

Title	Optical and near infrared observations of accretion processes in galactic compact objects
Authors	McConnell, Owen
Publication date	2017
Original Citation	McConnell, O. 2017. Optical and near infrared observations of accretion processes in galactic compact objects. PhD Thesis, University College Cork.
Type of publication	Doctoral thesis
Rights	© 2017, Owen McConnell. - http://creativecommons.org/licenses/by-nc-nd/3.0/
Download date	2023-05-04 22:28:12
Item downloaded from	http://hdl.handle.net/10468/4828

NATIONAL UNIVERSITY OF IRELAND, CORK



UCC

Coláiste na hOllscoile Corcaigh, Éire
University College Cork, Ireland

Optical and Near Infrared Observations of Accretion Processes in Galactic Compact Objects

by

Owen McConnell MSci

Thesis submitted in partial fulfillment of the
requirements of the degree of Doctor of Philosophy

Head of Department: Prof. John McInerney

Supervisor: Prof. Paul Callanan

Declaration of Authorship

I declare that the thesis submitted is my own work, and has, where necessary, been duly referenced and has not been submitted for another degree, either at University College Cork or elsewhere.

Signature

Date

Abstract

In this thesis, we present optical and near-infrared observations of compact binary systems. The observations are used to refine the binary parameters of several Low Mass X-ray Binaries, and to better understand the accretion processes in these systems.

Accretion is essential in the formation of stars, planets and solar systems yet remains poorly understood. In this thesis, we present results that focus on the accretion processes in two important Low Mass X-ray Binary systems.

In Chapter 3, optical photometry and spectroscopy are used to study the pulsar system PSR J102341.6+003841. The system has been observed to be accreting material from its companion, while radio pulsations indicate this accretion process is transient in nature. Combining quiescent photometry and spectroscopy allows us to constrain the binary orbital parameters, while photometry obtained when the system was in outburst allows us to investigate the nature of accretion within the system.

In Chapter 4, simultaneous optical photometry and spectroscopy is used to present a proof of concept for the black hole system A0620-00. We used spectroscopy to determine the contribution of the light from the accretion disc at each phase of our observation. This contribution was then removed from the optical light curve, leaving the pure ellipsoidal modulation due to the motion of the secondary

star. Our results suggest that for systems such as A0620, we will require the next generation of telescopes to successfully complete such a study.

Finally, Chapter 5, focuses on the black hole system GRS1915+105, one of the most massive stellar mass black holes in the Galaxy. We present infrared spectroscopy in an attempt to constrain the mass of the black hole and determine any orbital period variation. The presence of double peaked emission lines in the spectra allow us to probe the nature of the very large accretion disc in this long period system.

Acknowledgements

There are many people without whom this work would not have been possible. Firstly to my supervisor, Prof. Paul Callanan, for all your help, guidance and encouragement over the past number years, thank you. I am extremely grateful for the opportunity you gave me, it has been much appreciated.

Thanks must go to the many collaborators who took data: Peter Garnavich, Mark Kennedy, Jeffrey McClintock, John Menzies, John Thorstensen and Mark Reynolds.

To all the people who came through the X-ray binaries research group over the years. Dan, thanks for helping me find my feet. To Hayret, Liam, Mark, Selma and Simon thanks for making coming into work every day so enjoyable. To the various summer students and fourth years I accompanied on observing trips, thanks for putting up with me.

Thanks must go to Science Foundation Ireland for their financial support, without which this project could not have happened.

To my family, Mum, Dad and Niall, thanks for your constant support and encouragement when things got tough and the end never seemed in sight.

Finally to Fiona, your help, support and patience over the last few years, especially at the end, have helped me more than I could ever say. I simply could not have done it without you.

Owen McConnell

July 10, 2017

List of Figures

1.1	Mass-radius diagram for a variety of EoSs. Also marked in green and blue are various forbidden regions. From Lattimer and Prakash (2015).	2
1.2	The Hertzsprung-Russell Diagram used to classify stars according to their luminosity, spectral type, temperature and evolutionary stage. Also shown are well known examples of stars at various stages of their evolution.	4
1.3	A schematic of a HMXB and LMXB where the cross indicates the centre of mass. The figure of eight-shaped line defines the Roche lobes of the two stars. In the case of the HMXB the arrows represent the strong stellar wind on the secondary star, also indicating that this is the method of accretion onto the compact object. The LMXB cartoon shows the accretion flow, through the L_1 point (see 1.3.1 for more detailed discussion on Roche lobes), forming a disc around the primary. Adapted from Tauris and van den Heuvel (2003).	8
1.4	Formation of a binary system and its evolution to become a LMXB. The end of this phase sees the emergence of a binary millisecond pulsar. Adapted from Tauris and van den Heuvel (2003).	11
1.5	19

1.6	This figure is produced by solving Equation 1.2 numerically for a mass ratio $q = 0.47$ and plotting the resulting equipotential surfaces in the orbital plane of the binary. The Lagrangian points are marked and the compact object is on the left. The centre of mass is marked with a cross and the axes are in units of solar radii. Adapted from Tauris and van den Heuvel (2003)	20
1.7	Trajectories of three test particles in the xy plane with small injection velocities through the L_1 point for a mass ratio of 0.6 (from Flannery, 1975).	22
2.1	Optical diagram of the 1.8 m VATT telescope.	30
2.2	Optical diagram of the 1 m SAAO telescope.	30
2.3	Optical diagram of a Ritchey-Chrétien telescope. M_1 and M_2 refer to the primary and secondary mirrors respectively, while F denotes the focal point.	31
2.4	Layout of the ISIS red grating cell.	33
2.5	Layout of the ISIS optical spectrograph.	33
2.6	MAGE optical design.	34
2.7	Layout of the MAGE optical spectrograph.	35
2.8	NIFS optical design.	36
2.9	Layout of the NIFS spectrograph.	37
2.10	The aperture and background selected to extract a spectrum.	39
2.11	A plot of the CuAr arc lines used to wavelength calibrate the J1023 spectra.	40
2.12	An example of a fully reduced and wavelength calibrated science spectrum of J1023.	41

2.13	An example MAGE spectrum of a flux standard star. The central wavelengths (blue) and order number (red) are listed. Figure from Bochanski et al. (2009a).	42
2.14	An example of the tilt observed in the arc lines.	44
2.15	An example of a fully reduced, extracted and continuum normalised spectrum of A0620.	45
2.16	An example of typical NIFS data. Clockwise from top left these images are: science data, arc lamp, Ronchi mask and flat lamp. Clearly seen in each image is the different slices.	47
2.17	The image on which a circular aperture (in blue) is placed around the star. Counts are summed within this aperture to produce a one dimensional spectrum of GRS1915.	49
2.18	A one dimensional, fully reduced and normalised spectrum of GRS1915.	50
3.1	The average of all 26 spectra is shown below and the G2V template used for cross-correlation is shown on top. The two most prominent absorption features, the Ca+Fe blend and H-alpha lines, are labeled. The data have been shifted to the rest frame of the secondary.	55
3.2	Radial velocity curve folded over the best fit period of 0.1980966(1) days. Error bars have been scaled to achieve a fit with a reduced $\chi^2 = 1$	56
3.3	Results of our Roche lobe underfilling modelling of J1023 using ELC and the V-band photometry of TA05. Data are repeated for clarity. .	59

3.4	The left panel shows the inclination of the system against the Roche lobe filling factor of the secondary star and the right panel shows the mass of the primary against the filling factor. The contours here represent constant values of reduced χ^2 and the dashed lines are the 1σ confidence limits. The χ^2 minimum occurs at 135.88 which corresponds to a reduced $\chi^2=1$	60
3.5	The residual H α emission seen as a result of the optimal subtraction.	62
3.6	The three sets of V-band photometry taken while the system was in its recent outburst phase. Figure 3.6a shows the SAAO data (black open squares) taken using the 1m telescope on the nights of 2014/06/06, 2014/06/12 and 2014/06/13 and Atel data (red filled circles) of Halpern et al. (2013) taken using the 1.3 m McGraw-Hill telescope at the MDM Observatory on Kitt Peak. Figure 3.6b shows the VATT data taken on the night of 2014/04/29. Data are repeated for clarity.	65
4.1	The effect of including non-stellar light on the inclination of A0620-00 found from modelling K-band spectra. Arrows indicate the 2σ upper limits on the disc contamination and inclination. Figure adapted from Shahbaz et al., 1999.	70
4.2	An i -band light curve of A0620-00 taken from Cantrell et al., 2010. .	74
4.3	Blue filled circles show the fractional contribution of the accretion disc to the total light of the system in the V-band. The red filled circles show the V-band magnitudes after the disc contribution has been removed. The errors on the veiling have been omitted for clarity.	77

5.1	Examples of NIFS spectra showing only absorption lines (bottom, showing some of the lines included in the cross correlation) and both absorption and emission lines (top).	85
5.2	The radial velocity curve of GRS1915 found from the 2013 H-band NIFS spectra. The error bars have been enlarged to achieve a reduced $\chi^2 = 1$. The 2010 points (in blue) are plotted to show the lack of radial velocity variation.	87
5.3	A typical VLT spectrum of GRS1915 before we applied the telluric and bad pixel corrections.	88
5.4	The radial velocity curve of GRS1915 found from the H-band VLT spectra listed in Table 5.2. The error bars have been enlarged to achieve a reduced $\chi^2 = 1$	89
5.5	Comparison between the residual spectrum of the two wavelength regions considered in the average GRS1915 spectrum (bottom spectrum in each panel) after the scaled template spectrum (top spectrum in each panel) was subtracted. Some of the strongest absorption lines have been labelled.	91
5.6	The straight line fit to the results shown in Table 5.4. The error bars are smaller than the size of the data points.	94
5.7	O - C residuals using our refined ephemeris.	95
5.8	Average VLT K-band spectrum of GRS1915.	98
5.9	K-band trail of the VLT spectra showing emission blue-ward of the absorption line in the first half of the orbit. In the second half the absorption line becomes stronger and the emission disappears. Data have been repeated for clarity.	99

5.10	Typical H-band trail of the VLT spectra showing the S-wave pattern of the absorption lines of the secondary star as well as the emission line centred on 16411.7 Å. Data have been repeated for clarity.	100
5.11	Emission line (16411.7 Å) EW versus the MAXI counts for the VLT spectra. It is clear there is no strong correlation.	101
5.12	The averaged H-band spectra of GRS1915 using the VLT spectra (top) and NIFS (bottom). The spectra have not been shifted to the rest frame of the donor in order to show the emission lines.	103

List of Tables

1.1	The current known accreting X-ray millisecond pulsars in LMXB systems. The companion types are: WD = White Dwarf (He and C/O refer to a Helium or Carbon/Oxygen core respectively), BD = Brown Dwarf, MS = Main Sequence, SubG = Sub Giant. Adapted from Patruno and Watts (2013).	14
3.1	The range of G-type stars used in the optimal subtraction process described in the main text. We note the minimum χ^2 occurs for a G2V star.	55
3.2	Results of the ELC modelling for the secondary star underfilling its Roche Lobe.	58
4.1	The results of the veiling measurements and the resulting corrected photometry at each phase of our observations. The error on the veiling is detailed in the main text, while the error on the photometry was taken to be the standard deviation of a non-varying comparison star in the same field of view as A0620-00.	76

5.1	List of observations of GRS1915 from 2010 and 2013. The total exposure time for each night, the orbital phase and whether the spectra are dominated by absorption lines only or both absorption lines and emission lines is shown.	82
5.2	List of VLT observations of GRS1915 from Steeghs et al. (2013). The date and orbital phase are listed and the total exposure time for each night was 2400s. All spectra show both emission and absorption lines.	83
5.3	Fractional contribution of the secondary star to the total light of the system for the two regions of interest.	92
5.4	Results of the fits to each radial velocity curve for the four epochs of observation. Also shown is the number of orbits that have occurred between the reference epoch of Steeghs et al. (2013) and the remaining three epochs.	93

Contents

Declaration	i
Abstract	ii
Acknowledgements	iv
List of Figures	v
List of Tables	xi
1 Introduction	1
1.1 Formation of Compact Objects	3
1.2 Binary Stars	5
1.2.1 X-ray Binaries	7
1.2.2 Low Mass X-ray Binaries	7
1.2.3 Formation and Evolution of LMXBs	9
1.2.4 Accreting Millisecond Pulsars	12
1.2.5 Mass Distribution and Evolution of Binary Systems	13
1.3 Accretion	17
1.3.1 Accretion in LMXB Systems	17
1.3.2 Accretion Discs	21
1.4 Measuring the Primary Mass in LMXBs	24

1.5	Organisation of the Thesis	26
2	Instrumentation and Data Reduction	28
2.1	Instrumentation	28
2.1.1	McGraw-Hill Telescope	28
2.1.2	Vatican Advanced Technology Telescope	29
2.1.3	South Africa Astronomical Observatory	29
2.1.4	Irénée du Pont Telescope	31
2.1.5	William Herschel Telescope	32
2.1.6	Magellen Telescope	34
2.1.7	Gemini Telescope	35
2.2	Data Reduction	37
2.2.1	Optical Photometry	38
2.2.2	Optical Spectroscopy	38
2.2.3	IR Spectroscopy	45
3	PSR J102347.6 + 003841	51
3.1	Introduction	52
3.2	Observations and Data Reduction	53
3.3	Results	54
3.4	An Eclipsing Light Curve Model	57
3.4.1	Residual H α Emission	61
3.5	A Change in State	62
3.5.1	Comparison to Similar Systems	63
3.6	Conclusions	64
3.7	Additional Discussion	66

4	A0620-00	69
4.1	Introduction	70
4.2	Observations and Data Reduction	72
4.3	Analysis	73
5	GRS 1915+105	79
5.1	Introduction	79
5.2	Observations and Data Reduction	81
5.3	Results	84
5.3.1	Veiling Measurement	90
5.3.2	Refining the Ephemeris	93
5.3.3	K-band Analysis	98
5.3.4	Emission Line Study	99
5.4	Similar Systems	105
6	Conclusions and Future Work	109
A	An Eclipsing Light Curve Code	115
B	The O-C Method	117
C	List of Publications	118
	Bibliography	120

Chapter 1

Introduction

Low mass X-ray binaries (LMXBs) are interacting binary systems in which a low mass (less than $\sim 1M_{\odot}$), typically main sequence, companion star orbits a compact object, either a neutron star or black hole. The companion star transfers mass to the primary star via an accretion disc, generally fed by Roche lobe overflow (see Section 1.3.1). The energy released in the inner disc gives rise to the observed X-rays.

The first LMXB, Scorpius X-1, was discovered over 50 years ago by Giaconni et al. (1962) and was the first extra-Solar object observed to emit X-rays. Since then almost 200 LMXB systems have been discovered (Liu et al., 2007) while in their catalogue, Ritter and Kolb (2003, updated 2016), present 1429 CVs, 108 LMXBs and 619 related objects with the caveat that all these have known orbital periods, thus the true numbers may be higher.

The study of LMXBs is important for several reasons. Firstly they provide a means of studying stellar mass black holes. Determining accurate black hole masses is crucial if we are to understand the evolutionary path that lead to the creation of the black hole. Secondly it allows us to study the process of accretion. Accretion is ubiquitous throughout the Universe, essential to the formation of stars, planets and

solar systems; however it is still poorly understood. Finally these systems allow us to study matter in extreme densities which we cannot produce on Earth. For example, there are many different neutron star equations of state (EoS) which seek to explain how matter should behave in these high density scenarios. However these themselves are poorly constrained. Figure 1.1 shows the numerous neutron star mass-radius relationships for different EoS. From this, for example, the measurement of a high mass neutron star would help to constrain the neutron star EoS.

In this Chapter we begin by discussing the formation of compact objects and the evolution of binary systems, before discussing the properties of LMXBs and accretion in more detail.

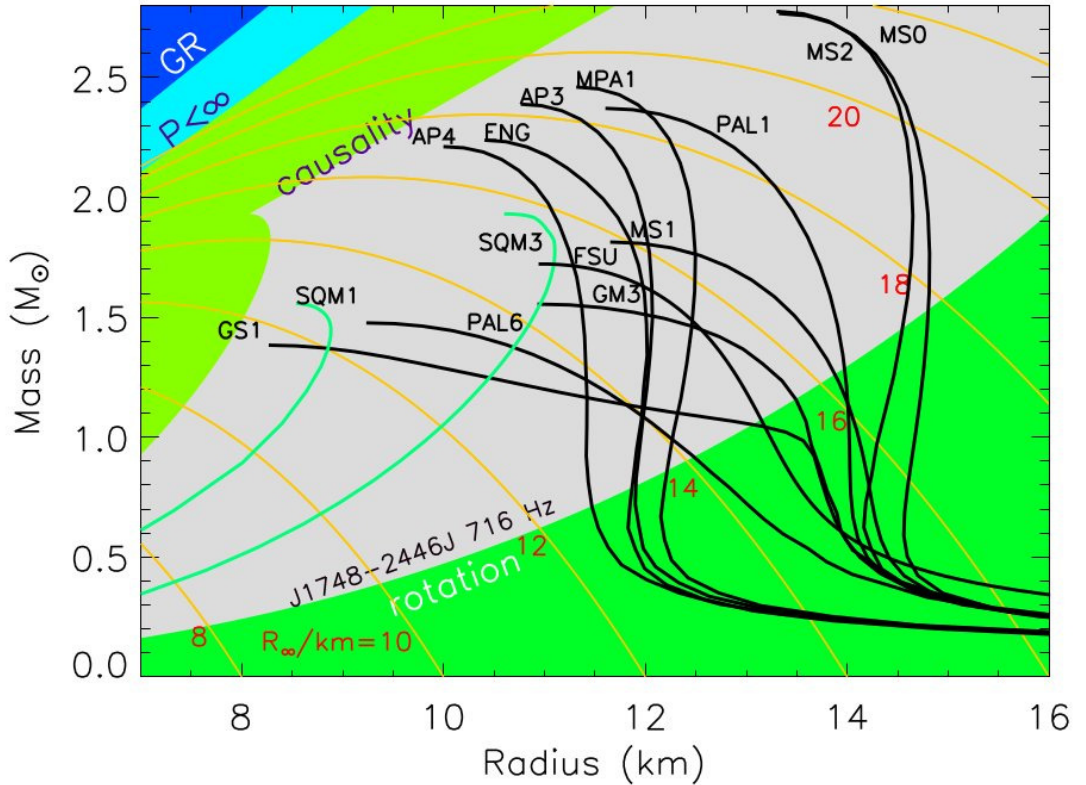


Figure 1.1: Mass-radius diagram for a variety of EoSs. Also marked in green and blue are various forbidden regions. From Lattimer and Prakash (2015).

1.1 Formation of Compact Objects

The following section summarises the current theory of the formation of white dwarfs, neutron stars and black holes. A number of sources were used and we refer the reader to those for a more detailed treatment. A comprehensive review of protoplanetary discs and their evolution can be found in Williams and Cieza (2011), stellar formation and evolution is explained in detail by Kippenhahn and Weigert (1994), Salaris and Cassisi (2005) and McKee and Ostriker (2007), while Lattimer and Prakash (2004) describes the formation of neutron stars and SOME GUY reviews the formation of black holes.

Stars are formed as the result of the gravitational collapse of a cold, dense molecular cloud. During the collapse the cloud fragments into smaller clumps which may then contract to form a protostar. As it condenses the protostar rotates faster and increases in temperature and is surrounded by material called a protoplanetary disc.

Over time the temperature of this protostar may rise above the threshold for nuclear fusion to occur. When this happens, Hydrogen is converted to Helium in the core and the star will do so for the majority of its lifetime. During this phase of its evolution it is known as a Main Sequence star.

Once all the Hydrogen in the core has been converted to Helium the core will begin to contract. This causes the temperature of the star to increase to the point that a thin shell of Hydrogen will burn around the Helium core. The continued contraction of the core causes the outer envelope of the star to expand. The star has now evolved onto the Giant branch of the Hertzsprung-Russell Diagram (see Figure 1.2).

Eventually the core becomes hot enough for Helium burning to occur while continuing to burn Hydrogen in a shell around the core. Once the Helium has been

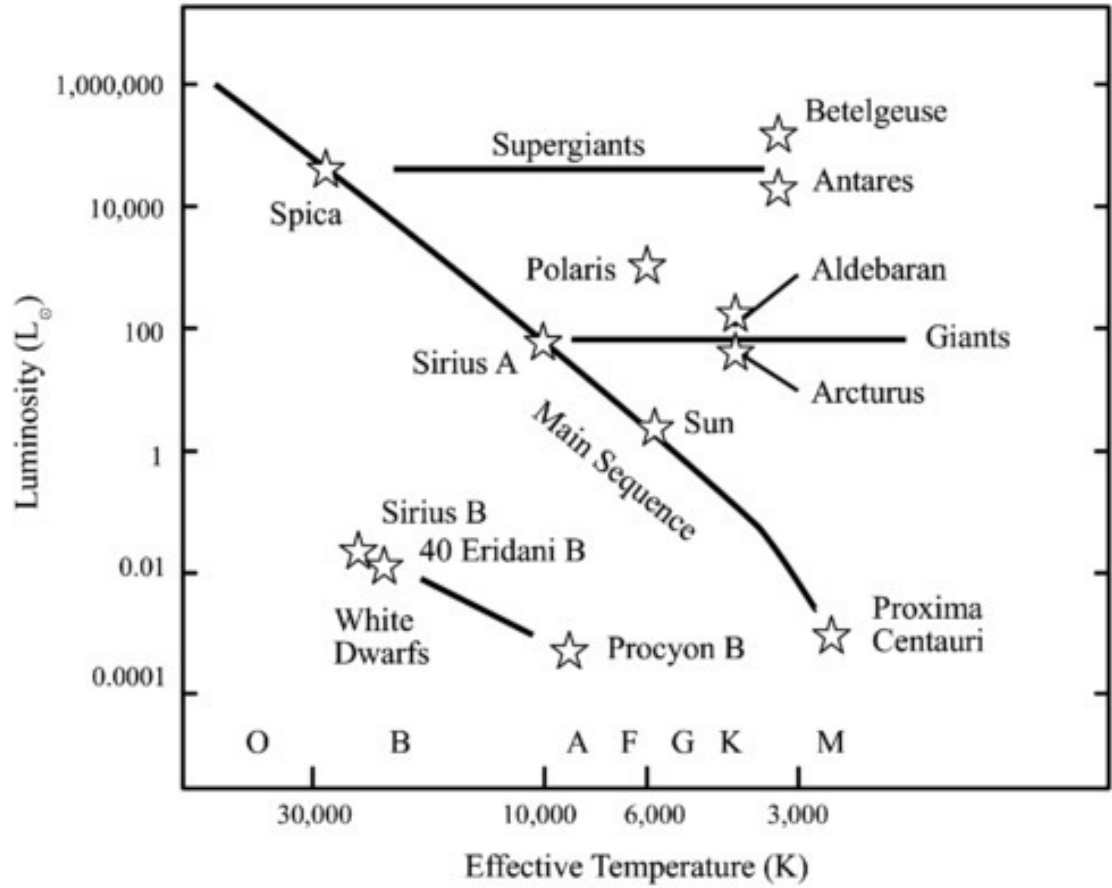


Figure 1.2: The Hertzsprung-Russell Diagram used to classify stars according to their luminosity, spectral type, temperature and evolutionary stage. Also shown are well known examples of stars at various stages of their evolution.

converted to Carbon the core contracts and increases in temperature once again. This ignites a Helium burning shell between the Carbon core and Hydrogen burning shell.

For stars with a mass less than $8M_{\odot}$ the Carbon core continues to contract but cannot reach the temperature required for Carbon fusion to begin. The two burning shells of Hydrogen and Helium are thermally unstable and eventually the outer envelope is expelled, forming a planetary nebula, leaving only the Carbon core. The core continues to contract until it is supported by electron degeneracy pressure (the Pauli exclusion principle forbids two Fermions from occupying the same quantum

state) which counteracts further gravitational collapse. The remaining core is known as a White Dwarf and as fusion can no longer occur the core slowly cools.

If the mass of the star is greater than $8M_{\odot}$ the core temperature will reach the level required for Carbon fusion to occur. The process of core burning, core contraction and shell burning is repeated until Iron is formed in the core surrounded by burning shells of Silicon, Oxygen, Neon, Carbon, Helium and Hydrogen. At this point it is no longer energetically favourable for this process to continue. As the star is no longer burning fuel the inward force of gravity overcomes the outward radiative pressure and the star begins to collapse.

If the mass of the core is less than $3M_{\odot}$ the gravitational collapse can be halted by neutron degeneracy pressure. The sudden halt of the collapse produces a shock wave which propagates through the outer layers of the star in what is known as a core collapse supernova leaving behind a Neutron Star. If the mass of the core is greater than $3M_{\odot}$ even neutron degeneracy pressure is unable to stop further gravitational collapse and a Black Hole is formed.

1.2 Binary Stars

The estimates of the number of stars in binary, or even multiple, systems varies, however there is a general consensus that this is a common occurrence, with some estimates that nearly half of sun-like stars reside in such systems (Tobin et al., 2016 and references therein).

The most common type of accreting binary systems are Cataclysmic Variables (CVs, e.g. see Ritter and Kolb, 2003, updated 2016) that consist of a white dwarf primary star and a late-type, main-sequence secondary star which fills its Roche lobe, transferring mass to the primary star via Roche lobe overflow. There are

many subclasses of CVs, defined by their outburst characteristics and invariably named after a prototype star (see Warner, 1995 for a review of CVs). Some of these include: Recurrent Novae which undergo repeating periodic outbursts; Dwarf Novae, or U Gem stars, which undergo similar outbursts but at a lower magnitude; and AM Her systems in which the rotational period of the white dwarf is synchronised with the binary orbital period and matter is channelled onto the poles of the white dwarf, rather than forming an accretion disc.

Binary stars can be classified in a myriad of ways but broadly can be thought of as either detached or interacting. The latter are systems where mass is transferred from one star to the other. Binary systems are can also be classified based on how they appear to the observer. For visual binaries the system is close enough to the observer so that the two stars can be resolved with the aid of a telescope (e.g. Alpha Centauri). One recent estimate puts the number of visual binary systems at ~ 130000 (Kovaleva et al., 2017) For spectroscopic binaries (systems that are too far away to resolve both components) if we can measure the Doppler shift of lines from only one star the system is known as a single-lined spectroscopic binary (single lined systems may include those where one star is much brighter than the other, a system containing a planet or where the unseen component is a black hole) or a double-lined spectroscopic binary (such as the HMXB WR 68a, Collado et al., 2015) if the Doppler shift can be measured for both stars. Finally, if the plane of the orbit of a binary system lies along our line of sight (an inclination close to 90°) the system is known as an eclipsing binary.

1.2.1 X-ray Binaries

Due to the transfer of mass from one star to the other, the evolution of stars in interacting binary systems is very different to that of their detached counterparts. Binary systems can contain stars of any type and the two stars themselves can be of the same or differing type. However, X-ray binaries consist of a neutron star or black hole primary and a secondary star which can be any type of star which loses mass to the primary. X-ray binaries are classified by the mass of the secondary star and have three broad categories: low mass X-ray binaries (LMXB) with a secondary of mass $\lesssim 1 M_{\odot}$, intermediate mass X-ray binaries (IMXB) with a secondary of between $\sim 1 M_{\odot}$ and $\sim 10 M_{\odot}$ (e.g. see Podsiadlowski et al., 2002) and high mass X-ray binaries (HMXB) with a secondary of mass $\gtrsim 10 M_{\odot}$ (e.g. Chaty, 2011). The method of accretion onto the compact object varies between the three types. Typically in LMXBs and IMXBs accretion is through Roche lobe overflow (see Section 1.3) via a disc which forms around the primary star, while in HMXBs mass loss is mainly due to a wind from the secondary.

X-ray binaries are important objects to study for several reasons. Most obviously they enable us to study the end states of stars, but they also allow us to see how matter behaves in extreme density scenarios, to test general relativity in strong gravity and to study the process of accretion; understanding the latter is important, not only for binary systems, but also more generally for the formation of stars, planets and even stellar systems.

1.2.2 Low Mass X-ray Binaries

The main focus of this thesis involves the study of LMXBs which, as already stated, accrete matter via Roche lobe overflow. These systems get their name as they are

brightest in the X-ray part of the spectrum (i.e. from 100 eV to 100 keV). This is because the infalling matter from the donor star is heated to millions of degrees, thus radiating in the X-rays. Typically they have X-ray luminosities of between 10^{35} erg s $^{-1}$ and 10^{38} erg s $^{-1}$ (Grimm et al., 2002), where the upper bound is determined by the Eddington limit - the point above which the radiative pressure overcomes the inward force of gravity and halts accretion.

LMXBs can be classified as either persistent or transient systems, depending on whether they are always X-ray bright or only periodically X-ray bright respectively. A general review of the properties of X-ray binaries can be found in e.g. Lewin (1997), while transient systems are the focus of White et al. (1984), Cowley (1992) and Tanaka and Shibazaki (1996), which we refer the reader to for more detail.

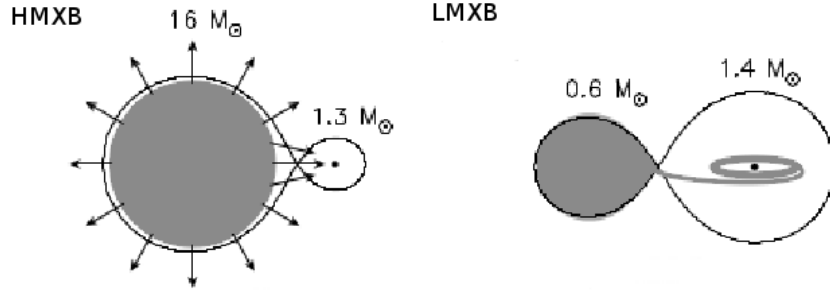


Figure 1.3: A schematic of a HMXB and LMXB where the cross indicates the centre of mass. The figure of eight-shaped line defines the Roche lobes of the two stars. In the case of the HMXB the arrows represent the strong stellar wind on the secondary star, also indicating that this is the method of accretion onto the compact object. The LMXB cartoon shows the accretion flow, through the L_1 point (see 1.3.1 for more detailed discussion on Roche lobes), forming a disc around the primary. Adapted from Tauris and van den Heuvel (2003).

Transient systems are characterised by the episodic X-ray outbursts they undergo. During these outbursts, transient systems show a soft X-ray spectrum that is characteristic of the persistently luminous systems. The X-ray outburst is accompanied by optical outbursts. These are thought to be caused by reprocessing of the X-rays in the accretion disc, which indicates that the secondary star has a low intrinsic luminosity, and therefore a low mass. As the X-ray and optical properties of transient systems in outburst closely match those of the persistent systems, it is believed the two harbour the same class of object. i.e. a close binary system containing a Roche lobe filling, low mass secondary star, and a neutron star or black hole primary.

As all LMXBs are variable, distinguishing between transient systems in outburst and persistent systems which happen to be undergoing a large increase in luminosity can be difficult. Historically, transient systems were only detected after they had gone into outburst. This was due to the pre-outburst luminosity being below the detection limit of the telescopes. As such, transient systems tend to be defined by an increase in X-ray luminosity from $< 10^{33} \text{ erg s}^{-1}$ to $> 10^{37} \text{ erg s}^{-1}$.

Outbursts are caused by a sudden increase in mass accretion onto the primary star (accretion will be discussed in more detail in Section 1.3). The secondary star also increases in luminosity, while radio outbursts are also often observed. Some systems even display relativistic jets (i.e. see Chapter 5), implying that, as a result of the sudden increase in mass accretion, some material is ejected from the system.

1.2.3 Formation and Evolution of LMXBs

Initially the binary system forms with a large separation between the two stars, as well as a large mass ratio. The more massive primary is believed to have an

initial mass of $\gtrsim 8 M_{\odot}$ while the secondary has mass $\lesssim 1 M_{\odot}$. The more massive primary star evolves at a faster rate than the secondary, eventually filling its Roche lobe. The resulting expansion of the primary engulfs the secondary star, forcing it to orbit through the envelope of the primary in what is known as the common envelope stage. The resulting frictional drag as the secondary orbits within the envelope of the primary causes the binary separation to decrease. The primary continues along its evolutionary track until a supernova occurs, forming a neutron star or black hole, blowing the envelope away. Tidal interactions between the two stars quickly circularise the orbit while also synchronising the rotational period of the secondary to the binary orbital period. The binary separation can decrease further if the two stars are close enough. There are two ways for this to occur: magnetic braking and the loss of gravitational radiation from the system. Magnetic braking is critical in removing angular momentum from systems with an orbital period approximately less than two days. Above this the binary separation is so large that magnetic braking is unable to drain the system of angular momentum and mass transfer will only begin once the secondary star has evolved off the main sequence. The magnetic braking concept states that highly ionized particles ejected from a star due to a wind are captured by the magnetic field lines of the star. They travel vast distances along these lines with the same angular velocity as the star until they eventually escape. This robs the star of some of its angular momentum, or spin, and in order for the total angular momentum of the system to be conserved the binary orbit has to shrink. Gravitational radiation is only effective in removing angular momentum from systems with the shortest orbital periods, on the order of one hour or less.

The resulting decrease in orbital separation from either of these processes allows

the secondary star to fill its Roche lobe. At this point mass can flow through the inner Lagrangian point and form an accretion disc around the compact object. For a detailed discussion on the formation and evolution of LMXBs, see Tauris and van den Heuvel (2003).

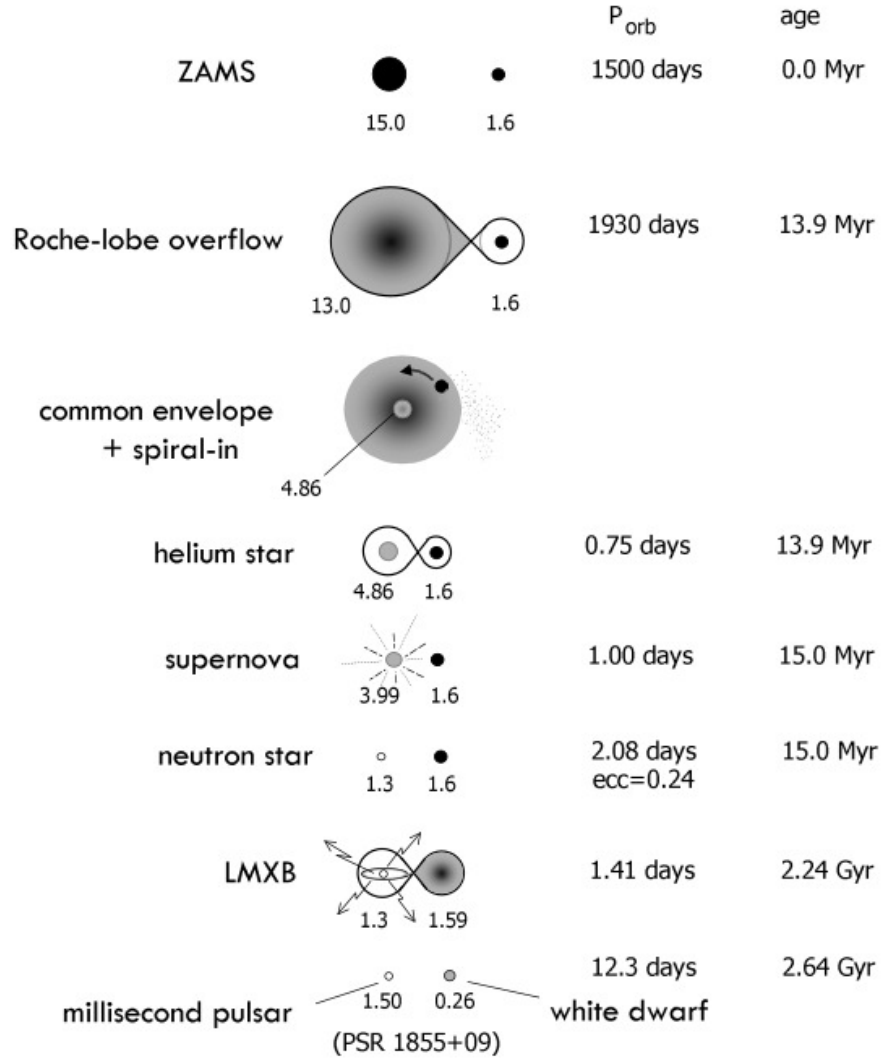


Figure 1.4: Formation of a binary system and its evolution to become a LMXB. The end of this phase sees the emergence of a binary millisecond pulsar. Adapted from Tauris and van den Heuvel (2003).

1.2.4 Accreting Millisecond Pulsars

The end of the LMXB phase occurs when the entire outer layers of the secondary star have been stripped off leaving only the core and the compact neutron star primary with a millisecond rotational period. One key question is how these systems evolve to become isolated millisecond pulsars. Radhakrishnan and Srinivasan (1984) proposed the theory that the transfer of angular momentum during the accretion phase is responsible for spinning up the neutron star to millisecond rotational periods in a process dubbed *recycling*. The name comes from the fact that pulsars lose energy as they rotate and eventually they will either stop emitting radio pulsations or these pulsations will become too weak to be detected. If this happens during the LMXB phase the companion star fills its Roche lobe and mass transfer will ensue. Once accretion stops, pulsed radio emissions may start up again from the now recycled millisecond pulsar.

The first recycled millisecond pulsar was discovered over 30 years ago (Backer et al., 1982), however it took almost another 20 years before telescopes (in this case the Rossi X-ray Timing Explorer, RXTE) with the required sensitivity to confirm the recycling scenario. SAX J1808.4-3638 was the first accretion powered millisecond X-ray pulsar to be detected (Wijnands and van der Klis, 1998). Further evidence to support not only the recycling scenario but the belief that accreting X-ray millisecond pulsars are born out of LMXB systems came with observations of PSR J1023+0038. Originally observed as part of the Faint Images of the Radio Sky at Twenty Centimetres (FIRST) survey (Becker et al., 1994), it took another 4 years for Bond et al. (2002) to come across the system. What they found was a binary system in emission, with clear signs of an accretion disc. Subsequent observations failed to see any evidence of a disc, however, until Archibald et al. (2009) detected radio

pulsations from the system. It was the first neutron star found to have switched on as a radio pulsar after previously being a LMXB. Figure 1.4 shows the various stages of the formation of a LMXB and its evolution to a millisecond pulsar while Table 1.1 gives a list of the current known accreting X-ray millisecond pulsars.

1.2.5 Mass Distribution and Evolution of Binary Systems

The mass distribution of stellar mass black holes (SMBHs) is linked to the population and evolution of massive stars. As such it can provide clues to the end stages of massive stars, while it is also important in the calculation of the rates of gravitational wave emission from neutron-neutron star and black hole-neutron star mergers. The mass function provides the most reliable method of mass determination, however it remains difficult to tightly constrain the inclination (and ultimately, mass) of these systems. It follows that the mass distribution of SMBHs can be predicted by models of the evolution and resulting supernova of massive stars. Theoretical models like that of Fryer and Kalogera (2001) derive the mass of the supernova remnant as a function of the initial mass of the progenitor based on the necessary and available energy required to unbind the stellar envelope. The available energy is scaled to the supernova explosion energy, which in turn is calculated from core-collapse simulations. They then convolve the resulting remnant-progenitor mass relation with the initial mass function of the progenitor to find the theoretical mass distribution of SMBHs. Their results suggest a continuous remnant mass distribution covering a wide range from neutron star masses up to SMBH masses of $M_{BH} < 15 M_{\odot}$ (see Fryer and Kalogera, 2001, for a complete description).

Bailyn et al. (1998) carried out a Bayesian analysis of the mass distribution of the (at the time) seven known SMBH systems. They found a gap in the $3 M_{\odot}$ -

Source	Spin frequency(Hz)	Orbital Period(hrs)	Companion Type
SAX J1808.4-3658	401	2.01	BD
XTE J1751-305	435	0.71	He WD
XTE J0929-314	185	0.73	C/O WD
XTE J807-294	190	0.67	C/O WD
XTE J1814-338	314	4.27	MS
IGR J00291+5934	599	2.46	MS
HETE J1900.1-2455	377	1.39	BD
Swift J1756.9-2508	182	0.39	He WD
Aql X-1	550	18.95	MS
SAX J1748.9-2021	442	8.77	MS/SubG?
NGC6440 X-2	206	0.95	He WD
IGR J17511-3057	245	3.47	MS
Swift J1749.4-2807	518	8.82	MS
IGR J17498-2921	401	3.84	MS
IGR J18245-2452	254	11.03	MS

Table 1.1: The current known accreting X-ray millisecond pulsars in LMXB systems.

The companion types are: WD = White Dwarf (He and C/O refer to a Helium or Carbon/Oxygen core respectively), BD = Brown Dwarf, MS = Main Sequence, SubG = Sub Giant. Adapted from Patruno and Watts (2013).

$5 M_{\odot}$ range while the distribution peaked at $\sim 7 M_{\odot}$, seemingly at odds with the theoretical continuous distribution. Later studies (e.g. Özel et al., 2010, and Farr et al., 2011) were able to include a larger number of systems yet found the same $3 M_{\odot} - 5 M_{\odot}$ mass gap and cluster around $\sim 7 M_{\odot}$. One possible explanation for the dearth of systems in the mass gap is that they would be expected to have a mass ratio $q \sim 1$, which implies a higher rate of accretion and as such these objects may be persistent X-ray sources and so estimates of binary parameters are more difficult. This is due to the fact that these systems are bright and therefore identification of the secondary star may not be possible.

Effects which influence the mass distribution include the nature of the supernova itself as well as the binary evolution of the system. In the first case the relationship between the mass of the remnant and the amount of fallback (material that does not receive enough energy to escape the potential well of the newly formed black hole) is crucial. Theories of binary evolution imply a period of mass transfer pre-supernova and the ejection of the outer envelope of the progenitor which may change the nature of the supernova itself (Brown et al., 1996). One possible post-supernova process can also affect the mass distribution: accretion. If accretion can change the mass of the black hole significantly, a broad distribution would be expected. At the time, Bailyn et al. (1998) excluded V404 Cyg from their analysis but note, however, that as it had the most evolved secondary (K0IV) of any of the seven other systems, a period of accretion onto the black hole may have occurred.

The study, mentioned previously, by Podsiadlowski et al. (2003) did consider mass transfer after the creation of the black hole. They note the difficulties in modelling such systems as the initial mass of the black hole depends on both single and binary stellar evolution. The maximum initial mass of the black hole in a binary

system is dependent upon several factors: the minimum initial mass above which a star can collapse to form a black hole; the minimum mass above which a single star loses its Hydrogen envelope becoming a Helium burning star; the maximum radius a star can have before and after the formation of a He-burning core; the amount of mass lost during the He-burning phase, and; the amount of mass lost when the black hole forms. In particular the evolutionary track of massive stars, along with the maximum radius a star can achieve, remain poorly understood. However, we expect the most massive black holes to form from stars closest to the minimum mass above which the Hydrogen envelope is lost and the star becomes a He-burning star, and where the common envelope phase occurs near the end of the evolution of the progenitor. This means the progenitor spends as short a time as a He-burning star as possible, when mass loss via a wind can be substantial. Mass loss at this stage lowers the maximum possible mass of the resulting black hole. Podsiadlowski et al. (2003) modelled binaries containing a black hole of initial mass $M_{BH,int} = 10 M_{\odot}$ and a range of initial masses of the secondary star of $2 M_{\odot} < M_{S,int} < 17 M_{\odot}$ up to the point the evolution of the secondary lead to it becoming degenerate or detached. They found that mass transfer rates are higher for larger secondary masses at any point during the evolution, while low mass secondary stars remained close to thermal equilibrium and so mass transfer is determined by the nuclear evolution of these stars. In all cases the rate of mass accretion was assumed to be Eddington-limited and where the secondary was initially modelled as an unevolved star its end state was a white dwarf. Their most significant finding was that, again assuming an initially unevolved secondary star, the black hole can accrete a significant amount of material, possibly up to $\sim 7 M_{\odot}$. For a moderately evolved secondary this figure is still appreciably high at $\sim 4 M_{\odot}$. They also consider the affect accretion has on the

angular momentum of the black hole and, even for an initially non-rotating black hole, accretion can lead to a spin parameter of $a \sim 0.9$. Finally the potential X-ray luminosity of the most massive black hole systems is estimated to be $L_x \sim 10^{41} \text{ erg s}^{-1}$.

1.3 Accretion

It was through the study of X-ray binaries that accretion was widely recognised as the driving factor behind the observed high energy X-rays. Further study has shown the importance of angular momentum in the accretion process. Material being transferred cannot accrete directly onto the primary until it has lost a substantial amount of the angular momentum it possesses. This led to the idea of *accretion discs* as a means of removing angular momentum in X-ray binary (and other) systems (e.g. see Shakura and Sunyaev, 1973 and Balbus and Hawley, 1991).

1.3.1 Accretion in LMXB Systems

There are two main methods of mass transfer in interacting binary systems: stellar wind and Roche lobe overflow. In LMXB systems it is the latter which drives mass transfer and so we discuss it in more detail here. Roche lobe overflow occurs when a star fills its Roche lobe (the area around a star within which material is gravitationally bound to that star) and material moves through the L_1 point, forming an accretion disc around the more massive companion star. It was first described by Édouard Roche in the 19th Century who investigated the interaction of planets and their moons. With respect to binary systems the model makes several key assumptions:

1. synchronous rotation of the secondary star with the binary orbital period;

2. the stars have circular, Keplerian orbits;
3. the two stars are considered as point masses; and
4. the frame of reference is co-rotating with the binary centred on the centre of mass of the system.

The flow of material from one Roche lobe to another is described by a modified version of the Euler equation, the extra terms accounting for the centrifugal and Coriolis forces introduced by the rotating frame of reference (e.g. see Frank et al., 1985):

$$\frac{\delta v}{\delta t} + (v \times \Delta)v = -\Delta\Phi - 2\omega \times v - \frac{1}{\rho}\Delta P \quad (1.1)$$

where v is the velocity vector, t is time, ω is the angular velocity of the binary, $(2\omega \times v)$ is the Coriolis force, ρ is the density and P is the pressure. $-\Delta\Phi$ is the Roche potential and includes both the gravitational and centrifugal potentials. It can be expressed via the following equation:

$$\Phi(r_3) = -G \left(\frac{M_1}{r_1} - \frac{M_2}{r_2} \right) - \frac{1}{2}(\omega \times r_3)^2 \quad (1.2)$$

where G is the gravitational constant, ω is the angular velocity of the binary, M_1 and M_2 are the masses of the primary and secondary stars respectively, r_1 and r_2 are the distances to the primary and secondary stars, respectively, from the location where $\Phi(r_3)$ is to be calculated and r_3 is the distance from this same point to the centre of mass of the system. This is shown pictorially in Figure 1.5.

Taking the derivative of Equation 1.2 allows the gravitational equipotential surfaces, along which the gravitational force is balanced by the centrifugal force, to be found. This is shown in Figure 1.6, along with the five Lagrangian points. Of these, L_4 and L_5 are local maxima and L_1 , L_2 and L_3 are saddle points of the potential. L_1 , or the inner Lagrangian point, is the most significant. The equipotential surface

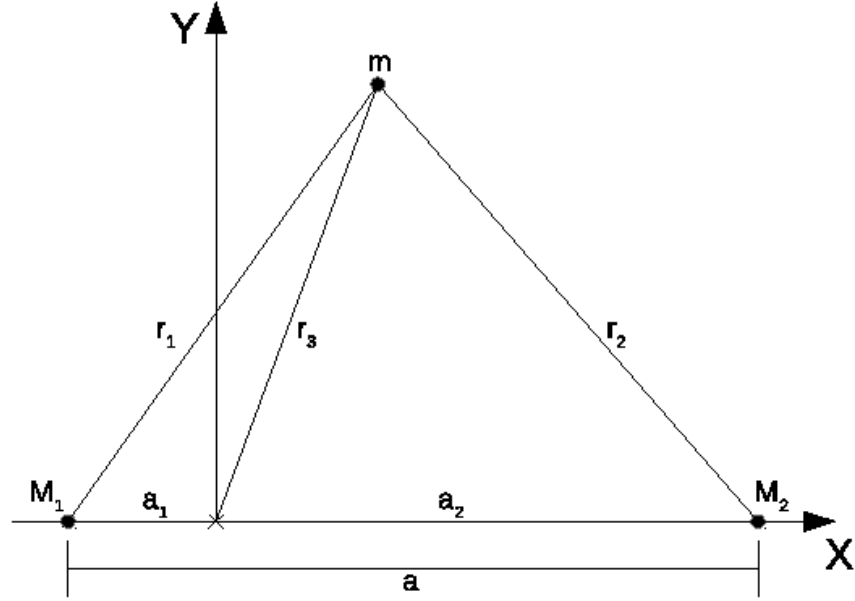


Figure 1.5

through the L_1 point forms two tear-drop lobes called Roche lobes. If a star fills its Roche lobe it is more energetically favourable for material in the vicinity of the L_1 point to flow into the Roche lobe of the other star than to leave the potential surface altogether.

In the context of mass transfer this implies the following: (a) if both stars do not fill their Roche lobes then the only method of accretion would be due to a stellar wind (i.e. in HMXB systems); (b) one star fills its Roche lobe and material flows through the L_1 point and will eventually accrete onto the other star; and (c) both stars fill their Roche lobes simultaneously, forming a contact binary.

The effective radius of the Roche lobe is defined as a sphere of the same volume

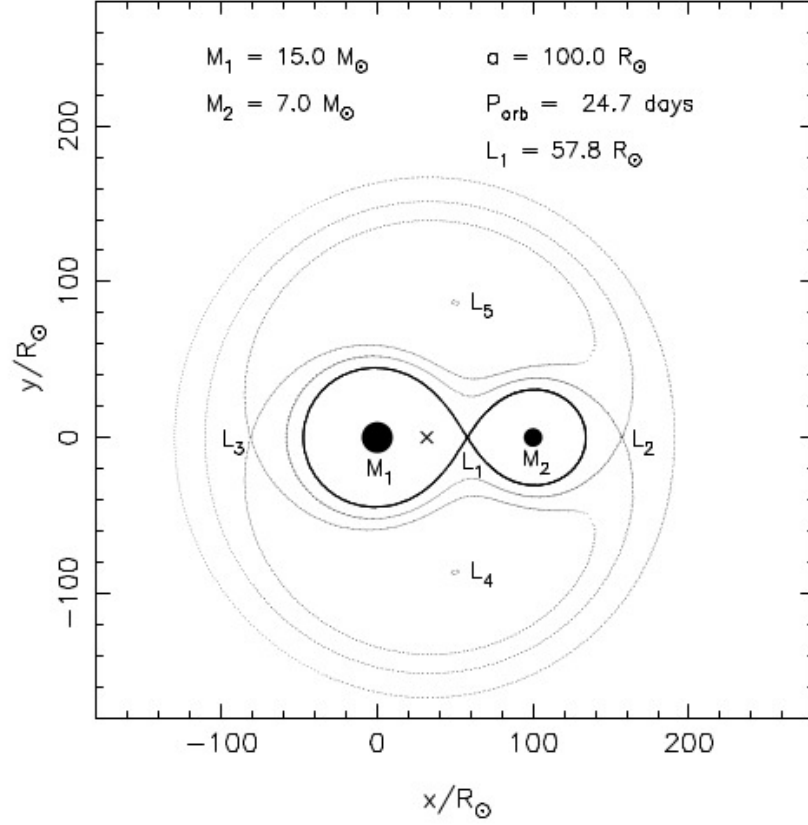


Figure 1.6: This figure is produced by solving Equation 1.2 numerically for a mass ratio $q = 0.47$ and plotting the resulting equipotential surfaces in the orbital plane of the binary. The Lagrangian points are marked and the compact object is on the left. The centre of mass is marked with a cross and the axes are in units of solar radii. Adapted from Tauris and van den Heuvel (2003)

as the lobe and is given by the Eggleton formula (Eggleton, 1983):

$$\frac{R_L}{a} \approx \frac{0.49q^{2/3}}{0.6q^{2/3} + \ln(1 + q^{1/3})} \quad (1.3)$$

Where q is the mass ratio and a is the binary separation. A consequence of mass transfer is that the mass ratio of the binary system changes. The redistribution of angular momentum also changes the orbital period which in turn changes the binary

separation. If the more massive star fills its Roche lobe (see Section 1.2.3) the mass transfer continues until the star shrinks due to dynamically unstable processes. If the less massive star fills its Roche lobe it requires angular momentum loss from the system, causing the orbital separation to decrease, to keep the star filling its Roche lobe to sustain mass transfer.

1.3.2 Accretion Discs

Gas flowing through the L_1 point does so as if it were escaping freely and so the flow velocity is equal to the sound speed in the atmosphere of the donor star (see Warner, 1995 or Lubow and Shu, 1975 for a detailed mathematical analysis). The gas is quickly accelerated to supersonic speeds, meaning the gas pressure can be neglected. The computation of the gas flow can therefore be reduced to calculating the path of a test particle dropped from the L_1 point with an initial speed equal to the sound speed.

Material flowing through the L_1 point will possess high angular momentum which implies that it cannot accrete directly onto the surface of the primary star but will eventually collide with the accretion stream as seen in Figure 1.7. As the gas stream is supersonic the collision will increase the temperature of the gas which will then radiate this heat away from the disc. To counteract this loss of energy the material in the inner disc moves closer to the compact object, losing angular momentum as it does so. Dissipative processes (shocks, collisions etc) in the disc exert a torque on the infalling material which transports angular momentum to the outer disc. This process is still relatively poorly understood, however, viscosity is believed to play a key role. As it is assumed the material in the disc moves in approximately Keplerian orbits this introduces a differential rotation: gas orbits at a different velocity with

respect to material beside it. The shear force exerted by the inner orbiting material transfers angular momentum to the outer orbiting material and so is transported to the edge of the accretion disc. So while material in the inner disc loses angular momentum and orbits closer to the primary, material in the outer disc gains angular momentum and orbits further from the primary. The disc stretches to both smaller and larger radii relative to the primary star. What happens at the disc edge to remove the angular momentum is unclear, however, tidal forces acting on the disc may feed it back into the orbit (Truss and Wynn, 2004).

Due to the large gravitational potential of compact objects, accretion onto them

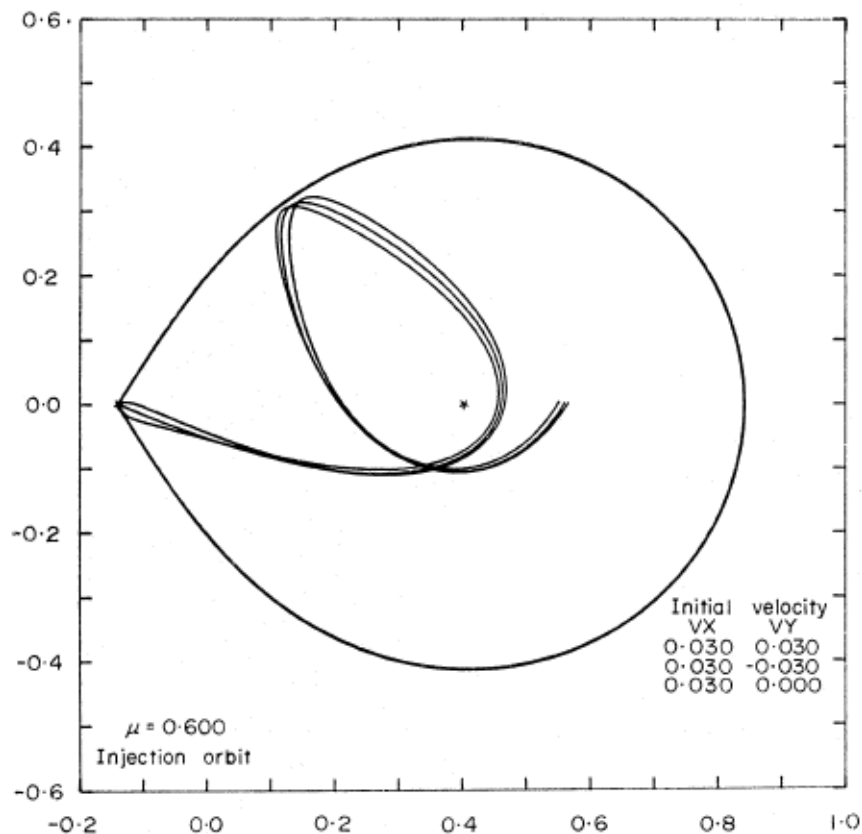


Figure 1.7: Trajectories of three test particles in the xy plane with small injection velocities through the L_1 point for a mass ratio of 0.6 (from Flannery, 1975).

can release vast amounts of energy. Indeed the accretion process is one of the most efficient ways of releasing energy, with up to 50% of the rest mass energy of the accreting material being released. The gravitational energy released during accretion is given by the following formula:

$$\Delta E = \frac{GMm}{R} \quad (1.4)$$

where M is the mass of the compact object with radius R and m is the mass of the material being accreted.

The energy liberated goes to heat which increases the temperature of the accretion disc as a whole and thus the disc luminosity is given by:

$$L_{disc} = \frac{GM\dot{M}}{2R} \quad (1.5)$$

where \dot{M} is the accretion rate. We can see that this is half the amount of energy released during accretion from Equation 1.4. See Frank et al., 1985 for a review. The temperature profile across an optically thick, geometrically thin accretion disc is (Carroll and Ostlie, 2007):

$$T(r) = \left(\frac{3GM\dot{M}}{8\pi r^3 \sigma} \left(1 - \left(\frac{R}{r} \right)^{1/2} \right) \right)^{1/4} \quad (1.6)$$

where M is the mass of the primary, \dot{M} is the accretion rate onto the primary, r is the radius of the accretion disc, σ is the Stefan-Boltzman constant and R is the radius of the primary.

Observational Evidence of Accretion Discs

As accretion discs in LMXBs cannot be resolved we rely on spectroscopy and photometry to infer their presence. For example, double peaked emission lines in spectra have long been used to imply the existence of accretion discs. As material in the disc orbits the central object, it is both blue shifted and red shifted, giving rise to

the double peaked nature of the emission line (see Figures 5.1 and 5.12 for examples of double peaked emission lines). Accretion discs are also hotter than the secondary star and hence have a blue spectrum.

Asymmetry in emission lines can be evidence of a warped accretion disc (see Section 5.3.4). Such a warped disc could also be explained by variable eclipse depths in photometric observations of LMXBs. Photometry can also provide an excellent means of observing time-variable events such as flaring. Interaction of material within the disc can lead to sudden outbursts which manifest as a spike in the light curve (e.g. see Figure 3.6).

1.4 Measuring the Primary Mass in LMXBs

Measuring the mass of the primary star in LMXBs is of great importance. Generally mass can be used to compare theoretical models (e.g. Salaris and Cassisi, 2005) of stellar evolution to what is observed. Accurate estimates of the masses of neutron stars can help to constrain the Equation of State which describes how matter behaves in extreme density and gravity scenarios. For black holes, the mass can be used to estimate its spin which is used to infer information on the formation and growth of the black hole (e.g. Podsiadlowski et al., 2003).

In order to constrain the mass of the primary, detailed observations of the secondary star is required. First, the mass function of the primary must be determined (e.g. see Pringle and Wade, 1985):

$$f(M_1) \equiv \frac{M_1 \sin^3 i}{(1+q)^2} = \frac{P_{orb} K_2^3}{2\pi G} . \quad (1.7)$$

where M_1 is the mass of the compact object, i is the inclination of the system, q is the mass ratio (M_2/M_1), P_{orb} is the orbital period of the binary, K_2 is the semi-

amplitude of the radial velocity curve of the secondary star and G is the gravitational constant. Rearranging for M_1 gives:

$$M_1 = \frac{(1 + q)^2}{\sin^3 i} \frac{P_{orb} K_2^3}{2\pi G} \quad (1.8)$$

The terms on the right hand side of this equation are all observable quantities. Therefore to estimate the mass of the primary we need knowledge of the mass ratio of the system, the inclination of the system, the orbital period of the secondary star and the semi-amplitude of the secondary star. As $(1 + q^2)$ is always greater than 1 and $\sin^3 i$ is always less than or equal to 1, this provides a lower limit of the mass of M_1 :

$$M_1 \geq \frac{P_{orb} K_2^3}{2\pi G} . \quad (1.9)$$

The semi-amplitude can be determined by measuring the radial velocity of the secondary. This involves cross-correlating (Tonry and Davis, 1979) the absorption lines in the spectrum of the secondary and measuring their Doppler shift relative to the absorption lines of a template star of the same spectral type and which has been shifted to zero heliocentric velocity. Plotting the velocities against time then yields the orbital period of the system (see Figures 3.2, 5.2 and 5.4 for examples of radial velocity curves).

The mass ratio can be estimated by measuring the rotational broadening of the absorption lines of the secondary star. The spectrum of a slowly rotating star will show deep and narrow absorption lines but as the rotational period of the star decreases these lines become broader and shallower due to the Doppler effect. Therefore comparing the spectrum of the secondary to that of a slowly rotating star of the same spectral type will give the rotational broadening of the secondary. Assuming the secondary is tidally locked and filling its Roche lobe (which is generally

true for LMXBs) the following relationship holds (Dunford et al., 2012):

$$\frac{v \sin i}{K_2} = 0.44 \left((1+q)^2 q \right)^{3/2} . \quad (1.10)$$

Therefore the mass ratio can be estimated from the two directly observable binary parameters: the rotational broadening of absorption lines and the semi-amplitude of the secondary star.

The final parameter needed from equation 1.8 to measure the mass of the primary is the inclination of the system. In practice this is the hardest property to accurately measure. If the binary inclination is close to 90° we see eclipses in the light curve and the inclination can be accurately constrained (and by extension the mass of the primary will also be more accurately determined). However eclipsing binaries are rare and so more usually we have to model the ellipsoidal variations due to the changing surface area of the secondary as it orbits the primary (see Appendix A and Orosz and H.Hauschildt (2000) for a detailed discussion of the code used). Infrared light curves are traditionally used for this as it is believed they suffer less from contamination due to light from the accretion disc. This is a particular problem for optical light curves. This is an important consideration as any extra light included in the modelling can lead to an underestimation of the inclination and thus an overestimation of the mass of the primary.

1.5 Organisation of the Thesis

The remainder of the thesis is organised as follows. In Chapter 2 we discuss the various data reduction methods employed on our data. In Chapter 3 we discuss optical observations, both photometric and spectroscopic, of PSR J1023+0038 in an attempt to better constrain the mass of the neutron star. This object has been

described as the missing link between LMXB systems and isolated millisecond rotational pulsars. In Chapter 4 we discuss simultaneous V-band spectroscopy and photometry of the black hole X-ray transient system A0620-00. The proof of concept presented in this Chapter attempts to measure the changing veiling at each phase of our observations. Chapter 5 outlines our attempts to use atomic lines in the H-band to better determine the binary parameters of the prototype galactic microquasar GRS1915+105. This is followed by some general conclusions and areas of future work.

Chapter 2

Instrumentation and Data Reduction

2.1 Instrumentation

The various data sets obtained for the work described in the thesis required the use of many different telescopes, and we briefly outline the design of these instruments below.

2.1.1 McGraw-Hill Telescope

The photometry of Thorstensen and Armstrong (2005), presented in Chapter 3, was obtained using the 1.3 m McGraw-Hill telescope¹, located at the Kitt Peak National Observatory in Tucson, Arizona.

A thinned SITe 1024×1024 pixel CCD was used, binned 2×2 and cropped to achieve a 256×256 pixel array with an image scale of 1.018 arcsec (per binned) pixel⁻¹.

¹For details see: <https://dept.astro.lsa.umich.edu/obs/mdm/technical/mcgraw.html>

2.1.2 Vatican Advanced Technology Telescope

The 1.8 meter Alice P. Lennon Telescope and the Thomas J. Bannan Astrophysics Facility, together known as the Vatican Advanced Technology Telescope (VATT²), was used to obtain photometry, presented in Chapter 3, on the night of April 29 2014. The optical design of the telescope can be seen in Figure 2.1. The focal length of the primary mirror is $f/1$, i.e. the focal length is equal to the diameter of the primary mirror. This allowed for a Gregorian design, which uses a concave secondary mirror at a point beyond the primary focus, allowing for sharp focusing across the entire field of view.

The data were taken using the back illuminated VATT4K CCD, a 4064×4064 pixel array, providing a field of view of 12.5 arcmin^2 and an image scale of $0.188 \text{ arcsec pixel}^{-1}$.

2.1.3 South Africa Astronomical Observatory

The 1 m telescope³ located near Sutherland, Northern Cape, was used to obtain photometry presented in Chapter 3 in June 2014. Built in 1964 it is of Cassegrain design with a focal length of $f/16$. The STE3 CCD was used which has a back illuminated 512×512 pixel array, providing a field of view of $158'' \times 158''$ and an image scale of $0.31 \text{ arcsec pixel}^{-1}$. The optical diagram of the telescope can be seen in Figure 2.2.

²For details see: <http://vaticanobservatory.org/VATT/>

³For details see: <http://www.sao.ac.za/science/facilities/telescopes/1-0m/>

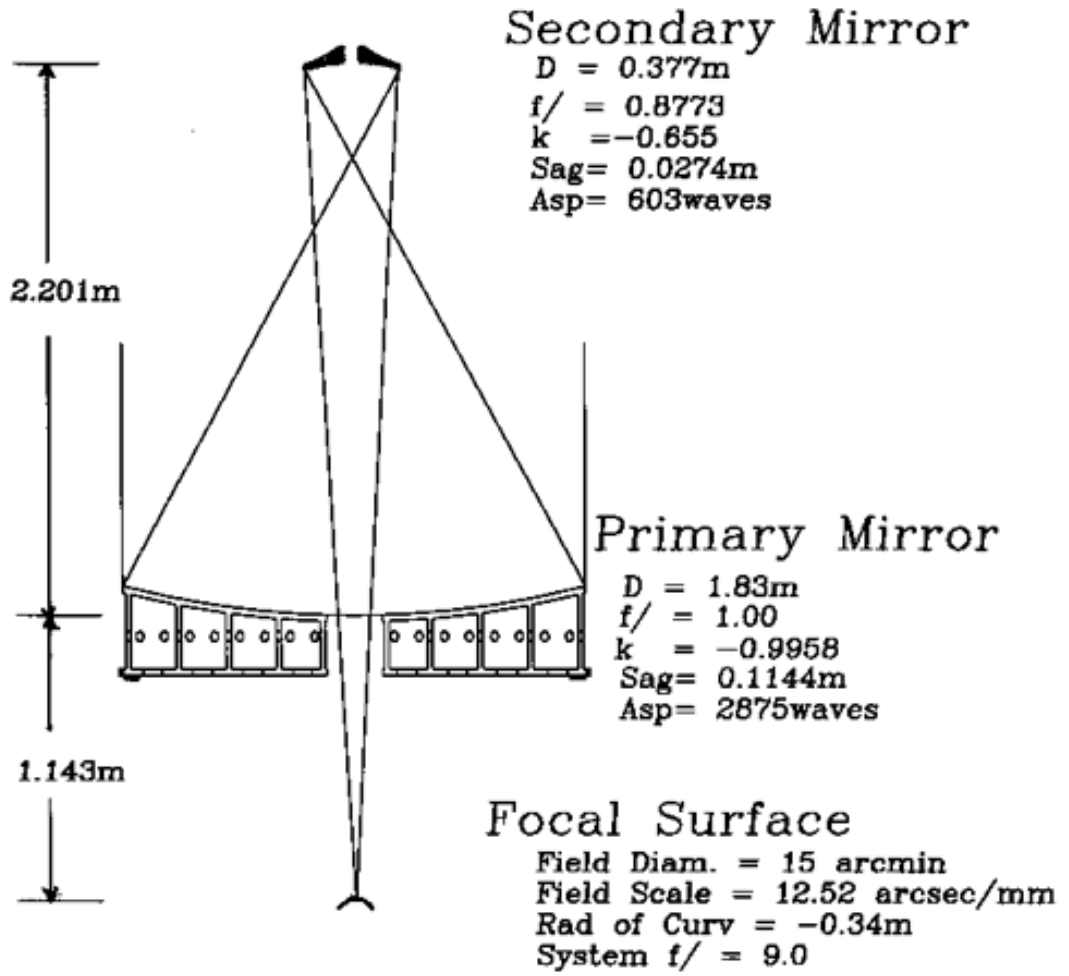


Figure 2.1: Optical diagram of the 1.8 m VATT telescope.

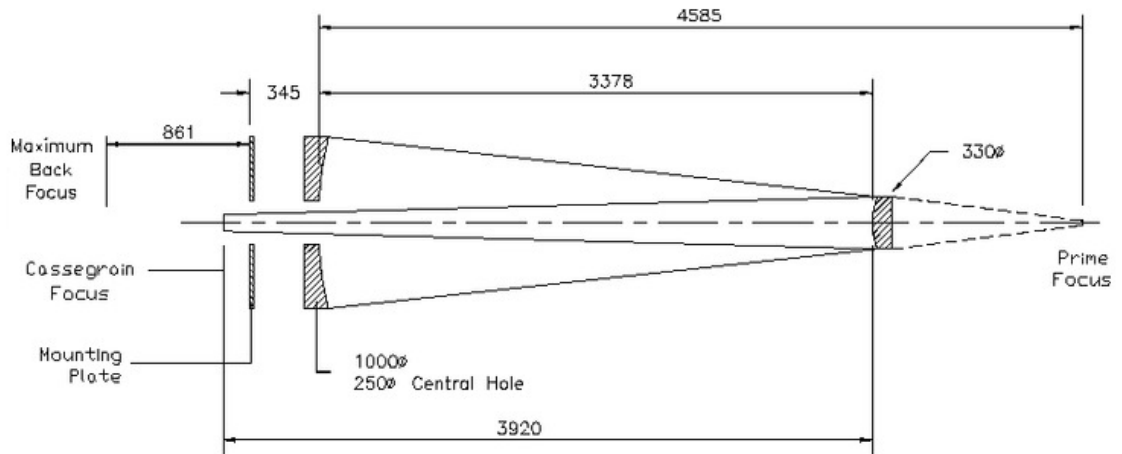


Figure 2.2: Optical diagram of the 1 m SAAO telescope.

2.1.4 Irénée du Pont Telescope

The 2.5 m Irénée du Pont telescope, used to obtain the photometry presented in Chapter 2.2.2, has been in operation at Las Campanas Observatory, Chile, since 1977.

The optical characteristics of the telescope are discussed in detail by Bowen and Vaughan (1973). To summarise, it is a Ritchey-Chrétien (RC) design with a Cassegrain focal length of $f/7.5$. This design yields images with radial sizes less than 0.3 arcsec to a field diameter of 2.1° . This limit to the field size is set by the chromatic aberration of the corrector plate and also by the maximum size of the hole in the primary that is permissible without vignetting the off-axis beam after it passes the secondary. The optical diagram of an RC telescope is shown in Figure 2.3.

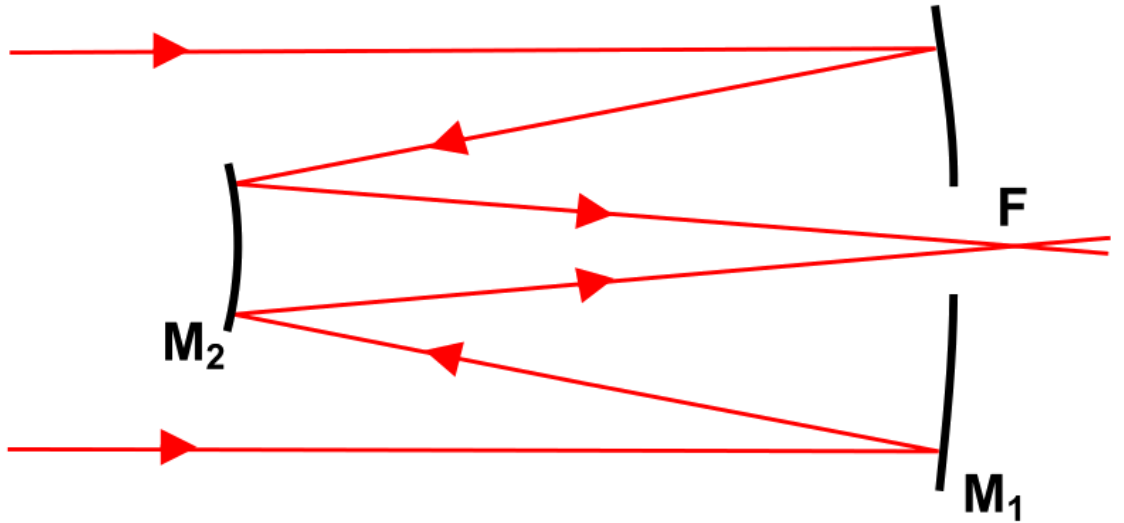


Figure 2.3: Optical diagram of a Ritchey-Chrétien telescope. M_1 and M_2 refer to the primary and secondary mirrors respectively, while F denotes the focal point.

2.1.5 William Herschel Telescope

The William Herschel Telescope (WHT, see Bingham, 1984) is a 4.2m telescope located on the island of La Palma in the Canary Islands. Inaugurated in 1987, it is of classical Cassegrain optical configuration with a focal length of $f/2.5$.

The Intermediate dispersion Spectrograph and Imaging System (ISIS, see Carter et al., 1993) instrument was employed to obtain the spectra described in Chapter ???. ISIS is a dual-arm spectrograph, with the blue arm and red arm optimised to cover specific wavelength ranges. The blue arm covers the wavelength range 3000\AA - 5000\AA and the red arm covers the wavelength range 5000\AA - 10000\AA . Light is fed into the two arms of ISIS by 45° fold mirrors on the optical axis of the telescope. The blue-fold mirror can be replaced by a choice of dichroic filters which reflect blue light and transmit red light, allowing simultaneous use of the blue and red arms. This is the most frequently used observing mode of ISIS.

There are nine gratings provided for use on ISIS, five for the blue arm and four for the red arm, each with a ruled area of $154\text{ mm} \times 206\text{ mm}$. The spectra presented in Chapter 3 were obtained using the R1200R grating. The first letter denotes the method of manufacture (in this case ruled), the number denotes the number of lines per millimetre while the last letter of the name indicates which arm of ISIS it is intended for (the red arm in this case). The red grating assembly can be seen in Figure 2.4 while the overall layout of ISIS is shown in Figure 2.5.

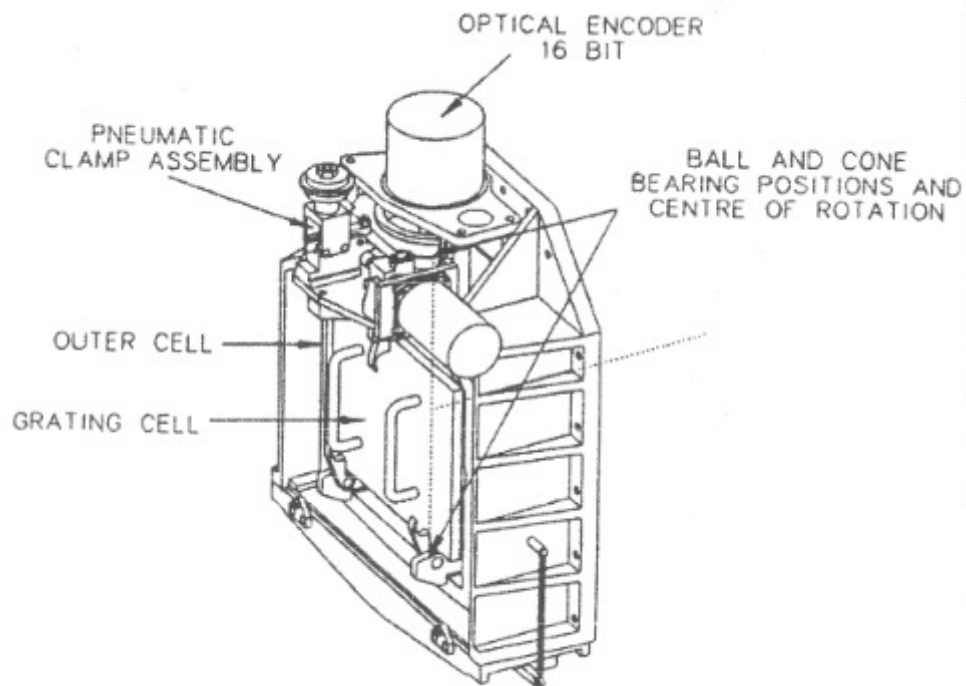


Figure 2.4: Layout of the ISIS red grating cell.

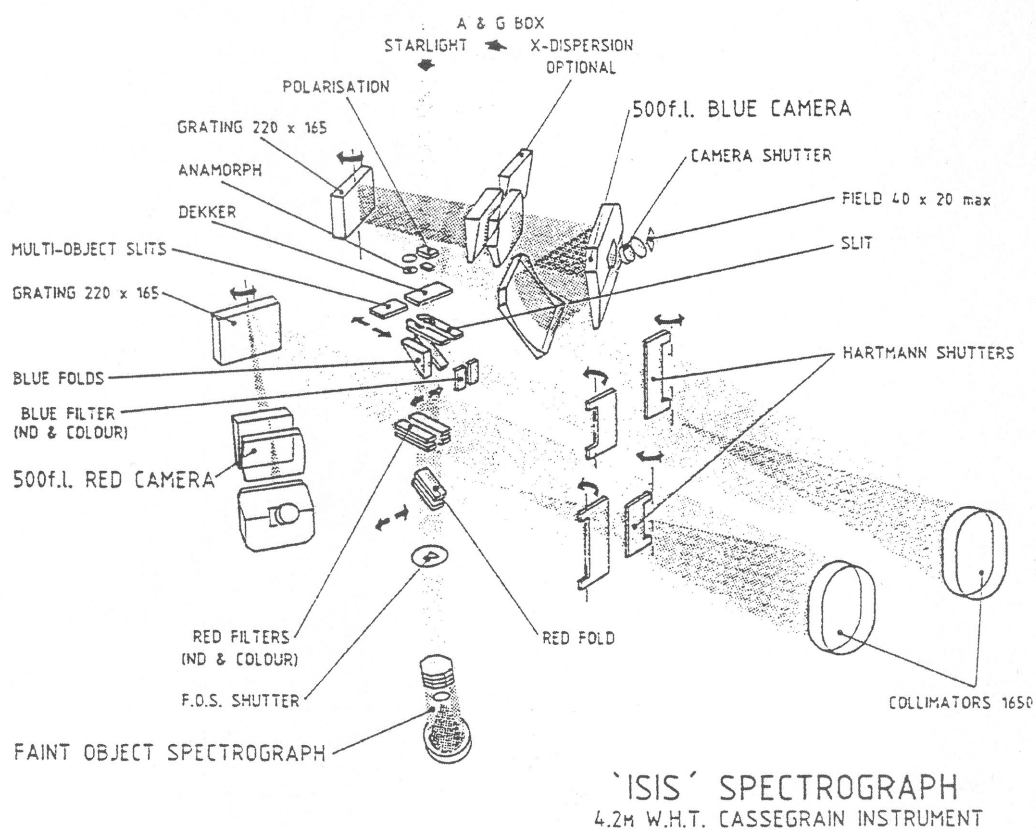


Figure 2.5: Layout of the ISIS optical spectrograph.

2.1.6 Magellen Telescope

The 6.5 m Baade and Clay telescopes (Shectman and Johns, 2003) were built by the Carnegie Institution of Washington at its Las Campanas Observatory in Chile on behalf of the Magellan Project, a collaborative effort by the Carnegie Institution, University of Arizona, Harvard University, University of Michigan, and Massachusetts Institute of Technology.

The work described in Chapter ?? utilised the Magellan Echellette (MAGE, see Marshall et al., 2008) spectrograph. MAGE is a single object optical echellette spectrograph for use on the Magellan Clay telescope. MAGE is a simple, fixed format spectrograph. The optical design includes a reflective collimator and a medium order reflective diffraction grating in combination with two prisms to provide cross dispersion. A f/1.4 Schmidt camera focuses the beam onto a CCD optimised for ultraviolet wavelength coverage (wavelengths blueward of 3600 Å), while maintaining high resolution and full wavelength coverage of the visible spectrum (3200 Å to 10000 Å), and providing resolutions of $R \sim 1000$ to $R \sim 8000$. The optical design of the instrument can be seen in Figure 2.6, while a solid model of the instrument can be seen in Figure 2.7.

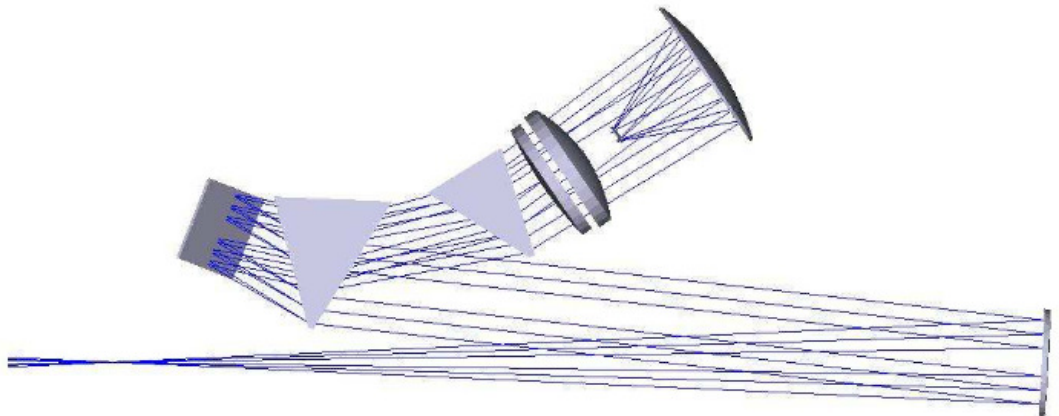


Figure 2.6: MAGE optical design.

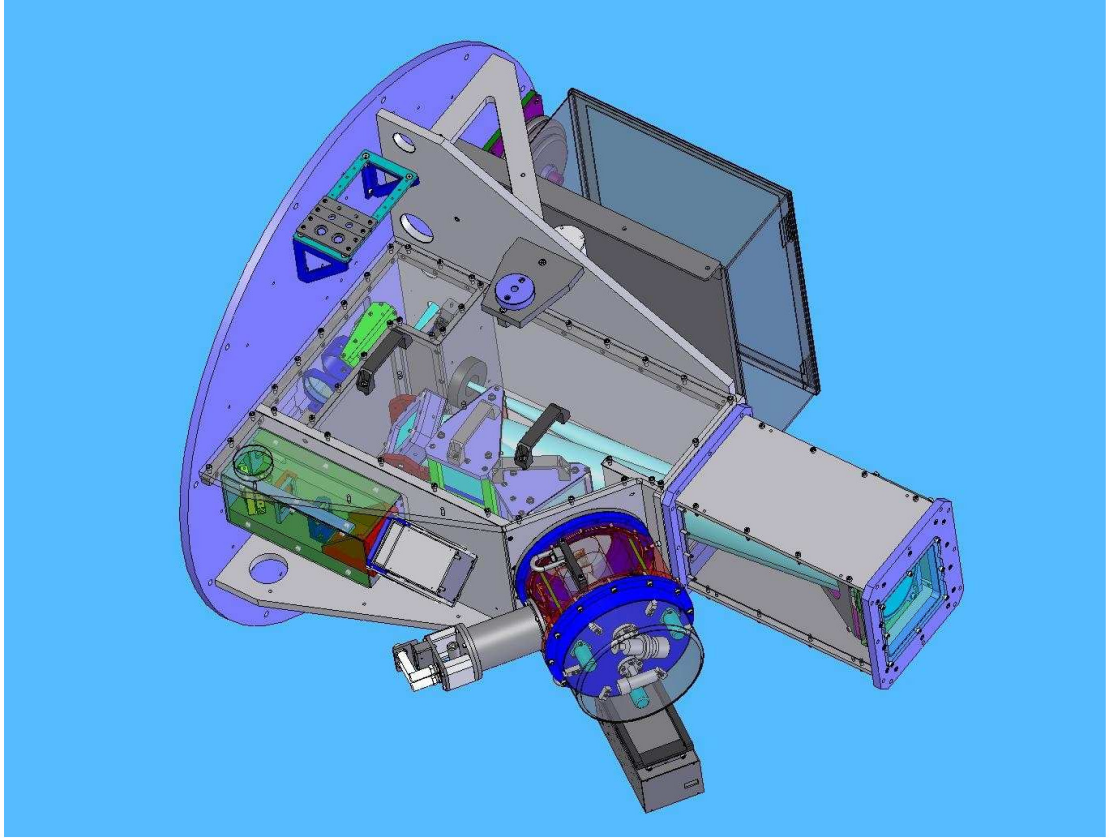


Figure 2.7: Layout of the MAGE optical spectrograph.

2.1.7 Gemini Telescope

The Gemini Observatory consists of two 8.1 m diameter telescopes, the Gemini South telescope on the summit of Cerro Pachon in Chile, and the Frederick C. Gillett Gemini North telescope on the summit of Mauna Kea on the island of Hawaii.

The work described in Chapter ?? utilised the Near-Infrared Integral Field Spectrograph (NIFS, see McGregor et al., 2002) on the Gemini North telescope. NIFS provides three dimensional imaging spectroscopy over a 3 " x 3 " field of view in the Z- through K-bands with a resolving power of $R \sim 5000$ and was designed to work with ALTAIR, the Gemini adaptive optics systems.

The NIFS spectrograph detector is a Rockwell H2RG device with 2048×2048 pixels, and is sensitive to light out to $2.6 \mu\text{m}$. Rather than using a shutter to control

the duration of an exposure, the recorded image is the difference of two read outs of the detector, one at the start of the integration and one at the end.

NIFS is an image-slicer spectrograph which means the sky is sampled by a series of long, thin mirrors. Each of these 29 slices acts like a slit in a traditional spectrograph, providing a slice across the two dimensional field that is then dispersed to provide a spatially resolved spectrum. However the design means spatial sampling is different along each slice than across it. Along the slice, sampling is determined by the detector, while across the slice, the sampling is determined by the width of the slice as projected onto the sky. This results in rectangular pixels, called spaxels, with scale $0.103'' \times 0.043''$ across and along the slice respectively.

The JH_G0602 filter was used in conjunction with the H_G5604 grating to obtain the spectra presented in Chapter 5. The JH_G0602 filter covers a wavelength range of $1.18 \mu\text{m}$ to $1.96 \mu\text{m}$ and has a central wavelength of $1.57 \mu\text{m}$, while the H_G5604 grating covers a wavelength range of $1.49 \mu\text{m}$ to $1.80 \mu\text{m}$, has a central wavelength of $1.65 \mu\text{m}$ and provides a spectral resolution of $R = 5290$.

The optical design of the instrument can be seen in Figure 2.8 , while a solid model of the instrument can be seen in Figure 2.9.

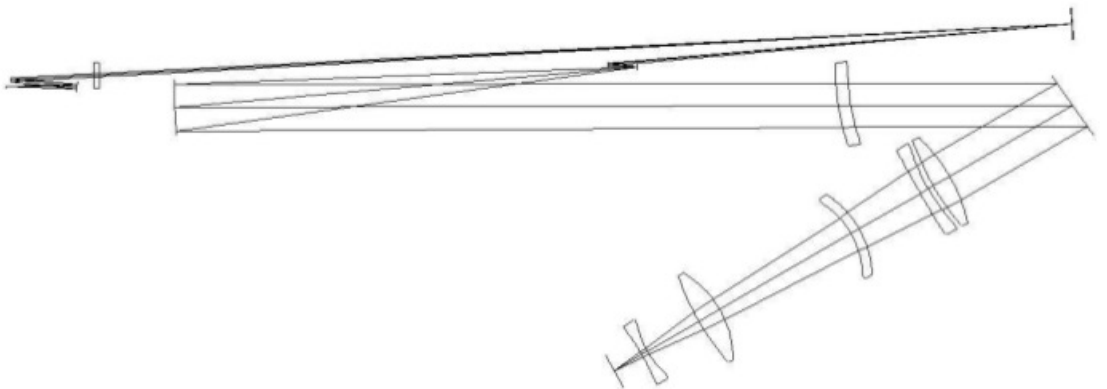


Figure 2.8: NIFS optical design.

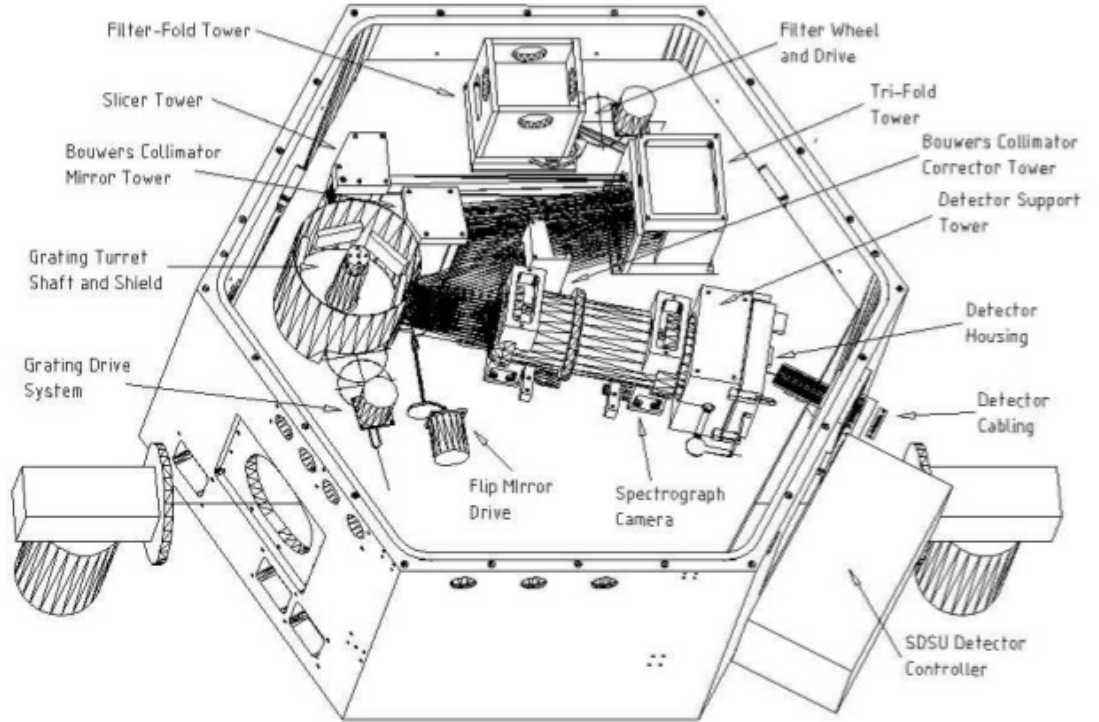


Figure 2.9: Layout of the NIFS spectrograph.

2.2 Data Reduction

Here we outline the various methods of reduction used to process our data. This includes a manual approach for reducing the spectra of PSRJ1023+0038, as well as the automated pipelines employed on the spectra of both A0620-00 and GRS1915+105. This is a necessary precursor to carrying out scientific analysis of the data as several instrumental effects are introduced when using CCDs. Detailed descriptions for removing instrumental effects and extracting spectra are given in the IRAF⁴ manuals Massey (1997) and Massey et al. (1992) respectively.

⁴IRAF is distributed by the National Optical Astronomy Observatories, which are operated by the Association of Universities for Research in Astronomy, Inc., under cooperative agreement with the National Science Foundation

2.2.1 Optical Photometry

The first processing step is to account for the bias level in the images. The bias level is an effect that arises when a ‘pedestal’ level is applied to each pixel on the CCD to ensure the electronics always records a positive number of counts. To account for this we take many zero second exposures called bias frames. These exposures are then averaged and subtracted from the science exposures.

The next data reduction step is to flat field the images. This corrects for the variation in pixel to pixel sensitivity across the CCD and involves exposing the CCD to a uniform light source. Typically this is done by projecting a light on the inside of the dome (dome flats) or by taking exposures of the night sky (sky flats) during twilight. Dome flats can be more advantageous as they can be taken at any time of the day whereas sky flats are very time sensitive. A large number of flats must be taken so as not to reduce the signal-to-noise of the science frames. These are averaged and then divided by the mean pixel value in order to normalise the response of all pixels and this normalised flat field image is then divided into the bias corrected science frames.

2.2.2 Optical Spectroscopy

Bias correction and flat fielding are common to both spectroscopy and photometry. Optical spectroscopy requires additional data reduction steps, which are outlined below.

Now that the main instrumental effects have been removed from the science data, we can move on to extracting the spectrum of the star. In order to do this we must first locate the star’s profile and trace it across the CCD. An aperture, defined as a number of pixels to the left and right of the centre of the stellar profile, is then

placed over the profile and a background region selected to take into account the sky contribution to the exposure (see Figure 2.10), which is then subtracted out. To extract the spectrum, the counts at each pixel within the aperture are summed to give the relationship between counts and pixels (in the dispersion direction).

In order to find the relationship between counts and wavelength we utilise arc lamp exposures. This involves using light of a known spectral type, in the case of PSR J1023+0038 this was a Copper-Argon (CuAr) lamp (see Figure 2.11), and extracting its spectrum in the way described above. The emission lines are then compared to an atlas of CuAr emission lines and the pixel location of the emission line is assigned a wavelength. By repeating this for several more emission lines

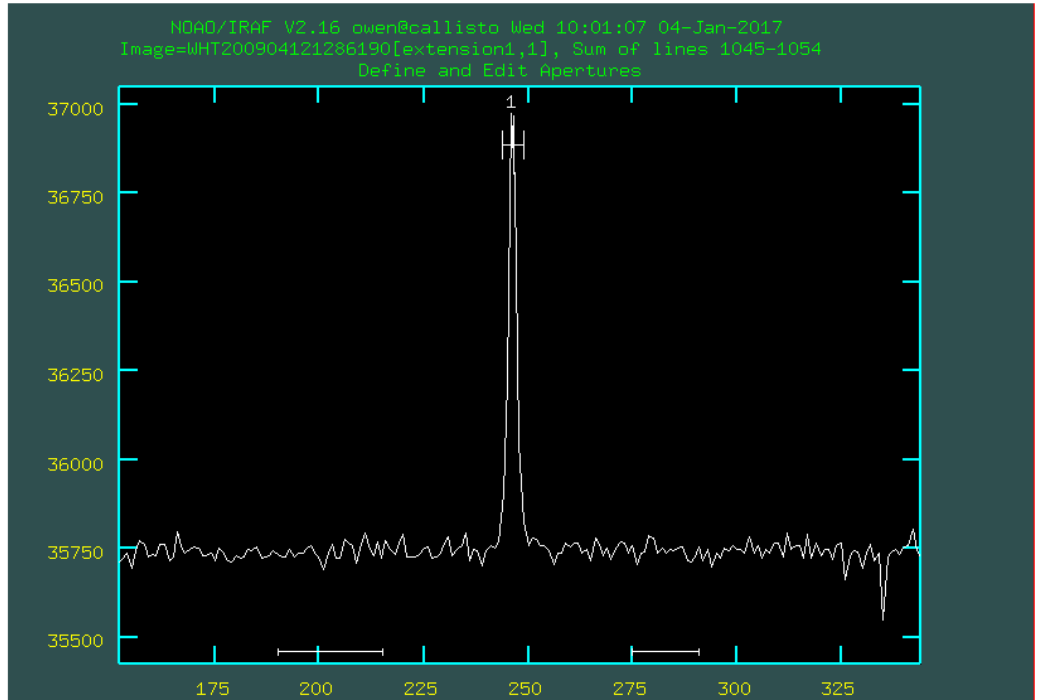


Figure 2.10: The aperture and background selected to extract a spectrum.

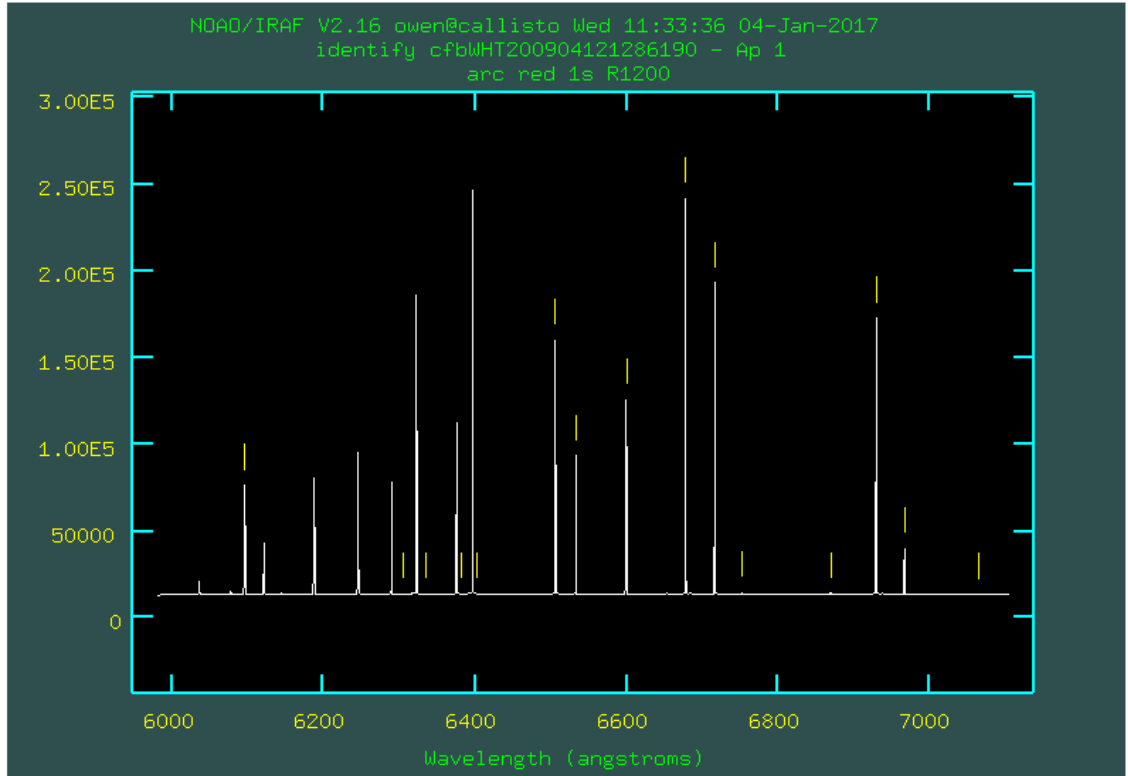


Figure 2.11: A plot of the CuAr arc lines used to wavelength calibrate the J1023 spectra.

across the CCD we can extrapolate a wavelength per pixel scale for the entire chip. This wavelength solution is then applied to the science spectra leaving us with a one dimensional, counts versus wavelength spectrum. In practice it is useful to normalise the spectrum to unity. This is achieved by fitting a polynomial to the continuum, avoiding emission and absorption lines, and dividing the spectrum by this fit. The one dimensional, wavelength calibrated spectrum is now ready to be analysed. An example of such a spectrum can be seen in Figure 2.12.

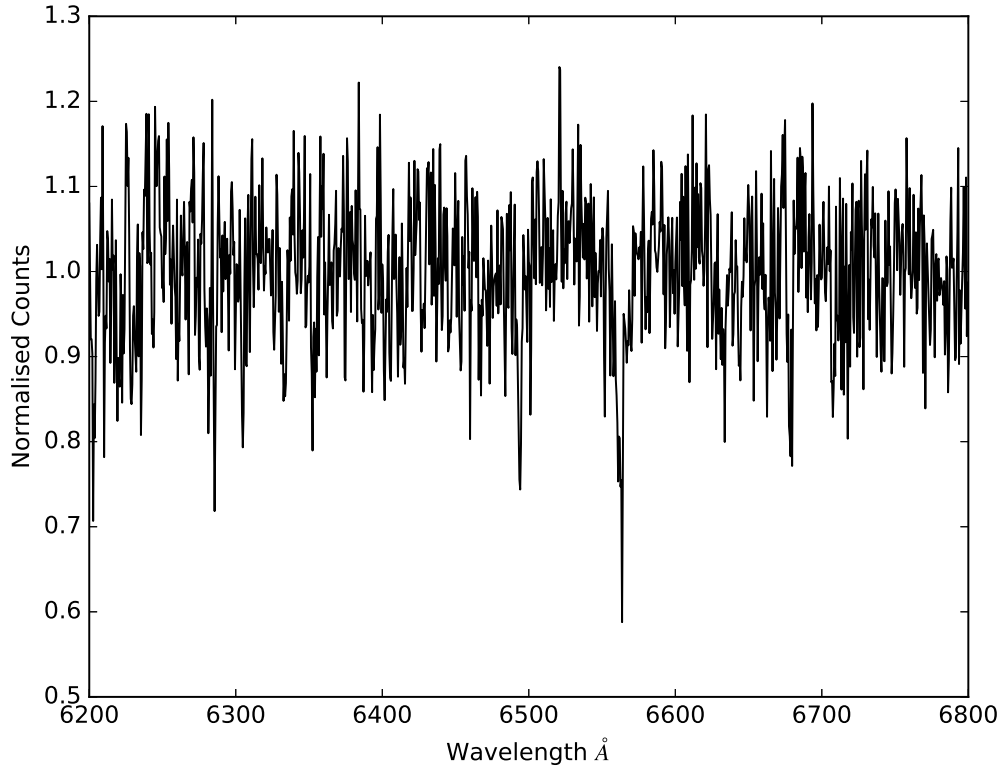


Figure 2.12: An example of a fully reduced and wavelength calibrated science spectrum of J1023.

A0620-00

Due to the design of the MAGE instrument, the standard IRAF routines for reducing optical spectra, as described previously, are not appropriate. As such, an Interactive Data Language (IDL) reduction package called MASE (MAGE Spectral Extractor, see Bochanski et al. 2009b) was developed. It incorporates bias subtraction, flat fielding, wavelength calibration, sky subtraction, object extraction and (if required) flux calibration. A Thorium-Argon (ThAr) cathode tube is used for wavelength calibration across the entire wavelength range. However, due to the extended wavelength range, two different types of flat field images are required. For the blue orders ($m \geq 14$) a Xenon (Xe) flash lamp is used, however in redder orders this is dominated

by emission lines. As such, a quartz lamp is used to flat field the red orders. It is recommended that in order to obtain a reliable normalised flat field at least ten Xe and quartz flats should be taken.

Bias Subtraction

The MAGE detector has a 128 x 128 pixel overscan region from which the median bias level is determined and subtracted from the images. Images are then trimmed to 2048 x 1024 pixels and each pixel is converted from ADUs to electrons.

Flat Fielding and Order Definition

Each flat field has a median filter applied to smooth it and remove large scale variations. The unsmoothed flat field is then normalised by its median filtered counterpart. The flat fields are then co-added to remove any pixels with a variation of two standard deviations from the mean pixel value. The separate Xe and quartz

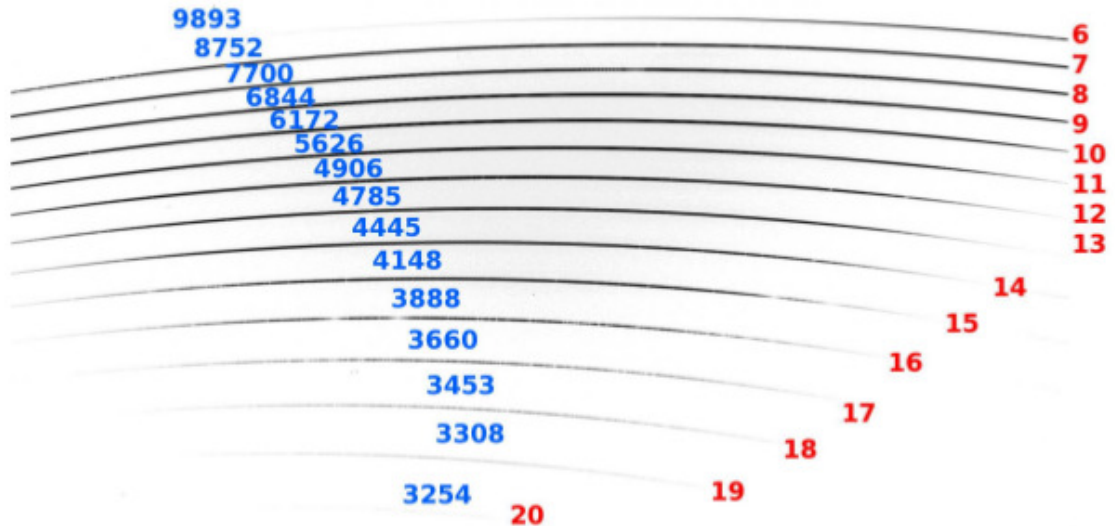


Figure 2.13: An example MAGE spectrum of a flux standard star. The central wavelengths (blue) and order number (red) are listed. Figure from Bochanski et al. (2009a).

flats are merged and the flat field correction applied. In order to define the edges of each order, trace flats are created by summing the Xe and quartz flats for each slit used. A filter is applied and a fourth order Legendre polynomial is fit to the edges of each order as a function of pixel position in the x-direction on the CCD. The coefficients of the fit define the edges, centre and width of each order on the CCD.

Wavelength Calibration

Due to the curvature of the orders the wavelength solution is obtained in two parts. First an extraction through the centre of each order extracts the one dimensional arc spectrum, in air wavelengths (the wavelength of light in air at 1 atmosphere, 15C and in dry conditions), which are compared to the ThAr atlas of Murphy et al. (2007), and a Fourier transform calculates any shift between the two. Once the lines have been identified, a low order Chebyshev polynomial is fit to identify weaker ThAr lines. A two dimensional solution is then computed to fit the wavelengths and echelle orders as a function of CCD row and order number.

The second part of the wavelength calibration deals with the tilt of the arc emission lines across the orders (see Figure 2.14). To account for this tilt, strong arc lines are fit with a straight line and the slope is used to determine the tilt as a function of position on the CCD.

Extracting the Spectrum

The target is identified and an approximate trace applied. Each order is collapsed in the wavelength direction and the spatial centre located. This traced region is then masked and a sky model created from the background. A fourth order spline is fit as a function of pixel position along the trace, offset from the centre of the order. The

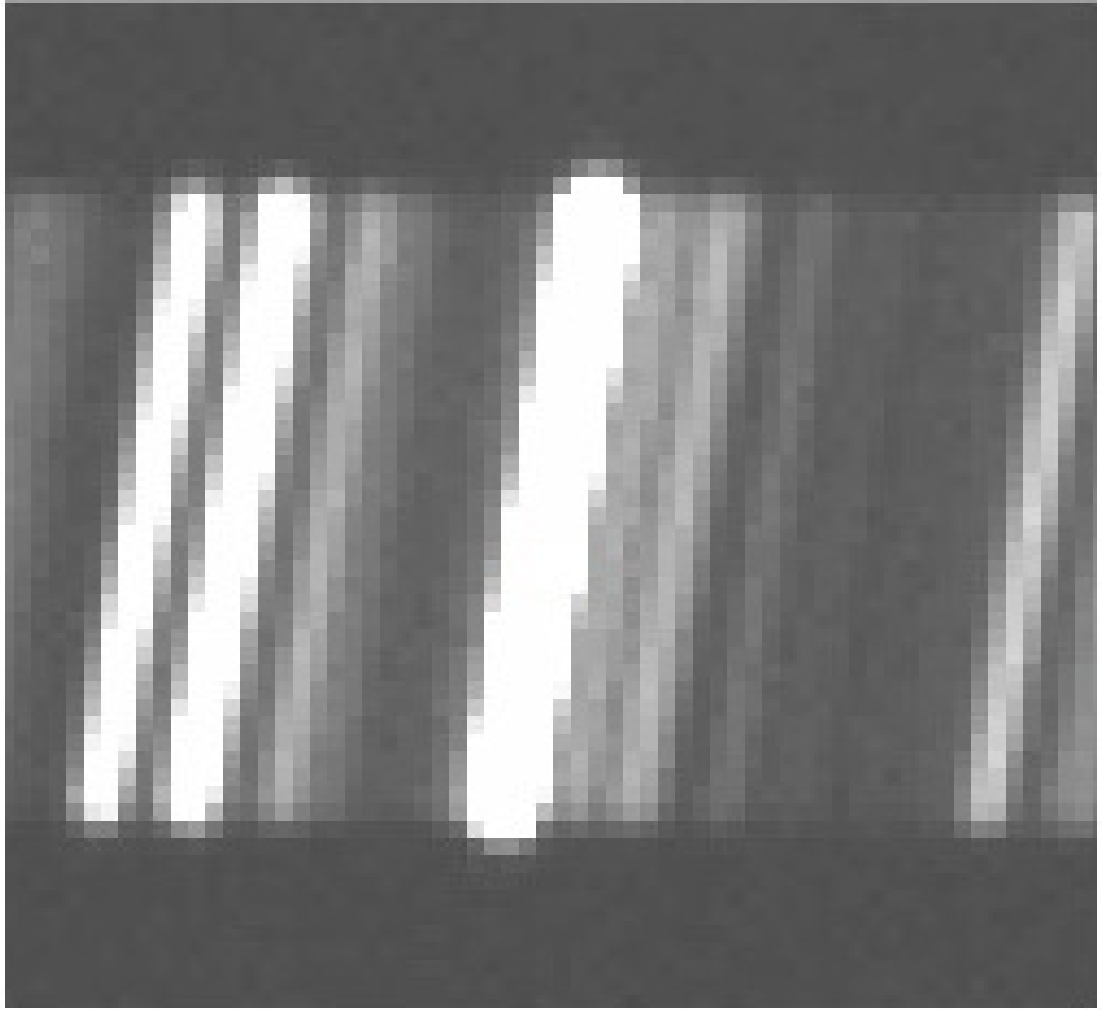


Figure 2.14: An example of the tilt observed in the arc lines.

sky model is propagated along the spatial direction using the tilt map determined previously. To refine this approximate trace, an already reduced flux standard star is used as a comparison as it is bright and therefore easier to locate and extract its spectrum. The target trace is compared to the flux standard trace and any difference corrected for. Next the dispersion axis is collapsed and counts plotted against slit height. To measure the flux of each order they are ranked by their S/N and optimally extracted - each pixel is weighted according to the fractional total flux falling on that pixel. Once the profile has been traced and the weights have been applied, splines are fit to both the sky model and the science spectrum. The initial

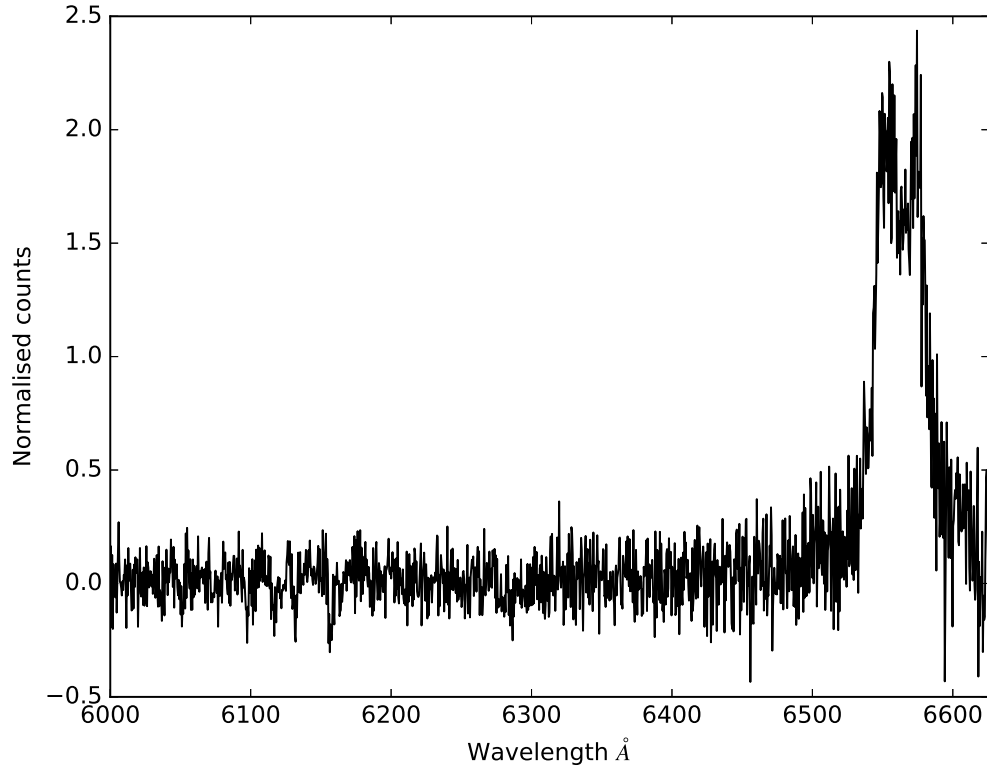


Figure 2.15: An example of a fully reduced, extracted and continuum normalised spectrum of A0620.

fit rejects pixels which deviate more than 3.5σ from the sky model. These pixels are masked out and the fit repeated, during which time the air wavelength values are converted to vacuum wavelengths, the wavelength solution is applied, and the spectra are heliocentrically corrected. Spectra are then normalised to unity, ready for analysis (see Figure 2.15).

2.2.3 IR Spectroscopy

As a result of its innovative design, the standard IRAF reduction techniques described previously are not applicable to NIFS data. Therefore Gemini have produced scripts, which make use of the GEMINI IRAF package, which can be edited by users in order

to reduce their data. This involves utilising three reduction scripts: the baseline calibration script to create dark and flat field frames and to determine the wavelength solution of the arc exposures, the telluric reduction script to reduce and extract the one dimensional spectrum of the telluric standard star observed, and finally the science reduction script to apply the calibration corrections to the science data and to extract a one dimensional spectrum of the target star. Each of these three broad stages of reducing NIFS data is now described in more detail.

Baseline Calibration

NIFS data are written as multi-extension FITS (MEF) files. The first reduction step calls the NFPREPARE task which adds data quality (DQ - used to fix hot and dark pixels) and variance (VAR) extensions to the data. As there are 29 slices, each FITS file will have a total of 87 extensions: 29 each for science, DQ and VAR. At this stage a mask definition file (MDF) extension is also added. This provides the relative location of the slices on the detector and compares this to the actual data. Any offset is stored as a new image and used subsequently to provide the location of the spectra on the detector.

The next step is to create the normalised flat field . The shift determined by the MDF is applied to all flats which are then passed through the NSREDUCE task. This task subtracts the flat field images and cuts the 29 slices into individual extensions which each have a basic wavelength solution applied. NSFLAT is then used to produce the normalised flat field image as well as a bad pixel mask (BPM) and finally, NSSLITFUNCTION is used to renormalise the slices to account for slice-to-slice variation by fitting a function in the spatial direction. The output of this task is used to flat field all further data.

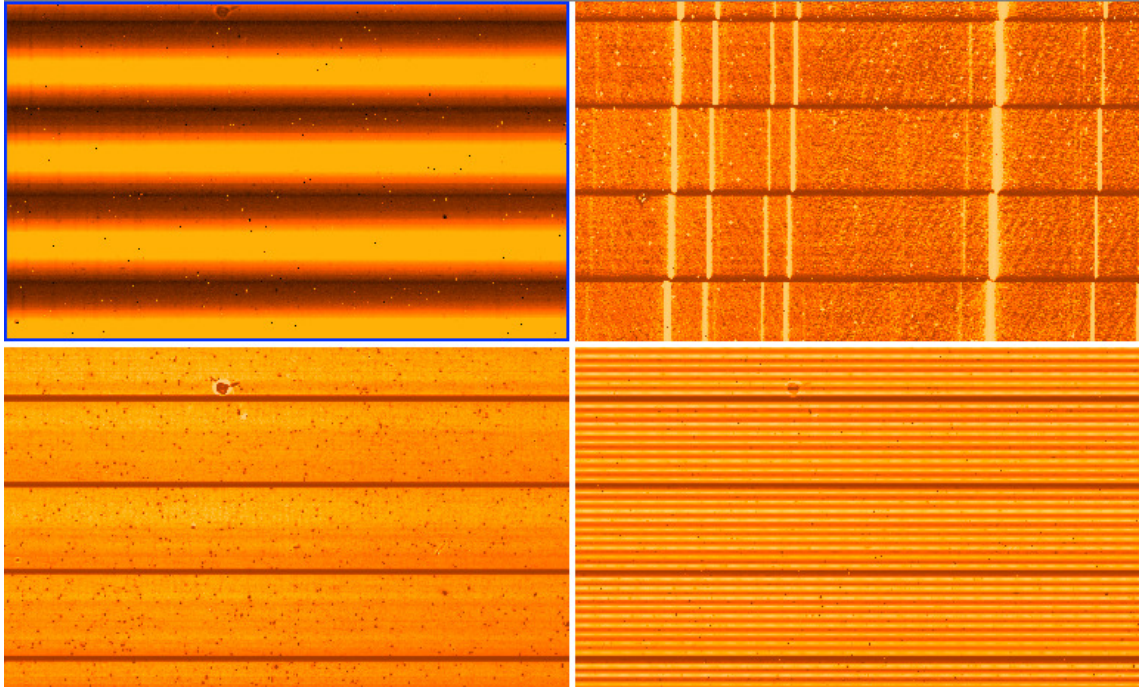


Figure 2.16: An example of typical NIFS data. Clockwise from top left these images are: science data, arc lamp, Ronchi mask and flat lamp. Clearly seen in each image is the different slices.

At this point a quick, approximate wavelength solution is applied to the arcs. This is based on information in the header file as each of the bands in which NIFS is capable of observing is identified by unique parameters stored in the header. This provides a starting point for `NSWAVELENGTH`, which determines the accurate wavelength solution. For the H-band spectra we obtained, this is done using an Argon (Ar) lamp. The routine automatically assigns a wavelength value to each pixel location of the Ar emission lines using a lookup table. Rather than applying the solution to the data itself, a database entry is created which is called later.

The final baseline calibration is to establish a spatial calibration correction using a ‘Ronchi’ mask. This accounts for distortions along the slice and is analogous to the wavelength calibration but in the spatial direction.

Telluric Correction

Telluric standard star observations are required to remove atmospheric absorption features from near-infrared spectra. When specifying the telluric standard star(s) to be observed, we must ensure the chosen star(s) have the same air mass as the average air mass of the target when they are being observed. In general, telluric standard stars are observed both before and after the target object. If the telluric standard star lies in the same field of view as the target star, these observations are trivial. However, if the telluric standard star is not in the same field of view as the target star, some care must be taken. As an example, if the science target spectrum requires two hours of observing time, acceptable before and after telluric standards would have approximately the same declination as the target but would have a right ascension of approximately one hour less than and greater than the target.

Again the first step is to run `NFPREPARE` to apply the MDF to all the telluric frames. Bad pixels are also corrected for. The sky spectrum is then subtracted from the telluric science frames and the flat field determined in the baseline calibration is applied to the science frames as well. `NSFITCOORDS` is then used to derive the two dimensional spectral and spatial transformations using the outputs of the wavelength solution and Ronchi mask respectively. The `NSTRANSFORM` task then applies the linear physical co-ordinates to each of the 29 slices, ensuring the slices are sampled in constant wavelength steps. Extraction of the one dimensional telluric spectrum is done manually using `NFEXTRACT` to define an aperture around the telluric star and summing the counts within it. The telluric star observed was the A0V star HD182761 (19h 25m 22.392s +20° 16' 18.22") and as such contains very few features intrinsic to the star itself. The few intrinsic lines it does contain are the Brackett gamma ($\text{Br}\gamma$) lines. These are removed by fitting a Gaussian to them and

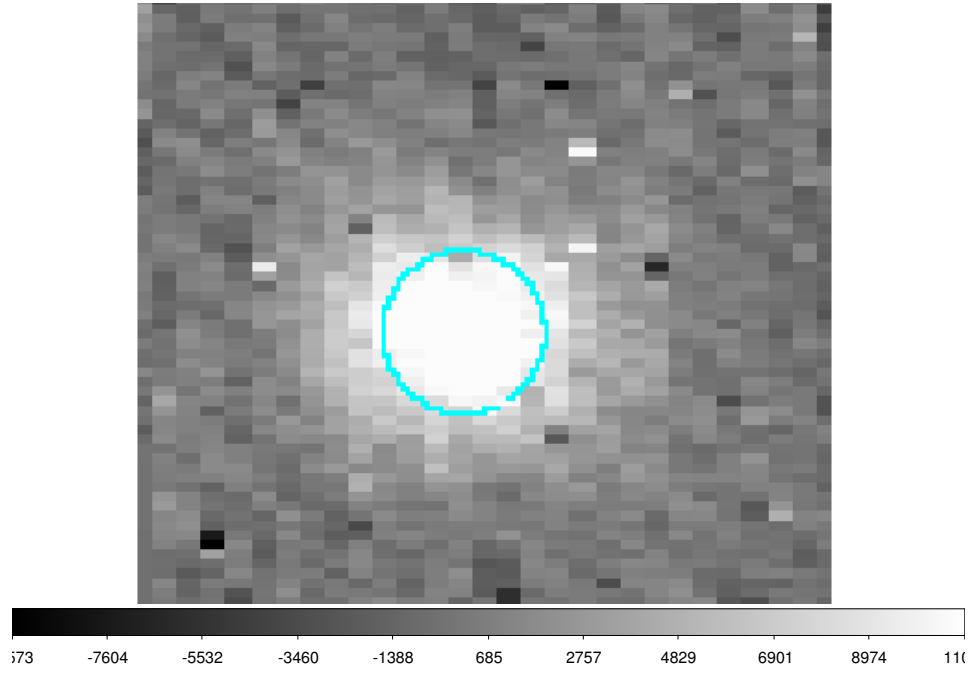


Figure 2.17: The image on which a circular aperture (in blue) is placed around the star. Counts are summed within this aperture to produce a one dimensional spectrum of GRS1915.

subtracting out the fits. This leaves a one dimensional spectrum containing only telluric absorption lines.

Science Reduction

The science reduction broadly follows the outline of the telluric reduction. The MDF and BPM are applied, science frames are sky subtracted, flat fielded and have the spectral and spatial corrections applied. NFTELLURIC is then called to correct the science frames for the presence of the atmospheric absorption lines. The one dimensional, telluric corrected spectra are then extracted in the same way as described above, using NFEXTRACT, normalised and combined to achieve one high signal-to-noise spectrum per night of observations. An example of such a spectrum can be seen in Figure 2.18.

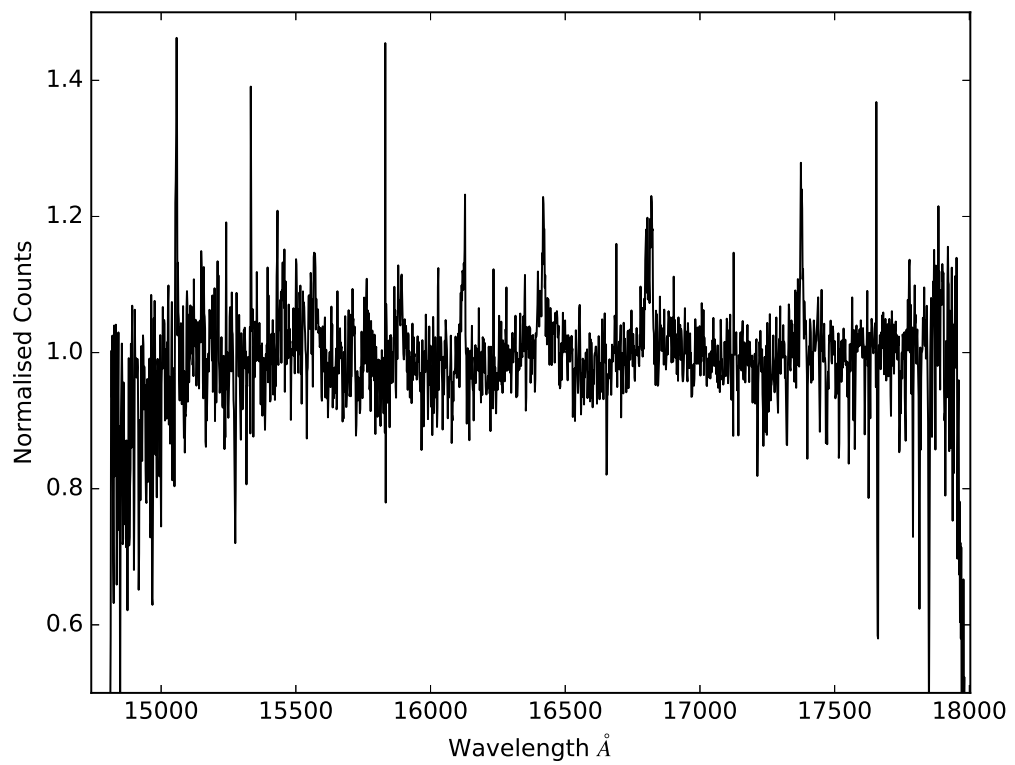


Figure 2.18: A one dimensional, fully reduced and normalised spectrum of GRS1915.

Chapter 3

PSR J102347.6 + 003841

¹ PSR J102347.6+003841 is a radio pulsar system with a spin period of 1.69 ms and an orbital period of 4.75 hours. Uniquely, it undergoes periods of transient accretion from its companion star: it occupies an important position in the evolutionary track from X-ray binary to isolated millisecond radio pulsar. Here we present a spectroscopic study of this system showing late-type absorption features which match those of a G2V star. We find a semi-amplitude of 286 ± 3 km s⁻¹ and a best fit orbital period of 0.1980966(1) days. We combine these measurements with optical photometry which suggests the secondary star may be underfilling its Roche lobe by between 15% and 20%. We weakly constrain the mass of the neutron star to be $\leq 2.2 M_{\odot}$ at the 2σ level. We also discuss the possible origins of the H α emission line in our template subtracted, averaged spectrum. Finally we present and discuss new optical photometry of J1023 taken during the recent outburst of the system.

¹Published in Monthly Notices of the Royal Astronomical Society.

Roche lobe underfilling of the secondary star in PSR J102347.6+003841? O. McConnell; P. J. Callanan; M. Kennedy; D. Hurley; P. Garnavich; J. Menzies Monthly Notices of the Royal Astronomical Society 2015 451 (4): 3468-3472

3.1 Introduction

PSR J102347.6+003841 (hereafter J1023) is a radio pulsar with a spin period of 1.69 ms and an orbital period of 4.75 hours. It was discovered by Bond et al. (2002) as part of the “Faint Images of the Radio Sky at Twenty Centimeters” (FIRST) survey. The spectrum was dominated by a blue continuum, much like that of a Cataclysmic Variable (CV) star in quiescence, but with stronger than normal HeI and HeII lines, suggesting J1023 may be a magnetic CV. They also realised this system lay in the region of sky covered by the Sloan Digital Sky Survey (SDSS). They analysed the archival SDSS data and found the emission lines were double peaked, indicative of the presence of an accretion disc. Woudt et al. (2004) found a repetitive modulation of $V \sim 0.45$ mag about a mean of $V \sim 17.5$ and an orbital period of 4.75 hours. They also detected low amplitude flickering, suggesting on-going mass transfer.

J1023 was observed again by Thorstensen and Armstrong (2005) (hereafter TA05) where they found only late-type absorption features, suggesting a dramatic change in the system. They combined radial velocity estimates and optical photometry which lead them to conclude it was likely that the primary star had a mass greater than the Chandrasekhar limit and so it was actually a neutron star or black hole, rather than a white dwarf. This hypothesis was supported by the optical and X-ray observations of Homer et al. (2006) of J1023, also taken while in quiescence, as they were unable to explain the observed X-ray emission in any other way.

In 2009 Archibald et al. detected radio pulsations from the system which confirmed the primary was indeed a neutron star and as such J1023 was confirmed as a LMXB. They combined their binary parameters with the radial velocity measurements of TA05 to estimate the mass ratio of the system, q , to be 7.1 ± 0.1 . Radio eclipses were also detected, and, assuming the inclination lies in the range $34^\circ < i <$

55° , as the line of sight between the pulsar and Earth does not intersect the Roche lobe of the companion (Archibald et al., 2009), they concluded these must be caused by material being forced off the companion star by a pulsar wind, as seen in other similar systems (d’Amico et al., 2001; Hessells et al., 2011).

In June 2013 J1023 became radio quiet (Stappers et al., 2013), suggesting, once again, that the system had undergone a transition in state. They saw a dramatic increase in the γ -ray flux which along with the softer X-ray spectrum of Patruno et al. (2014) and the re-emergence of double peaked emission lines as seen by Halpern et al. (2013) confirms accretion, specifically via a disc, has begun again in J1023.

The discovery of J1023 as a millisecond pulsar when in quiescence makes the system extremely interesting, especially given the double peaked emission lines seen in 2002 and from 2013. The history of the system suggests J1023 undergoes periods of transient accretion from its companion star and, as such, it occupies an important position on the track from LMXB to isolated MSP. Here we present analysis of archival optical data, combined with new optical photometry, and attempt to more tightly constrain the dynamical properties in this important system.

3.2 Observations and Data Reduction

The Isaac Newton Group (ING) archival data of Rodriguez-Gil and Santander presented here were taken using the Intermediate dispersion Spectrograph and Imaging System (ISIS) optical spectrometer on the 4.2 m William Herschel Telescope at La Palma, Canary Islands (see Chapter 2). The red arm of ISIS is equipped with a 4096 x 2048 pixel array with an image scale of $0.22 \text{ arcsec pixel}^{-1}$ and the high resolution R1200R grating with a dispersion of $0.26 \text{ \AA pixel}^{-1}$ was used.

The observations consisted of 26 600 s individual exposures obtained during the

night of April 12 2009 and cover the whole orbital period. We combine this with the photometry of TA05 to better constrain the binary parameters. Data were reduced using the standard IRAF routines for bias and sky subtraction, flat fielding and wavelength calibration. The data were then exported to the MOLLY² package where they were rebinned onto a common velocity scale for analysis.

We also obtained photometry of J1023 in the V-band using the 1.8m Vatican Advanced Technology Telescope (VATT, see Chapter 2) located at Mount Graham International Observatory (MGIO) on April 29 2014. The images were taken using the VATT4K CCD with a typical exposure time of 15 s. A total of 329 images were taken. The images were reduced using the standard IRAF routines for flat fielding and bias subtraction, and the relatively uncrowded field was analysed with the PHOT command in the DIGIPHOT package. We also obtained three nights of V-band photometry in June 2014 using the STE3 CCD on the 1.0 m telescope at the South African Astronomical Observatory (SAAO, see Chapter 2). A total of 63 300 s exposures were taken and reduced and analysed in the same way as the VATT data. In both cases differential magnitudes were found using two stars, from TA05, in the same field of view as the pulsar: a $V = 14.86$ magnitude comparison star and a $V = 17.40$ magnitude star as a check.

3.3 Results

The spectral type of the secondary star was estimated by performing a χ^2 fit to our selection of G-type stars. The results are displayed in Table 3.1 while Figure 3.1 shows the average pulsar spectrum along with our choice of template.

²<http://www2.warwick.ac.uk/fac/sci/physics/people/marsh/software>

The radial velocities of the individual spectra were found through cross-correlation with a high signal-to-noise G2V template spectrum observed on the same night as the target spectra. The wavelength range used was 6200 Å - 6800 Å (excluding

Name	Spectral Type	χ^2
HR6538	G1V	34.023805
BD+08 2015	G2V	21.4970827
HR1262	G5V	37.3525085
HR159	G8V	38.4522552

Table 3.1: The range of G-type stars used in the optimal subtraction process described in the main text. We note the minimum χ^2 occurs for a G2V star.

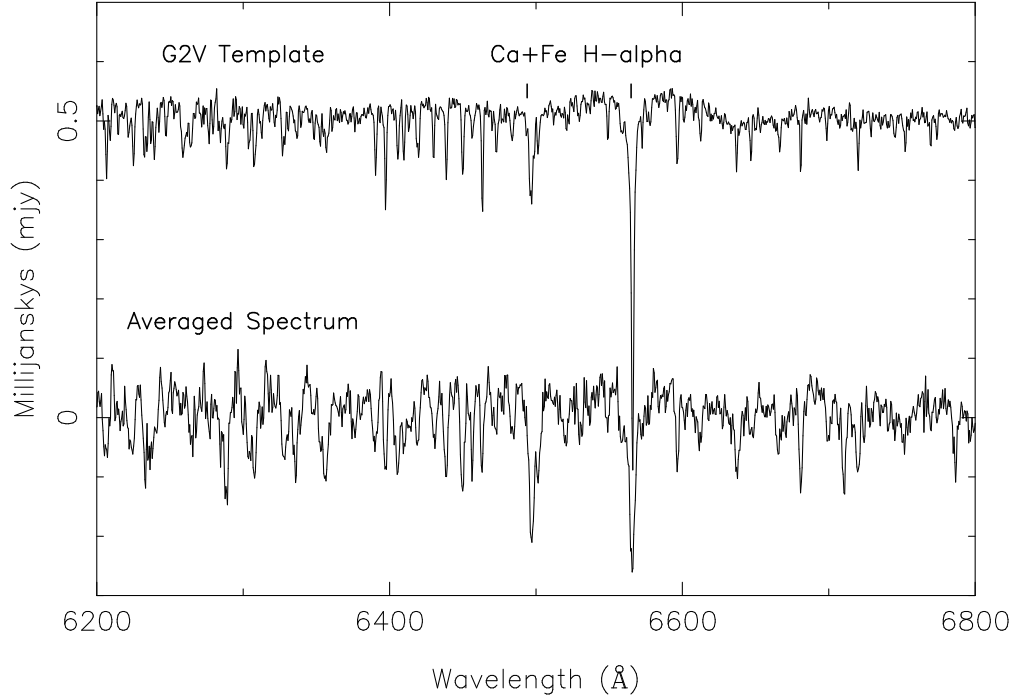


Figure 3.1: The average of all 26 spectra is shown below and the G2V template used for cross-correlation is shown on top. The two most prominent absorption features, the Ca+Fe blend and H-alpha lines, are labeled. The data have been shifted to the rest frame of the secondary.

the $H\alpha$ region) and the cross-correlation was carried out using the XCOR routine in MOLLY and FXCOR in IRAF. Figure 3.2 shows the radial velocity curve obtained through the cross-correlation technique. A sine wave fit yields a systemic velocity of $\gamma = 0.45 \pm 1.6 \text{ km s}^{-1}$, in good agreement with TA05, and a semi-amplitude of $286 \pm 3 \text{ km s}^{-1}$ for K_2 compared to $268 \pm 4 \text{ km s}^{-1}$ found by TA05. However our value of K_2 supersedes theirs as our spectra are of a higher resolution (1 \AA compared to their 3.5 \AA) and due to the better sampling of our radial velocity curve.

In order to refine the orbital period of TA05 we used the O-C method described by Bevinton and Robinson (2003) (see Appendix B). This resulted in a best fit orbital period $P = 0.1980966(1)$ days at the 1σ confidence limit. This improves on

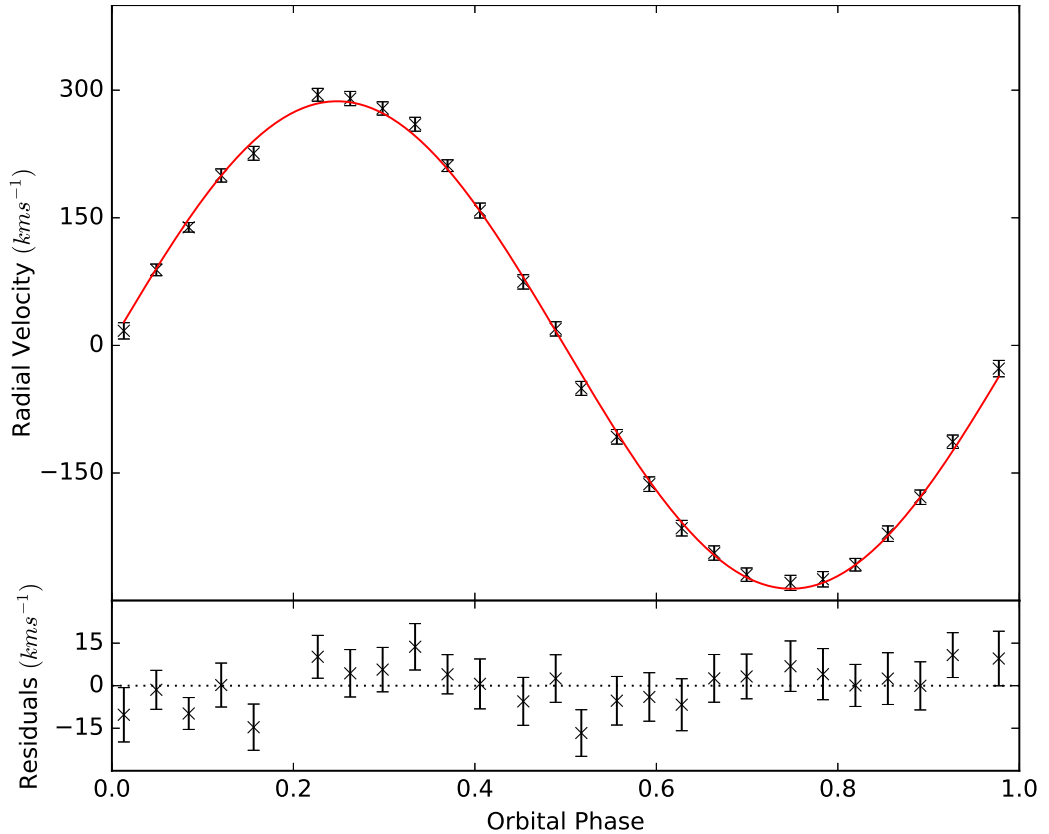


Figure 3.2: Radial velocity curve folded over the best fit period of $0.1980966(1)$ days.

Error bars have been scaled to achieve a fit with a reduced $\chi^2 = 1$.

the value found by TA05, however not on the value found by Archibald et al. (2009) of 0.1980962019(6) days which was obtained through timing measurements of radio pulsations of the pulsar.

Using our K_2 and orbital period we estimate the mass function (see Equation 1.7), $f(m_2)$, to be $0.48 \pm 0.02 M_\odot$.

3.4 An Eclipsing Light Curve Model

We next attempted to constrain the system parameters by utilising the Eclipsing Light Curve Code, (ELC; see Appendix A), of Orosz and H.Hauschildt (2000), to simultaneously fit the V-band light curve of TA05 and our new radial velocity curve. A Monte Carlo Markov Chain (Tegmark, 2004) was used to determine errors. The bounded free parameters were the Roche lobe filling factor, f , the effective temperature of the secondary, $5570 \text{ K} < T_{eff} < 5750 \text{ K}$ (in line with a G2V spectral type), the irradiating luminosity of the pulsar, $L_x = 10^{33} - 4 \times 10^{34} \text{ erg s}^{-1}$ (where the upper limit is determined by the spin down luminosity of the pulsar), the mass ratio of the system, $7.0 < q < 7.2$ (we adopted the mass ratio of Archibald et al. (2009), 7.1 ± 0.1), and the inclination of the system, $36^\circ < i < 55^\circ$. The upper bound on the inclination comes from previous estimates of Archibald et al. (2009) while the lower bound comes from noting that, for a fixed K_2 , period and mass ratio, the calculated mass of the primary is entirely dependent on the inclination of the system (see Equation 1.8), and an inclination of less than 36° gives a primary mass greater than $3 M_\odot$, the maximum theoretical mass of a neutron star (Chamel et al., 2013). The albedo of the secondary star was set to 0.5, in keeping with the star being a low mass (e.g. $\sim 0.2 M_\odot$ for a $1.4 M_\odot$ primary), convection dominated star as noted by Deller et al. (2012).

The results can be seen in Table 3.2, with the fit to the V-band shown in Figure 3.3. The left panel in Figure 3.4 shows the correlation between the inclination of the system and the filling factor of the companion. The inclination here is higher than the $44^\circ \pm 2^\circ$ inferred from Deller et al. (2012) however they have a higher mass for the neutron star which assumed a Roche lobe filling secondary. As we have allowed the Roche lobe filling factor of the secondary star to vary, we are only able to provide an upper limit to the mass of the neutron star. The limits are $1.4 M_\odot$ at the 1σ level and $2.2 M_\odot$ at the 2σ level. This can be seen in the right panel in Figure 3.4 which shows the correlation between the mass of the neutron star and the filling factor of the companion.

It is worth noting that our modelling assumes the secondary star has a convective envelope which, given the evolutionary history of the system, may not necessarily be the case. We note that a radiative envelope changes the optical modulation by approximately 0.1 magnitudes which would have a significant effect on the parameters estimated here.

In stellar mass stars the fusion of Hydrogen to Helium occurs via the proton-

Free Parameters	Results
f	$0.83^{+0.03}_{-0.02}$
i	$54^{+1^\circ}_{-5^\circ}$
T_{eff}	5655 ± 85 K
L_x	$9.9^{+0.4}_{-1.6} \times 10^{33}$ erg s $^{-1}$

Table 3.2: Results of the ELC modelling for the secondary star underfilling its Roche Lobe.

proton chain, which results in a shallow temperature gradient. This means the cores of low mass stars are radiation dominated, while the temperature in the stellar envelope is low enough that Hydrogen remains neutral, and so convection dominates.

In more massive stars the fusion of Hydrogen to Helium occurs via the CNO cycle. The higher temperature gradient means the core is convective while the temperature in the envelope is high enough to ionise Hydrogen, meaning the envelope is radiative.

In the case of our ELC model, a secondary star with a radiative envelope would be intrinsically brighter than a star with a convective envelope. This would change the amplitude of the optical light curve, which in turn would have a significant impact on the parameters.

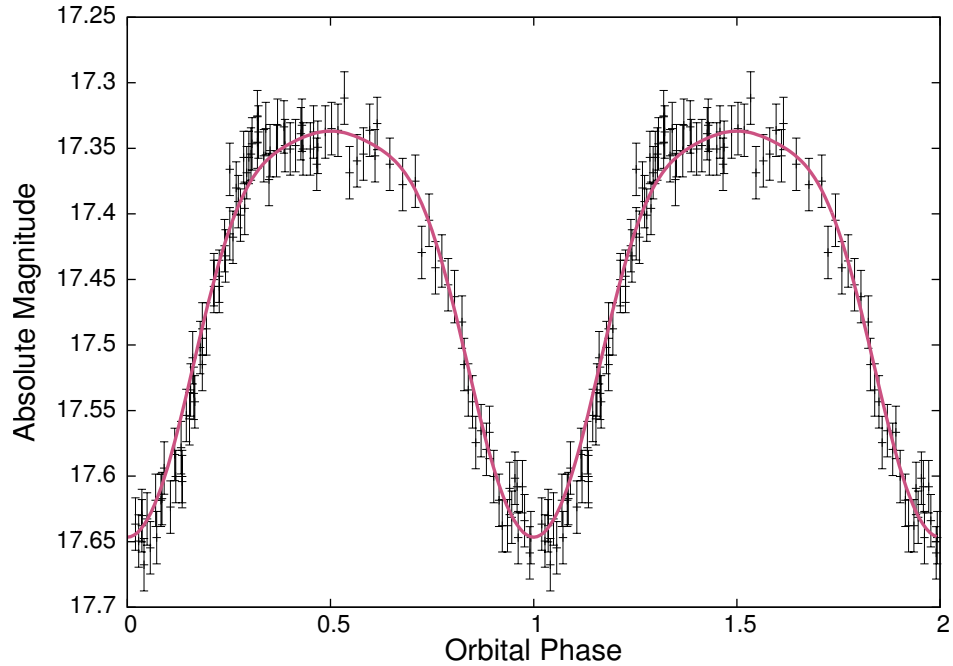


Figure 3.3: Results of our Roche lobe underfilling modelling of J1023 using ELC and the V-band photometry of TA05. Data are repeated for clarity.

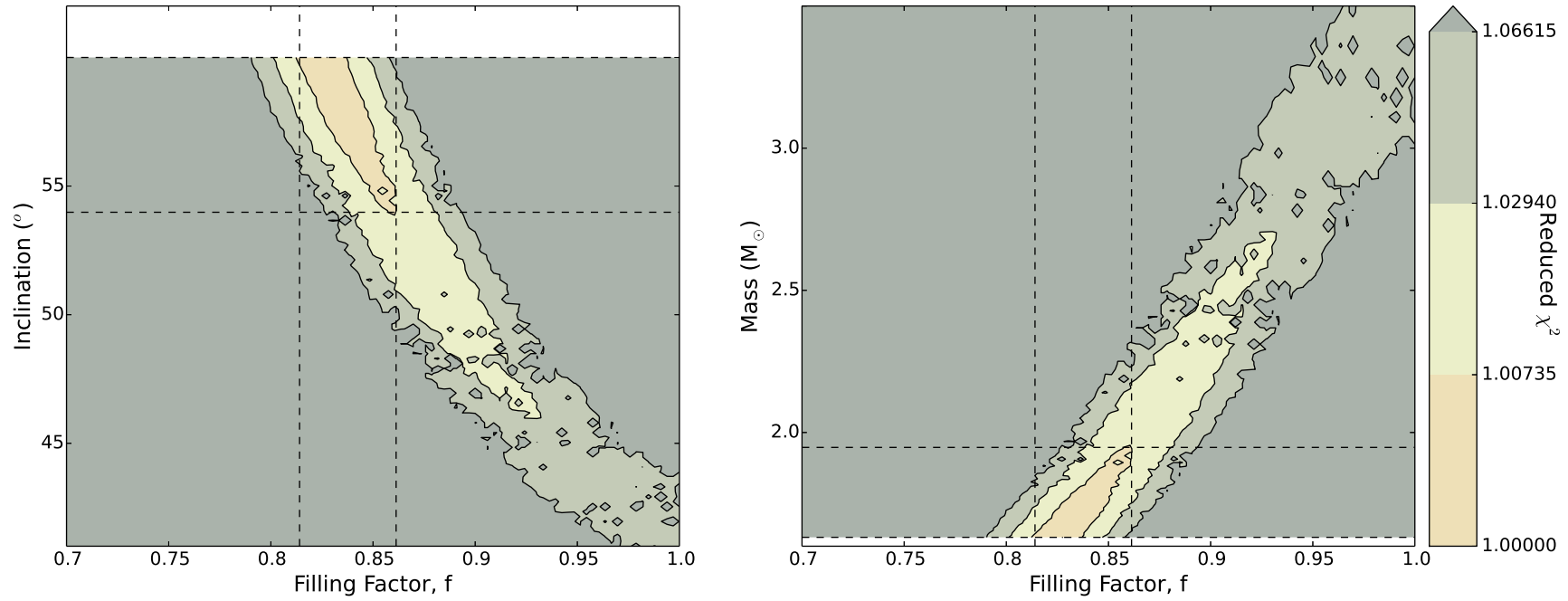


Figure 3.4: The left panel shows the inclination of the system against the Roche lobe filling factor of the secondary star and the right panel shows the mass of the primary against the filling factor. The contours here represent constant values of reduced χ^2 and the dashed lines are the 1σ confidence limits. The χ^2 minimum occurs at 135.88 which corresponds to a reduced $\chi^2=1$.

We also investigated the effects of veiling on the light curve (for example, due to a constant contribution from an accretion disk). For a Roche lobe filling factor of one we require a relatively high veiling (of order 100%, or twice the observed minimum flux) to best match the observed data. However, this is not consistent with veiling constraints we obtain from spectroscopic measurements: these provide an upper limit of 30% for a G2V template.

By using a temperature of 5655 K for a G2V star and radius of the companion star as computed by ELC of $0.39 \pm 0.07 R_{\odot}$, we found the absolute magnitude of the companion should be 6.88 ± 0.07 , which is in good agreement with the absolute magnitude of 6.84 ± 0.07 , calculated using a distance to the system of 1368^{+42}_{-39} pc from Deller et al. (2012) and using an extinction of 0.14 in the V band.

3.4.1 Residual H α Emission

The cross-correlation, averaging of the J1023 spectra and optimal subtraction of the template spectrum resulted in a residual H α emission line with equivalent width $(-1.3 \pm 0.2)\text{\AA}$ (where the error was found by varying the continuum level when fitting the emission line) and can be seen in Figure 3.5. To estimate the K_2 of the H α emission line we cross-correlated and optimally subtracted the template spectrum from each of our 26 individual exposures to produce a radial velocity curve of the emission line. We found a K_2 of $290 \pm 4 \text{ km s}^{-1}$ which is consistent with the absorption line value ($286 \pm 3 \text{ km s}^{-1}$), which suggests that the source of the residual emission is from the secondary itself, possibly an irradiated inner hemisphere. Alternatively as discussed in Gonzalez-Hernandez and Casares (2010), and the references therein, the measured equivalent width is consistent with H α emission due to a chromospherically active secondary star.

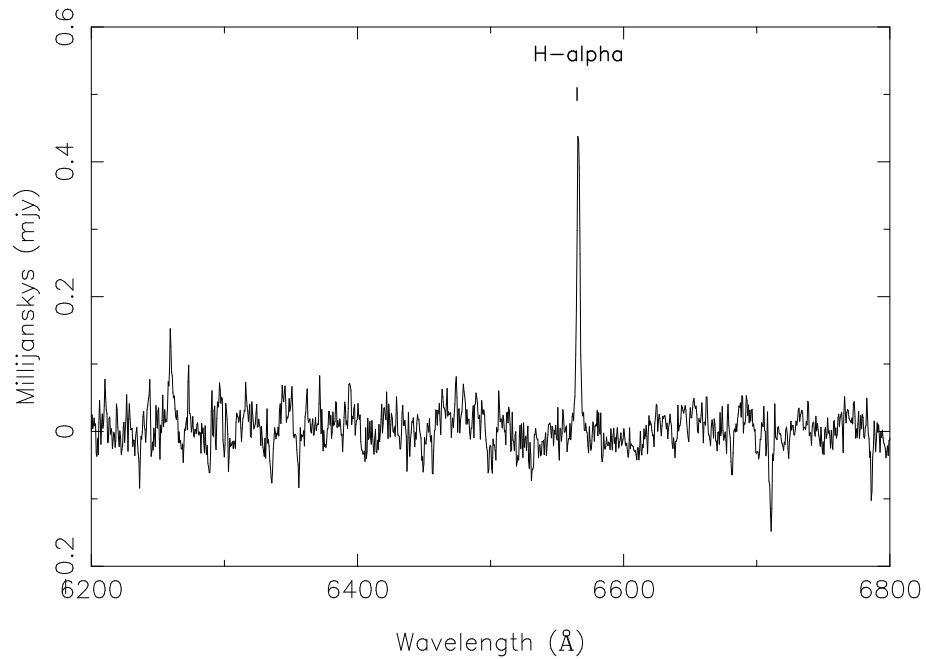


Figure 3.5: The residual H α emission seen as a result of the optimal subtraction.

3.5 A Change in State

As stated in Section 1, J1023 reverted back to its accretion phase in June 2013. We obtained optical photometry of the system over three nights (2014 June 6, 12 and 13) using the 1 m telescope at the South Africa Astronomical Observatory (SAAO, see Chapter 2). This was combined with a single night’s observation (2014 April 29) at the Vatican Advanced Technology Telescope (VATT, see Chapter 2) at the Mount Graham International Observatory (MGIO) in Arizona. Together these observations cover three quarters of the orbital period and we combine this with the V-band data of Halpern et al. (2013) which gives us complete phase coverage (Figure 3.6.)

The data indicate that the system has brightened by over a magnitude compared to the average V-band magnitude of ~ 17.5 when in quiescence.

The data suggest two types of behaviour in this state: one appears as a somewhat smooth, albeit asymmetric light curve, with minimum at phase zero, whereas during the epoch of the VATT observations, a second type of more rapid, flaring variability

is observed.

3.5.1 Comparison to Similar Systems

Long Term Variability

XSS J12270-4859 (hereafter J12270) was discovered as part of the Rossi X-ray Timing Explorer Project (RXTE) slew survey (Sazonov and Revnivtsev, 2013) and was initially classified as a CV by Masetti et al. (2006) due to the presence of optical emission lines. Further multi-wavelength observations cast doubt on this, indeed de Martino et al. (2010) noticed the position coincided with a Fermi γ -ray source (1FGL J1227.9-4852) which lead Hill et al. (2011), amongst others, to suggest that J12270 may harbour an active radio MSP. In their paper Bassa et al. (2014) describe changes in the system as it transitions from an accreting LMXB phase to that of a rotation powered MSP. They note that the optical light curve decreases by between 1.5 and 2 magnitudes while there is a corresponding decrease, by a factor of 10, in the X-ray count rate and a decrease in the γ -ray brightness, again by a factor of between 1.5 and 2. This matches J1023 very well as in its change of state from MSP to LMXB the optical luminosity increases by between 1 and 2 magnitudes from quiescence, the X-ray luminosity increases from $\sim 10^{32}$ erg s $^{-1}$ to $\sim 10^{33}$ erg s $^{-1}$ while the γ -ray flux increased by a factor of five.

Short Term Variability

Figure 3.6b shows that some of the flaring events occur on timescales shorter than the sampling time of 15s, while other, higher amplitude, flares last ~ 100 s. While in similar systems both the short and long timescale variations tend to last longer than in J1023, Hynes et al. (2002), in their study of V404 Cyg, suggest that shorter

timescale flickering may be a common feature of LMXB systems while the larger amplitude events are more difficult to explain, but may be due to instabilities in the accretion disc. Similar short and long timescale events are seen in Cen X-4 and Shahbaz et al. (2010) compared the observed colours to those predicted by three emission mechanisms: blackbody, synchrotron radiation and an optically thin layer of recombining Hydrogen. They favour this third mechanism and attribute the source of the flares to the accretion disc. However the amplitude of the flaring we observe in J1023 appears unusual in comparison to other black hole or neutron star related systems.

Archibald et al. (2010) found evidence of X-ray emission modulated at the rotational period of the pulsar. Russell et al. (2007) analysed optical/infrared (OIR) and X-ray data from 19 Neutron Star X-ray Binaries (NSXB) to compare the observed OIR and X-ray fluxes to their expected values if the OIR emission is dominated by thermal emission from a X-ray heated disc or synchrotron emission from the jet. They found that thermal emission due to X-ray reprocessing could explain all their data except at high luminosities. Synchrotron emission from the jet was found to dominate the NIR light curve above $L_x \sim 10^{36} \text{ erg s}^{-1}$ and the optical above $L_x \sim 10^{37} \text{ erg s}^{-1}$. This suggests that the flaring seen in our VATT data is not due to synchrotron emission, given the spin down luminosity of the pulsar, $L_x \sim 10^{34} \text{ erg s}^{-1}$.

3.6 Conclusions

The results of our modelling suggest that the secondary star in J1023 is underfilling its Roche lobe between 15% and 20%, albeit at the 1σ level. If confirmed, this suggests that the mode of accretion in this system is more likely to be via a wind

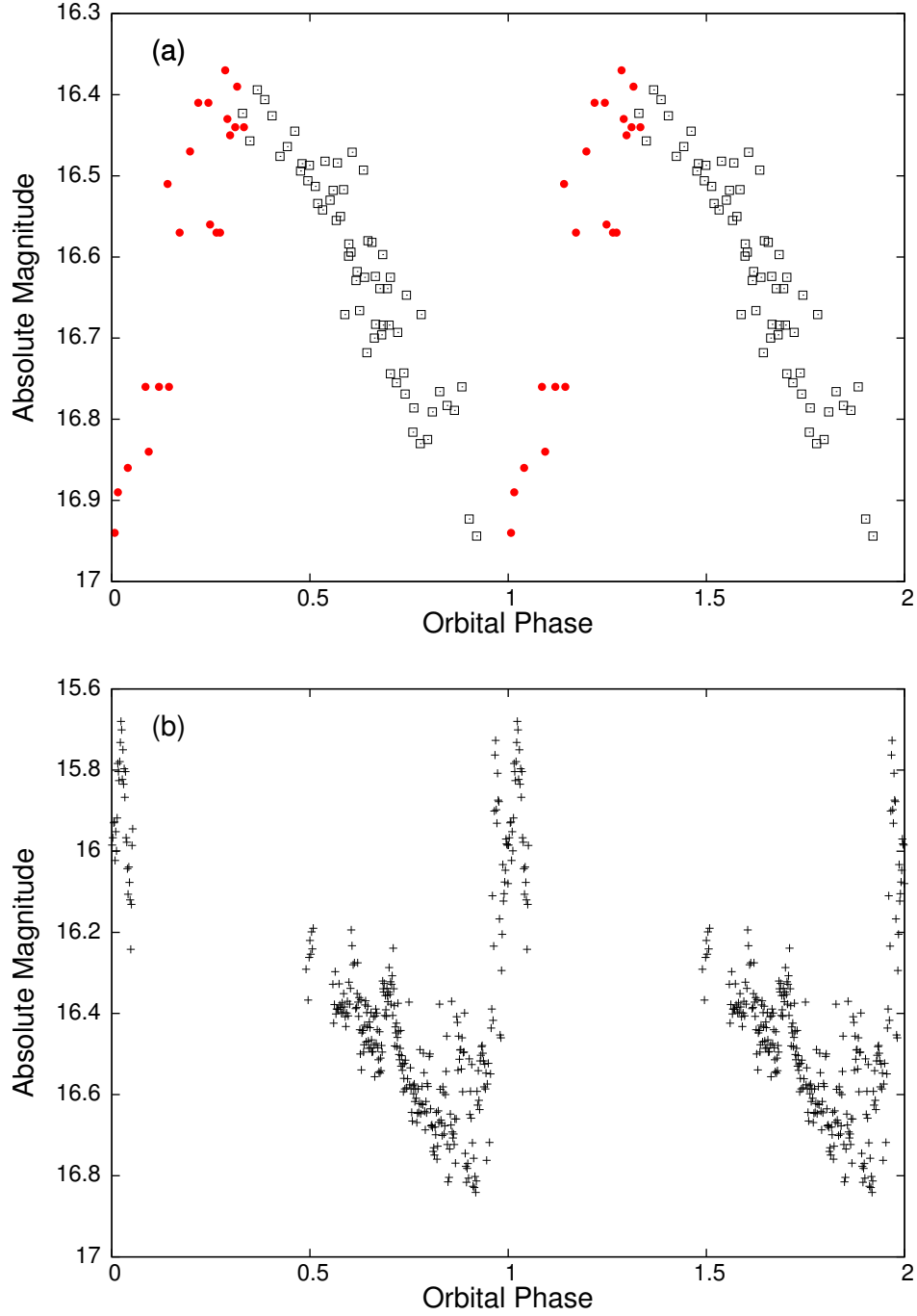


Figure 3.6: The three sets of V-band photometry taken while the system was in its recent outburst phase. Figure 3.6a shows the SAAO data (black open squares) taken using the 1m telescope on the nights of 2014/06/06, 2014/06/12 and 2014/06/13 and Atel data (red filled circles) of Halpern et al. (2013) taken using the 1.3 m McGraw-Hill telescope at the MDM Observatory on Kitt Peak. Figure 3.6b shows the VATT data taken on the night of 2014/04/29. Data are repeated for clarity.

from the secondary star, rather than Roche lobe overflow which is more commonly the case. This may in turn be related to the accreting/non-accreting transitions that have been observed from this system.

We also observe evidence for $H\alpha$ in emission in the quiescent state, which we associate with either the irradiation of the secondary star by the spin down luminosity of the pulsar, or from an active chromosphere on the secondary.

As our photometric observations of J1023 in this outburst phase have been taken over several epochs, in which only part of the orbital phase has been sampled, more systemic, multi-wavelength, observations are required. Further multi wavelength observations once it returns to quiescence are encouraged, especially phase-resolved spectroscopy and more accurate photometry to confirm the underfilling of the Roche Lobe of the secondary star, the source of the $H\alpha$ emission, and more tightly constrain the mass of the neutron star.

3.7 Additional Discussion

Since our own paper on J1023 was published, two additional campaigns in the r' -band and radio have been undertaken by other authors. Here we discuss their findings and their implications for our understanding of the system.

Shahbaz et al. (2014) undertook long-term r' -band time-resolved observations during the recent accretion/radio quiet phase. They observed both a sinusoidal modulation due to the irradiated inner hemisphere of the secondary star as well as its ellipsoidal modulation along with rapid flaring and separate large amplitude flaring events. The rapid flaring occurs on time-scales of ~ 20 s with amplitudes of 0.1 - 0.5 magnitudes while the large flare events typically occur on time-scales of up to one hour with amplitudes of 0.5 - 1.0 magnitudes. This matches our results quite

well as we see flares on time-scales shorter than our sampling time of 15 s as well as a longer time-scale flare which lasts ~ 100 s with an amplitude of ~ 1.0 magnitudes.

With the colour information they have available and assuming the flare emission mechanism is an optically thin layer of recombining Hydrogen, Shahbaz et al. (2014) show that there is a decrease in baryon density and an increase in temperature during the large amplitude flaring events. This implies the flare is hotter and more optically thin than the out of flare state. They measure the energy of the flare in the optical to be 6×10^{35} erg s $^{-1}$ - two orders of magnitude larger than flares seen in chromospherically active stars. Church and M.Balucińska-Church (2004) determined the accretion disc corona (ADC) in LMXBs extends from 20,000 km in the faintest sources to 700,000 km in the brightest, typically 15% of the disc radius. In this context Shahbaz et al. (2014) conclude the large flare arises from a large fraction of the disc, most likely the ADC.

Meanwhile Deller et al. (2015) undertook a radio imaging campaign of J1023 between November 2013 and April 2014. They observed a rapidly variable, flat emission spectrum which they say is indicative of synchrotron emission, probably due to a jet. They suggest the system undergoes propeller mode accretion with the jet removing significant fractions of the liberated energy from the system.

In the analogous system XSS J12270-4859 de Martino et al. (2014) observe emission lines in the high state which fade around superior conjunction of the secondary. At this phase they also preferentially observe flares along with randomly occurring dips. They put this behaviour down to propeller mode accretion rather than an accretion disc corona. In the low state emission lines disappear altogether, indicating the system has transitioned from accretion to rotation powered.

Similarly, IGR J18245-2452 has been observed to transition between rotation

and accretion powered states on time-scales of a few days to months (Papitto et al., 2013). Typical quiescent X-ray luminosities of $\sim 10^{32}$ erg s $^{-1}$ implies a small mass accretion rate while the presence of radio millisecond pulsations indicates the pulsar magnetosphere was preventing accretion onto the neutron star (i.e. propeller mode accretion).

Chapter 4

A0620-00

Stellar mass black holes, and their mass distribution, are important inputs in binary evolution and supernova models. However, a key limiting factor in accurate mass determination is the uncertainty in the inclination of such systems due to contamination of light from an accretion disc. This additional non-stellar light decreases the amplitude of the ellipsoidal variation observed in the light curves of these objects and manifests as an underestimate of the inclination of the system and an overestimation of the mass of the black hole. Shahbaz et al. (1999) showed the effect that including light from the accretion disc can have on the binary inclination of A0620-00 (see Figure 4.1) The ellipsoidal modulation itself results from tidal distortions of the secondary as well as non-uniform surface brightness. In order to estimate the true value of the inclination we must model only light from the secondary star and this is achieved through simultaneous spectroscopy and photometry. The veiling, or amount of light from the accretion disc, is estimated from the spectra, and the corresponding photometric observation is corrected accordingly. This modified light curve, representing the *pure* ellipsoidal modulation due to the geometry and orbit of the secondary star, can then be used to obtain a more accurate inclination of the

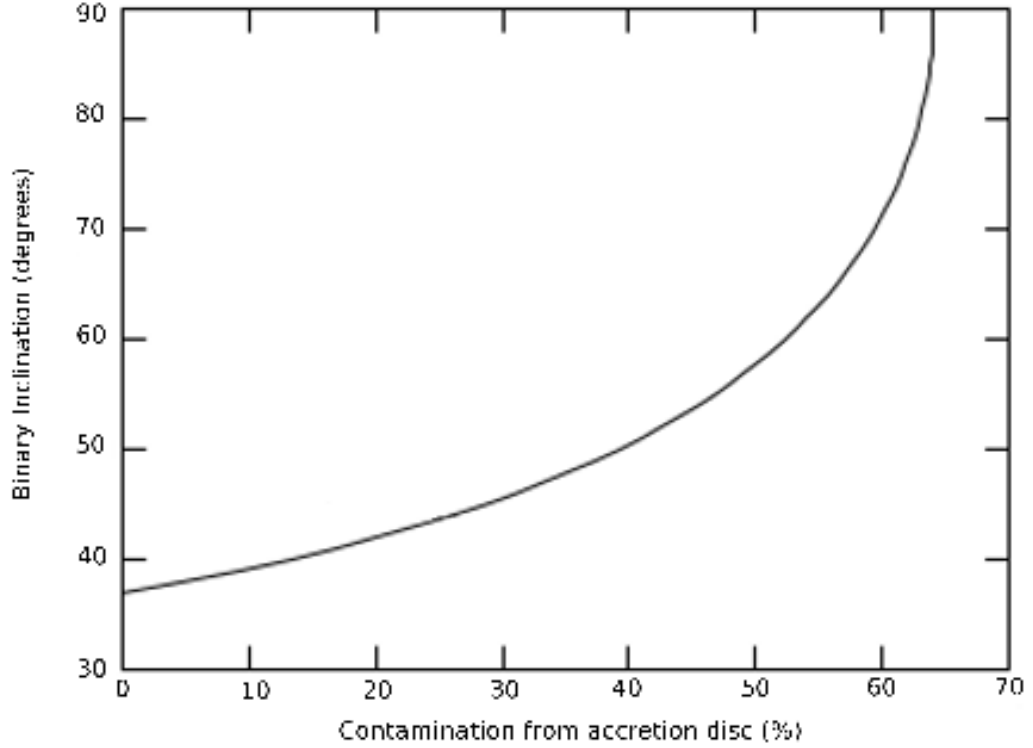


Figure 4.1: The effect of including non-stellar light on the inclination of A0620-00 found from modelling K-band spectra. Arrows indicate the 2σ upper limits on the disc contamination and inclination. Figure adapted from Shahbaz et al., 1999.

binary system and, by extension, mass of the black hole.

4.1 Introduction

The Low Mass X-ray Binary A0620-00 was discovered in 1975 (Elvis et al., 1975) and has since been classified as the prototype soft X-ray transient, a sub class of LMXBs which exhibit infrequent but intense X-ray bursts (see Section 1.2.2). Observations of the system in quiescence revealed a K-type donor star transferring mass via an accretion disc to a compact object primary (Oke, 1977). Radial velocity studies by McClintock and Remillard (1986) found a semi-amplitude of $457 \text{ km s}^{-1} \pm 8 \text{ km}$

s^{-1} , an orbital period of approximately 7.75 hours and a mass function of $3.18 M_{\odot} \pm 0.16 M_{\odot}$ which gives a lower limit of $3.2 M_{\odot}$ to the mass of the primary, making A0620-00 a black hole candidate. This has been confirmed and refined by Marsh et al. (1994) and Neilsen et al. (2008) amongst others.

A precise estimate of the mass of the primary requires an accurate estimate of the inclination of the system. Froning and Robinson (2001) found estimates of the inclination to range from 38° to 75° , implying a mass range of $3.4 M_{\odot}$ to $13.2 M_{\odot}$. A possible reason for this wide range of inclination was put forward by Cantrell et al. (2008). Their analysis of V-, I- and H-band light curves from 1999 to 2007 found three distinct states - passive, loop and active - even though the system was in quiescence throughout that time. In the passive state all observed variability is consistent with ellipsoidal variation. In the loop state A0620-00 brightens for approximately one month and traces a loop in the optical colour-magnitude diagram and exhibits increased variability on a range of timescales. Finally, the active state is when the system is typically brighter and more variable than in the loop state.

Another explanation for the range of inclination is due to the assumed disc contribution when fitting light curves. In the V-band Neilsen et al. (2008) find the disc contribution varies from 0.48 to 0.76 over their three nights of observations. In the infrared some studies have neglected the disc contribution entirely, while Froning et al. (2007) find the disc contribution to be significant, up to 19% in active state light curves. Therefore, in order to get a reliable estimate of the inclination of A0620-00 we require a better understanding of the variation in the disc contribution.

Much analysis of A0620-00 has focussed on ellipsoidal variations of the light curves in various bands and the contamination of the donor star light by the accretion disc. However, in previous work the disc contribution has been assumed to be

constant, which is clearly not the case. Estimates range significantly over all epochs of observations and even on time scales as short as night to night. With this in mind we present simultaneous V-band phase resolved spectroscopy and photometry with the aim of estimating the disc contribution at each phase of our observations and correcting our photometry accordingly. By removing the contribution from the accretion disc we should be left with the pure ellipsoidal modulation due to the motion and distorted shape of the secondary star.

4.2 Observations and Data Reduction

In the following section we briefly summarise the observations presented here, and their reduction. For a detailed treatment of the telescopes and instruments used see Chapter 2.

The V-band photometry presented here were taken using the 2.5 m DuPont Telescope located at Las Campanas Observatory, Chile on the night of March 24 2009. The images were taken using the CCD instrument with an exposure time of 240 s. A total of nine exposures were taken covering approximately one tenth of the orbital phase. The images were reduced using the standard IRAF routines for bias subtraction and flat fielding and the relatively uncrowded field was examined using the PHOT command in the DIGIPHOT package. Differential magnitudes were found using two comparison stars in the same field of view as A0620-00. The V-band magnitudes of these stars, a $V = 16.96$ magnitude comparison star and a $V = 16.55$ magnitude star as a check, were taken from the NOMAD catalogue (Zacharias et al., 2004).

The simultaneous V-band spectroscopy was taken using the 6.5m Magellan Telescope using the medium resolution ($R \sim 4100$) Magellan Echellette Spectrograph

(MAGE). Data were reduced using the MAGE Spectral Extractor (MASE) pipeline, which incorporates the entire image reduction and calibration process, including bias subtraction, flat fielding, wavelength calibration, sky subtraction and object extraction (see Chapter ??). The data were then exported to the MOLLY package, where they were rebinned onto a common velocity scale for analysis.

4.3 Analysis

The secondary stars in LMXB systems are subjected to tidal forces due to the gravitational influence of the more massive primary star. These forces are so extreme that they actually distort the shape of the secondary from spherical to tear-shaped. This effect can be most readily seen in the light curves of such systems as an ellipsoidal modulation due to the varying size of the secondary at different phases of its orbit (see Figure 4.2). At phases 0.25 and 0.75 the secondary will appear brightest as we are viewing the elongated face of the star and therefore a greater surface area. We also see two minima of differing depth with the deeper minimum occurring at phase zero and is due to the secondary passing in front of the primary.

However in systems where an accretion disc is present, like A0620-00, the ellipsoidal modulation due to the size and motion of the secondary star is more difficult to detect. This is due to the contamination of the light curve by additional light from the disc itself. In order to model the *pure* ellipsoidal modulation from the secondary we must first remove the contribution of the disc, which is achieved through simultaneous spectroscopy and photometry. The disc contribution, or veiling factor, is measured by subtracting a template spectrum of the same spectral type from the target spectrum. The veiling factor is then used to calculate the resulting change in magnitude and the light curve is adjusted accordingly, leaving only the light from

the secondary star.

Previous work which has utilised this technique (Marsh et al. 1994; Froning et al. 2011, amongst others) has done so under the assumption that the contribution of the disc remains steady over long periods of time and has given a single veiling measurement based on the averaged spectrum of their observations. However, particularly in the case of A0620-00, it is clear that the disc contribution is far from constant over time. Neilsen et al. (2008), for example, saw a change in the contribution of light from the disc of nearly 30% over the course of three nights. It is critical that the fraction of light from the disc is known accurately: any light not attributed to the secondary star included in modelling would lead to an overestimation of the black

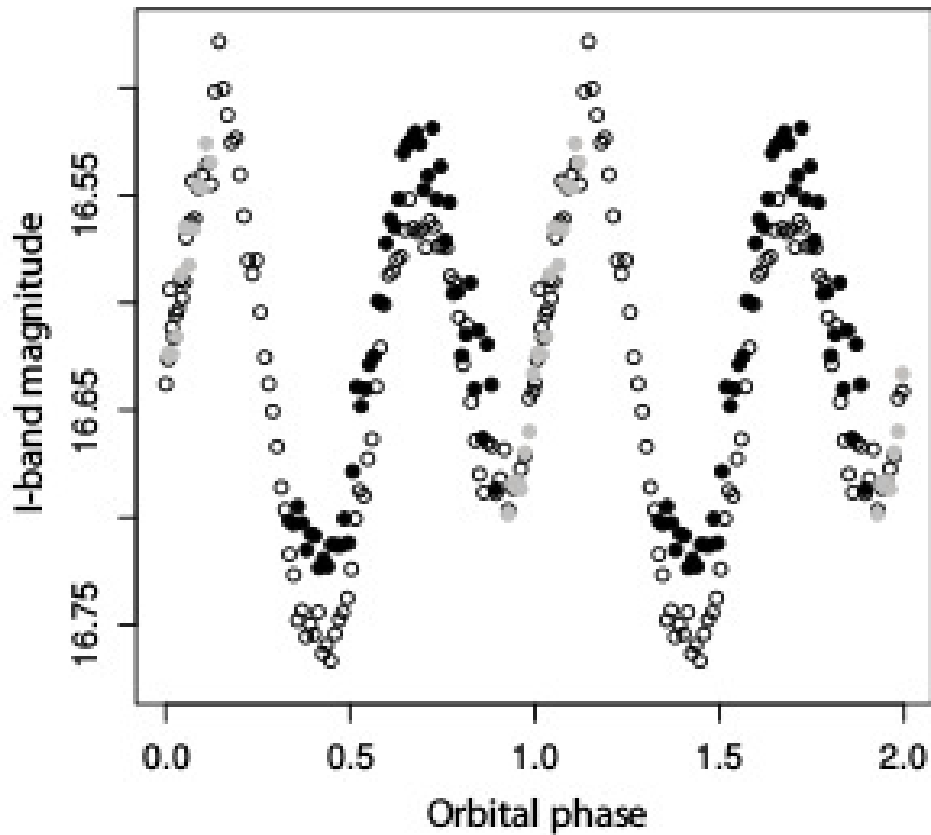


Figure 4.2: An *i*-band light curve of A0620-00 taken from Cantrell et al., 2010.

hole mass (Froning et al., 2007). We therefore proposed a proof of concept idea in which we would attempt to measure the changing veiling factor at each phase of our observations.

In order to estimate the continuum level of the disc, target spectra were fit with a first order polynomial at varying continuum levels. A χ^2 was found for each fit and the minimum taken to be the disc veiling. This was repeated for all A0620-00 spectra and the lowest χ^2 overall was set equal to one and the error spectra of the remaining spectra were scaled appropriately. The spectra were then imported to the spectral analysis software MOLLY where the continuum level was shifted according to the process described previously. The target spectra were then cross-correlated against the rotationally broadened template spectrum, HD131977, which was observed on the same night as A0620-00. The rotational broadening applied was $v \sin i = 83 \text{ km s}^{-1}$ (Marsh et al., 1994) and a linear limb darkening co-efficient of $\epsilon = 0.65$ was used (Al-Naimiy, 1978). Once the radial velocity was removed, the optimum subtraction routine in MOLLY was used to subtract the broadened template spectrum from the target spectra. This gives a factor, f , which corresponds to the fractional contribution of the secondary star to the total light of the system. The disc contribution is therefore $(1 - f)$. It is now trivial to correct our photometric observations for the veiling of the accretion disc, with the change in magnitude being given by the following equation:

$$\Delta m = -2.5 \log(f) \quad (4.1)$$

The results of which can be seen in Table 4.1.

Figure 4.3 shows the veiling and corresponding corrected photometry of A0620-00. If the ellipsoidal modulation was due to the distorted shape of the secondary we would expect to see a minimum magnitude at $\phi = 0$. However this occurs at

Orbital Phase	Secondary Contribution	Disc Contribution	Veiling Error	Corrected Magnitude	Magnitude Error
0.952	0.360	0.640	0.863	18.508	0.044
0.964	0.308	0.692	0.849	18.819	0.044
0.977	0.256	0.744	0.871	19.120	0.044
0.989	0.334	0.666	0.878	18.768	0.044
1.001	0.282	0.718	0.878	18.840	0.044
1.013	0.250	0.750	0.884	18.935	0.044
1.018	0.234	0.766	0.872	19.026	0.044
1.036	0.208	0.792	0.879	19.154	0.044
1.048	0.254	0.746	0.874	19.025	0.044

Table 4.1: The results of the veiling measurements and the resulting corrected photometry at each phase of our observations. The error on the veiling is detailed in the main text, while the error on the photometry was taken to be the standard deviation of a non-varying comparison star in the same field of view as A0620-00.

$\phi \sim 1.04$. The error on the photometry was taken to be the standard deviation of a comparison star of similar magnitude to A0620-00 in the same field of view. As described previously the error on the veiling was more difficult to estimate. It is clear however that we do not have the signal-to-noise required to make a measurement of the veiling on this short (four minute) time scale. Our (unscaled) errors are on the order of 45% per exposure and it is worthwhile noting that Froning et al. (2011) estimate an average disc contribution around $H\alpha$ to be $\pm 6\%$, based on close to 10 hours of observations. This may suggest that an increase of approximately eight in

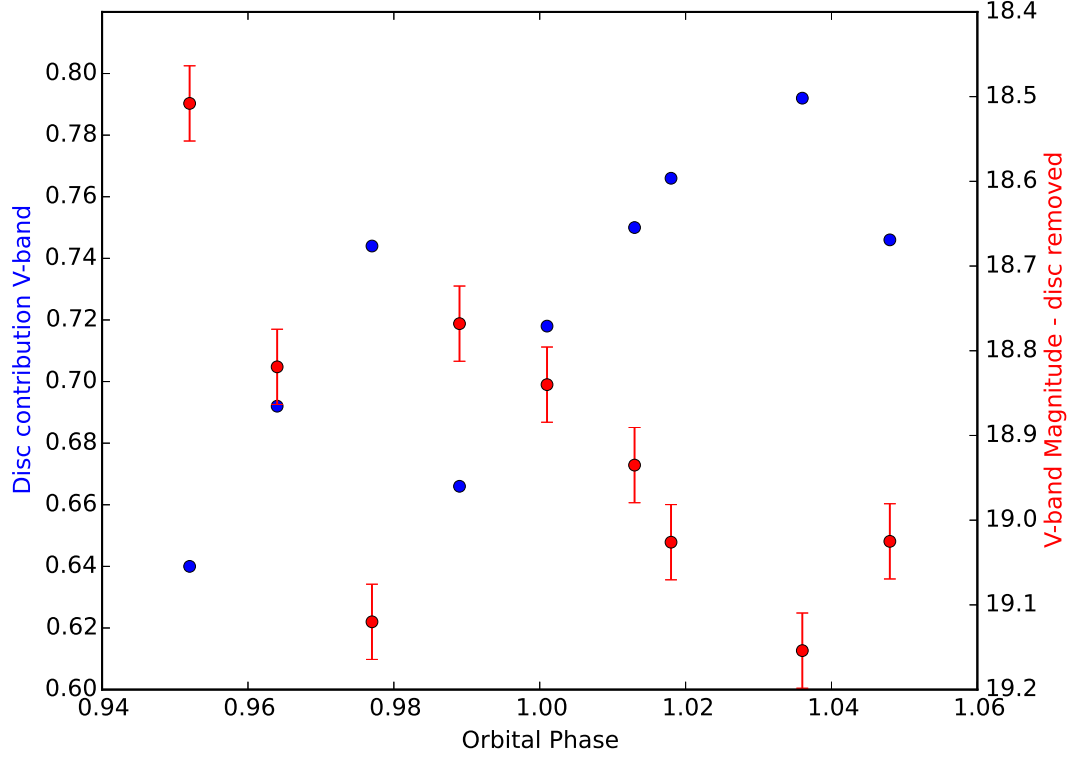


Figure 4.3: Blue filled circles show the fractional contribution of the accretion disc to the total light of the system in the V-band. The red filled circles show the V-band magnitudes after the disc contribution has been removed. The errors on the veiling have been omitted for clarity.

S/N could achieve a similar error.

It is clear that observations of A0620-00 using the 6.5 m Magellan telescope are of insufficient signal-to-noise in order to measure the changing contribution of the accretion disc throughout the orbit. The same exposure time on the VLT would lead to a signal-to-noise of approximately 14 (according to their online exposure time calculator). This is consistent with what we are already achieving with Magellan as the V-band spectra have a signal-to-noise of between eight and 13. To increase this by a factor of eight would require an exposure of ~ 5000 s on the VLT. At approaching 20% of the orbital period of A0620-00 it is clear the current largest

class of telescope is unable to carry out this proof of concept.

The next logical step would be to observe a brighter binary system. For example, the CV IP Peg has a visual magnitude of $V \sim 14.5$ (Ribeiro et al., 2007) and also harbours an accretion disc. For this magnitude and the estimated spectral type of M2 (from SIMBAD) a 240 s exposure on the VLT suggests a signal-to-noise ratio of ~ 80 would be achievable. This would seem to suggest that if a brighter object and larger telescope were used it may indeed be possible to achieve spectra with the required signal-to-noise to accurately determine the changing contribution of the accretion disc.

For fainter systems, such as A0620-00, we may have to wait until the next generation of large telescopes come online.

Chapter 5

GRS 1915+105

5.1 Introduction

GRS1915+105 (hereafter GRS1915) is a black hole X-ray transient containing a Roche lobe-filling K-type secondary star transferring material via an accretion disc onto the black hole primary. It was discovered by Castro-Tirado et al. (1994) using the WATCH all-sky monitor on board the Russian GRANAT satellite. While other such systems generally return to their quiescent state within a year (Steehhs et al., 2013), GRS1915 has remained in outburst since its discovery. The long orbital period of ~ 34 days is thought to be what has sustained the long outburst period (Truss and Wynn, 2004). A large orbital period allows a large accretion disc to form containing enough material to maintain the outburst over the past 20 years. Indeed GRS1915 has been frequently observed at near-Eddington luminosities and displays X-ray variability across a wide range of time scales. Belloni et al. (2000) identified 12 variability classes based on the count rates and colours of 163 observations from the Rossi X-ray Timing Explorer (RXTE). To date most work has focused on short time-scale variability, which is thought to be caused by instabilities in the accretion

disc and by heating by the central source. The mechanism causing longer term ($\gtrsim 100$ days) aperiodic variation, however, is more poorly understood, although may be due to dynamical evolution in the outer disc (Truss and Wynn, 2004).

GRS1915 is classified as a microquasar, the galactic equivalent of Active Galactic Nuclei (AGN), and as such the most distinguishing of its features are the parsec-scale radio jets (Mirabel and Rodríguez, 1994). These jets are believed to be powered by the spin of the black hole which has been measured to be spinning at or near the maximum rate (Narayan and McClintock, 2012) and which lead to GRS1915 being the first galactic source to display super-luminal motion (Castro-Tirado et al., 1996). The study of microquasars like GRS1915 is important, therefore, not only for our understanding of how jets form around black holes, but also allows an insight into the evolution of AGNs.

Due to its close proximity to the galactic plane the system suffers from high optical extinction ($A_v \sim 20$; Chapuis and Corbel, 2004) and as such observations in the infrared have been crucial. Greiner et al. (2001a) used H- and K-band infrared spectra to identify the spectral type of the companion as a K-MIII star and in a second paper, Greiner et al. (2001b) estimated the mass of the black hole to be $14 M_\odot \pm 4 M_\odot$ (using an inclination of $70^\circ \pm 2^\circ$ found by Fender et al., 1999) making it one of the largest stellar mass black holes in the Milky Way. This mass estimate has been revised several times recently. A radial velocity analysis by Hurley et al. (2013) based on previously unpublished VLT spectra, combined with a reanalysis of the data presented by Greiner et al. (2001a), refined the black hole mass to be $12 M_\odot \pm 1.4 M_\odot$. Steeghs et al. (2013) also performed a dynamical study of GRS1915 using the X-shooter spectrograph on the VLT. They found a black hole mass of $10.1 M_\odot \pm 0.6 M_\odot$ based on a distance estimate of 11 ± 1 kpc. The parallax distance

estimate of $8.6^{+2.0}_{-1.6}$ kpc of Reid et al. (2014) provides the most recent mass estimate of $12.4^{+2.0}_{-1.8} M_{\odot}$.

Here we present near-infrared (NIR) H-band spectra obtained in 2010 and 2013 using the Gemini North Near-Infrared Integral Field Spectrometer (NIFS). Much work in the NIR has been focussed on radial velocity studies of the absorption lines of the secondary star and, while we carry out a similar study, the presence of Brackett gamma ($\text{Br}\gamma$) Hydrogen emission lines allows us to perform an emission line analysis as well. We also present a reanalysis of the H- and K-band spectra of Steeghs et al. (2013). We compare and discuss the change in emission line profiles between the two epochs of the observations and search their K-band spectra for the phase dependent emission of the CO band heads as reported by Hurley et al. (2013). We provide an estimate of the veiling in the H-band, refine the orbital ephemeris and give an estimate of \dot{P} which we compare to theory.

5.2 Observations and Data Reduction

The near-infrared observations of GRS1915 were obtained with the integral field spectrograph NIFS (McGregor et al., 2002) on the Gemini North telescope under the programmes GN-2010A-Q-72 and GN-2013-Q-53. Up to this point previous work on this object has mainly focused on K-band observations of molecular absorption lines (e.g. see Castro-Tirado et al., 1996, Greiner et al., 2001a,b). In 2010 we obtained three test exposures of GRS1915 in the H-band in the hope that the atomic absorption lines here, which are intrinsically narrower, would provide more accurate estimates of the system parameters. We obtained more time in 2013 to carry out further observations, which cover more of the orbital phase (see Table 5.1).

As discussed in Chapter ??, NIFS provides three dimensional imaging spec-

Date	Phase	No. of Exp	Total (s)	Spectral Property
2010 Jun 29	0.59	24 x 180	4320	Absorption
2010 Jul 06	0.79	24 x 180	4320	Absorption
2010 Jul 13	0.99	24 x 180	4320	Absorption
2013 Jun 22	0.76	18 x 120	2160	Both
2013 Jun 30	0.99	18 x 120	2160	Absorption
2013 Jul 01	0.02	15 x 120	1800	Absorption
2013 Jul 03	0.09	18 x 120	2160	Both
2013 Jul 05	0.14	9 x 120	1080	Both
2013 Jul 15	0.44	16 x 120	1920	Both
2013 Jul 18	0.53	18 x 120	2160	Both

Table 5.1: List of observations of GRS1915 from 2010 and 2013. The total exposure time for each night, the orbital phase and whether the spectra are dominated by absorption lines only or both absorption lines and emission lines is shown.

troscopy with a spectral resolving power of $R \sim 5000$ over a $3.0'' \times 3.0''$ image field in the Z- through K-band spectral regions. Our science data consisted of 24×180 second exposures per night in 2010 and differing numbers of 120 second exposures in 2013 (defined by the varying weather) averaged together resulting in a typical signal to noise of ~ 20 in 2010 and ~ 13 in 2013. The data were reduced using the tasks contained in the IRAF GEMINI NIFS package. The reduction (see Chapter ??) consisted of sky subtraction, flat fielding, interpolating over bad pixels, spatial rectification using the Ronchi mask and wavelength calibration. The spectra were corrected for telluric features using the A0V star HD189920, after first removing

Date	Phase	Date	Phase
2010 Jun 09	0.99	2011 Apr 21	0.33
2010 Jul 09	0.88	2011 Apr 21	0.62
2010 Jul 11	0.93	2011 May 01	0.68
2010 Jul 13	0.99	2011 May 03	0.80
2010 Jul 27	0.41	2011 May 07	0.86
2010 Aug 02	0.58	2011 May 09	0.98
2010 Aug 10	0.82	2011 May 13	0.12
2010 Aug 19	0.08	2011 Jun 13	0.89
2010 Aug 27	0.32	2011 Jun 15	0.95
2010 Aug 30	0.41	2011 Jun 24	0.21
2010 Sep 19	0.99	2011 Jul 17	0.89
2010 Sep 24	0.17	2011 Aug 04	0.42
2010 Oct 07	0.53		

Table 5.2: List of VLT observations of GRS1915 from Steeghs et al. (2013). The date and orbital phase are listed and the total exposure time for each night was 2400s. All spectra show both emission and absorption lines.

the Br γ lines. One dimensional spectra were then extracted using the `NFEXTRACT` task and combined using `GEMCOMBINE` giving one spectrum of GRS1915 per night of observation. A summary of our observations can be seen in Table 5.1, while a summary of the VLT observations can be seen in Table 5.2.

5.3 Results

Gemini NIFS Data

After the raw data had been processed by the NIFS data reduction pipeline the resulting one dimensional spectra were imported into the spectral analysis software MOLLY. Here the data were heliocentrically corrected and phased using the ephemeris of Steeghs et al. (2013):

$$T_0(\text{HJD(UTC)}) = (2455458.68 \pm 0.06) + (33.85 \pm 0.16)E.$$

where T_0 is the time of inferior conjunction and E is the epoch of observations.

The spectra can be broken down into two classes: those spectra that show only absorption lines and those that show both absorption lines and emission lines (see Figure 5.1).

In order to determine the radial velocities of the absorption lines of the secondary star the spectra of GRS1915 were cross-correlated against a K1III template star taken from the high resolution catalogue of Lebzelter et al. (2012). All spectra were first continuum normalised to zero and binned onto a common velocity scale before the emission lines from the accretion disc were masked out to exclude them from the cross-correlation. To our surprise we did not find the radial velocities we expected based on the phase of each spectrum. In an attempt to address this problem we investigated the telluric correction by over-plotting our science and telluric spectra, which indicated that the telluric correction was poorer for the longer wavelength part of the spectrum of GRS1915. We therefore extended the mask to include these regions of poor telluric correction and repeated the cross-correlation. Once again, however, the radial velocities did not follow a sinusoidal variation. We then investigated two other possible sources of error: the arc calibration solution and deviation of the skylines from their expected wavelengths. The RMS of the

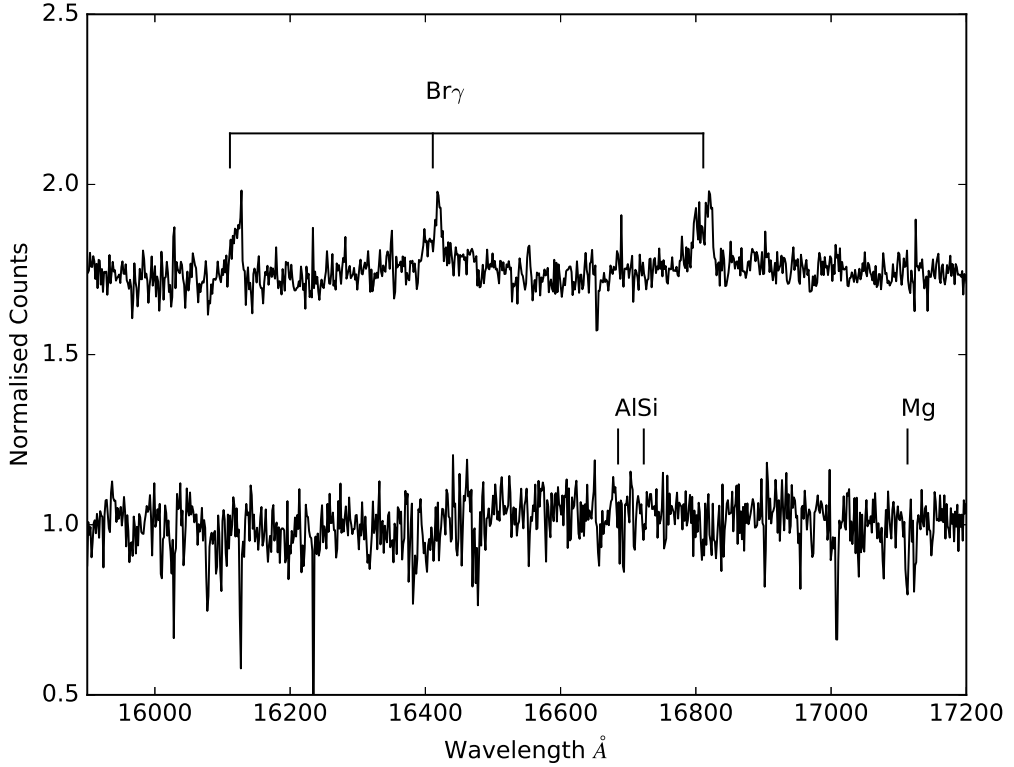


Figure 5.1: Examples of NIFS spectra showing only absorption lines (bottom, showing some of the lines included in the cross correlation) and both absorption and emission lines (top).

wavelength calibration was within the expected error range (as stated by Gemini data reduction handbook) of between 0.05 \AA to 0.15 \AA (i.e. a maximum error of $\sim 3 \text{ km s}^{-1}$ in the H-band) for the Argon arc lamp used to calibrate spectra in the H-band. The sky spectra for each night were then extracted and wavelength calibrated in the same way as the science spectra. They were then cross-correlated against a comparison H-band spectrum of the night sky and we found that our sky spectra differed from the expected wavelengths by between -13 km s^{-1} and -14 km s^{-1} . However, correcting for this shift did not account for the deviation of the radial velocities from their expected values as the shift was not systematic but varied from spectrum to spectrum.

Contact with the Gemini Helpdesk facility lead to updating both the version of IRAF as well as the GEMINI IRAF package. The raw data were then re-reduced, exported to MOLLY and cross-correlated as previously. Again, however, we encountered the same problem. It was then suggested that we migrate to the recently developed *Ureka* package. *Ureka*, a collaboration between the Space Telescope Science Institute and Gemini Observatory, is a collection of astronomy software centred around Python and IRAF and is specifically designed to work with the data reduction packages offered by both organisations. Another re-reduction and reanalysis of all spectra proved just as unsuccessful in producing a radial velocity curve. A final reduction was carried out on the recently developed NIFS Python data reduction pipeline. Again, another reanalysis did not reveal the expected radial velocities.

We contacted Steeghs et al. (2013) and they supplied us with their JHK X-shooter data with the hope that reproducing their radial velocity analysis of the absorption lines in the H-band would help in our own study of the NIFS spectra. We also looked to perform an analysis of the emission lines in the H-band, something they had not undertaken, and to compare their K-band spectra to that of Hurley et al. (2013), specifically to see if they also found phase dependent emission of the CO band heads. Included in the data made available to us was a mask used for their cross-correlations. This covered several additional regions of the H-band than our mask and so we added them and once again cross-correlated our NIFS spectra. The inclusion of the extra regions finally enabled us to find the expected sinusoidal motion of the secondary star and the resulting radial velocity curve can be seen in Figure 5.2. The overlaid fit implied a $\gamma = 5 \pm 6 \text{ km s}^{-1}$ and $K_2 = 118 \pm 11 \text{ km s}^{-1}$. While these values differ from those of Steeghs et al. (2013) ($\gamma = 11 \pm 4.5 \text{ km s}^{-1}$ and $K_2 = 126 \pm 1 \text{ km s}^{-1}$) they are consistent within our errors which are larger

due to the higher resolution of the X-shooter spectrograph and the better sampling of their dataset.

The 2010 NIFS spectra are omitted from the analysis as despite the many data reductions and using the extra regions of the mask provided by Steeghs et al. (2013), we were still unable to achieve the expected velocities for the three 2010 spectra (see Figure 5.2). In their analysis of the same spectra Hurley et al. (2013) were also unable to find the expected radial velocity variation. We checked too that the telescope was on the correct target, as well as checking SIMBAD to ensure there was no other source nearby, which there is not. Given how well the features match those

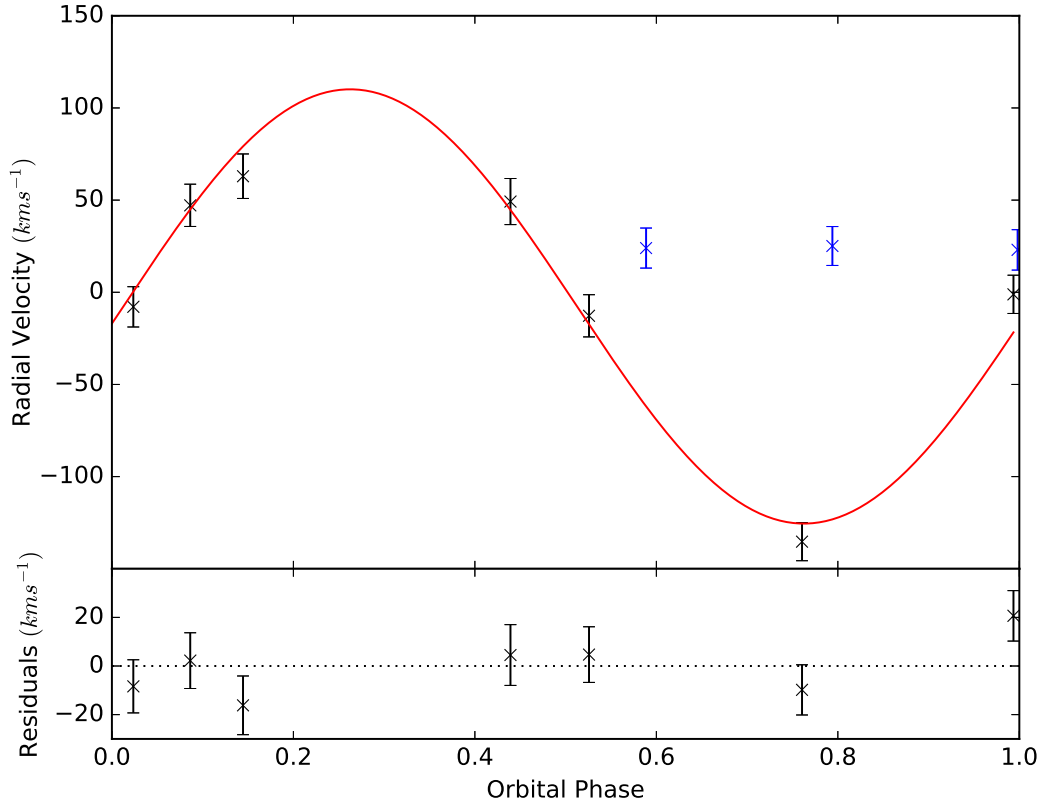


Figure 5.2: The radial velocity curve of GRS1915 found from the 2013 H-band NIFS spectra. The error bars have been enlarged to achieve a reduced $\chi^2 = 1$. The 2010 points (in blue) are plotted to show the lack of radial velocity variation.

of the template star, and the fact that the two spectra from 2013 which show only absorption lines produce the expected radial velocity variations, it is strange that the 2010 spectra do not.

VLT X-shooter Data

Steehgs et al. (2013) made available to us the following data: continuous, flux-calibrated JHK spectra of GRS1915, telluric standards for each night and the velocity template stars they observed; the H- and K-band masks used for their cross-correlations; and the averaged, template-subtracted H- and K-band spectra of GRS1915 in the rest frame of the secondary.

Initially the target, template and telluric spectra were written to ASCII files,

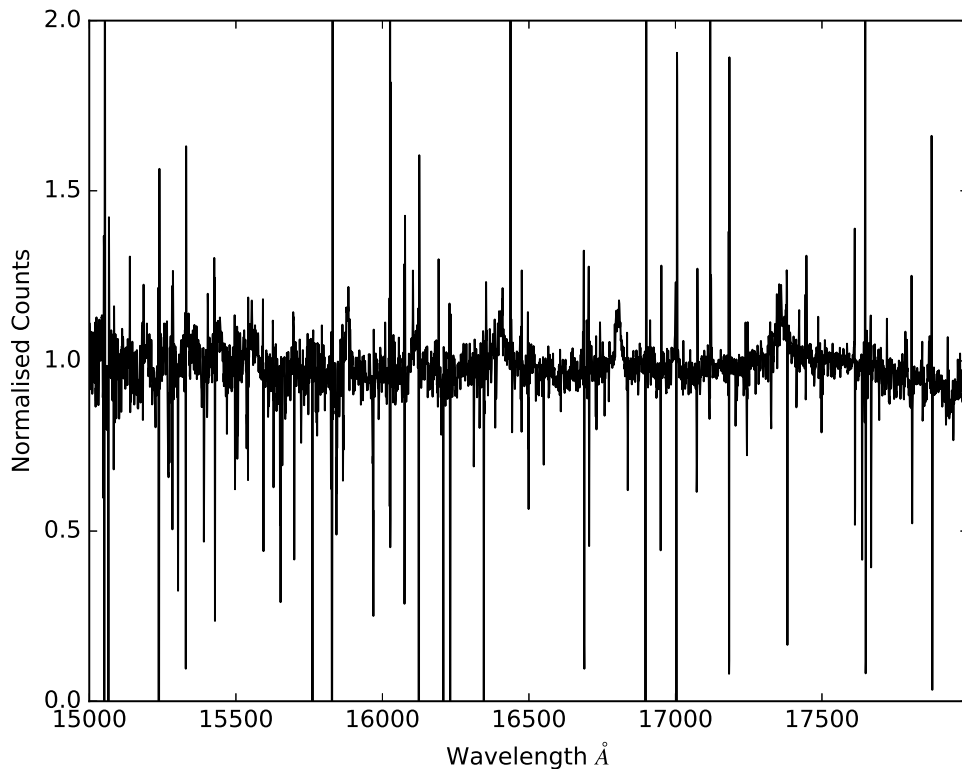


Figure 5.3: A typical VLT spectrum of GRS1915 before we applied the telluric and bad pixel corrections.

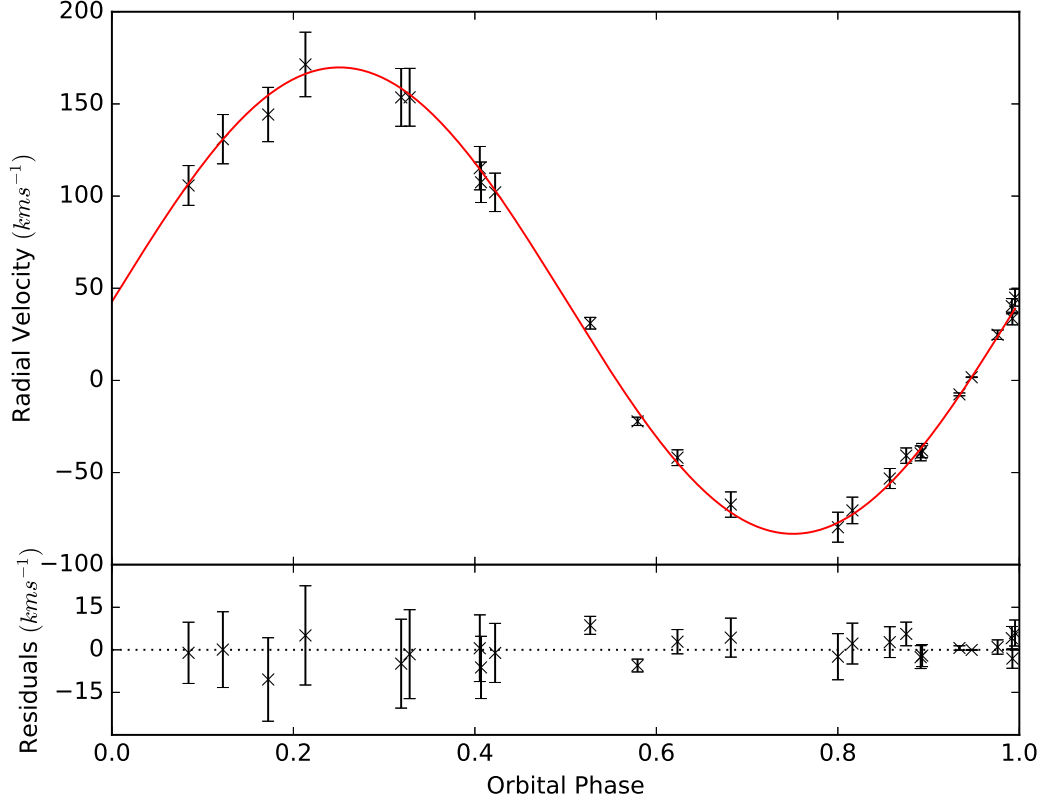


Figure 5.4: The radial velocity curve of GRS1915 found from the H-band VLT spectra listed in Table 5.2. The error bars have been enlarged to achieve a reduced $\chi^2 = 1$.

separated into individual J-, H- and K-bands and imported into IRAF where the continuum was normalised to one. At this point an inspection of the data revealed regions of poor telluric correction, particularly in the K-band, and extensive bad pixel regions in the H-band (see Figure 5.3). To remove the telluric lines present we divided each target spectrum by its corresponding telluric spectrum and then wrote a script to linearly interpolate over the bad pixel regions to aid with cross correlation. The spectra were then exported into MOLLY where the continuum was normalised to zero and the spectra were binned onto a common velocity scale. At this point the H-band spectra of GRS1915 were cross-correlated, using the same mask as for the NIFS spectra, against the same K5III template spectrum (HD 180732) used to produce Figure 2 of Steeghs et al. (2013). The resulting radial velocity curve can

be seen in Figure 5.2. The fit overlaid gives a semi-amplitude, $K_2 = 126 \pm 3 \text{ km s}^{-1}$. As stated in Steeghs et al. (2013) only one of the templates they observed has a published radial velocity (HD179130; $\gamma = 38 \pm 4 \text{ km s}^{-1}$) which allows us to estimate the velocity of GRS1915 to be $\gamma = 12 \pm 6 \text{ km s}^{-1}$. These values are consistent with those of Steeghs et al. (2013) ($K_2 = 126 \pm 1 \text{ km s}^{-1}$, $\gamma = 11 \pm 4.5 \text{ km s}^{-1}$), the larger errors on our values being due to the telluric and bad pixel corrections, as well as having used a slightly different mask for the cross-correlations.

5.3.1 Veiling Measurement

Once the system parameters (γ and K_2) were found from the fit to the radial velocity curve, the VLT spectra had their orbital motion removed and were averaged together to create a single high S/N spectrum. We used the OPTSUB routine in MOLLY which optimally subtracts the rotationally broadened template spectrum from the averaged spectrum of GRS1915 in order to estimate the contribution of the secondary star to the total light of the system. This works by subtracting constants times one set of spectra from another set and adjusting the constants so as to minimise the χ^2 of the residual spectrum. In estimating the secondary contribution we focused on two wavelength regions, namely $15920 \text{ \AA} - 16080 \text{ \AA}$ and $16530 \text{ \AA} - 16730 \text{ \AA}$, which contained absorption lines unaffected by both the bad pixel correction and telluric contamination. The fractional contribution of the secondary star in these two regions can be seen in Table 5.3 while the residuals can be seen in Figure 5.5.

The main sources of error in determining the contribution of the secondary star are ensuring the template used is of the correct spectral type and the accuracy of the normalisation of both the target and template spectra. In order to determine the spectral type we repeated the optimum subtraction process using the other template

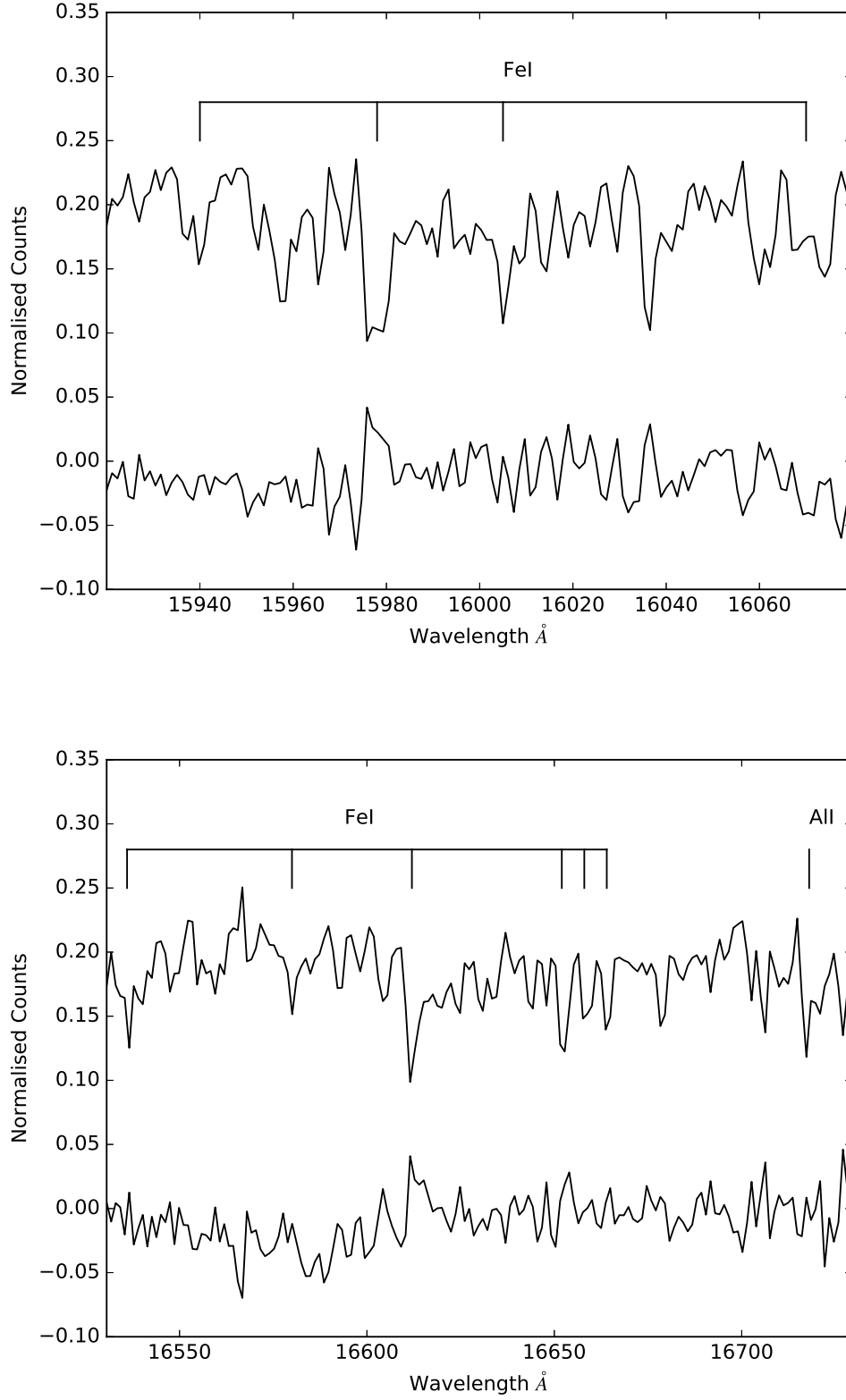


Figure 5.5: Comparison between the residual spectrum of the two wavelength regions considered in the average GRS1915 spectrum (bottom spectrum in each panel) after the scaled template spectrum (top spectrum in each panel) was subtracted. Some of the strongest absorption lines have been labelled.

Region	Secondary Contribution
15920 Å - 16080 Å	0.37 ± 0.02
16530 Å - 16730 Å	0.35 ± 0.02

Table 5.3: Fractional contribution of the secondary star to the total light of the system for the two regions of interest.

spectra Steeghs et al. (2013) observed (K0III, K1III and K2III stars). The K5III template resulted in the lowest χ^2 and was therefore chosen as the best spectral type match. We also investigated the normalisation of the two regions of interest in both the target and template spectra and found this made no significant improvement to the errors quoted in Table 5.3.

Steeghs et al. (2013) estimated the contribution of the secondary star to be approximately 25% across both the H- and K-bands, but provided no estimate of the error due to source variability from one epoch of observation to the next. We were restricted to looking at a small wavelength region of the spectrum due to the removal of a significant number of bad pixels. It is possible, therefore, that had we been able to utilise a larger wavelength region, our estimate of the secondary contribution would have been closer to the value found by Steeghs et al. (2013). However, as previously stated, given the source variability from one epoch to another, this may be able to explain the difference between our values quoted in Table 5.3 and that of Steeghs et al. (2013). We also attempted to see how the veiling varied with orbital phase but were prevented from doing so as the S/N was too low.

Epoch	Time of Minimum Light	Error (days)	Number of Orbits
Greiner	2451666.53898	0.25	-112
Hurley	2452478.93372	0.23	-88
Steeghs	2455458.68	0.06	0
NIFS	2456474.64682	0.3	30

Table 5.4: Results of the fits to each radial velocity curve for the four epochs of observation. Also shown is the number of orbits that have occurred between the reference epoch of Steeghs et al. (2013) and the remaining three epochs.

5.3.2 Refining the Ephemeris

Along with our own NIFS observations and those of Steeghs et al. (2013), we had available to us the data of Hurley et al. (2013) who reanalysed the data present by Greiner et al. (2001a,b) as well as presenting previously unpublished archival VLT data. These four epochs, stretching over approximately 14 years allowed us to refine the binary orbital ephemeris of GRS1915.

In order to accomplish this we first had to estimate the time of minimum light (ToML) for each epoch, defined here as the inferior conjunction of the secondary star. This was found from a sinusoidal fit to each of the four radial velocity curves of the form:

$$ToML = \gamma + \left(K_2 \sin \frac{2\pi(HJD - T_0)}{P_{orb}} \right) \quad (5.1)$$

where the semi-amplitude, K_2 , and the orbital period, P_{orb} , were fixed on the values found by Steeghs et al. (2013) (126 km s^{-1} and 33.85 days respectively). The results are shown in Table 5.4.

As the ephemeris of Steeghs et al. (2013) had hitherto been the most accurate,

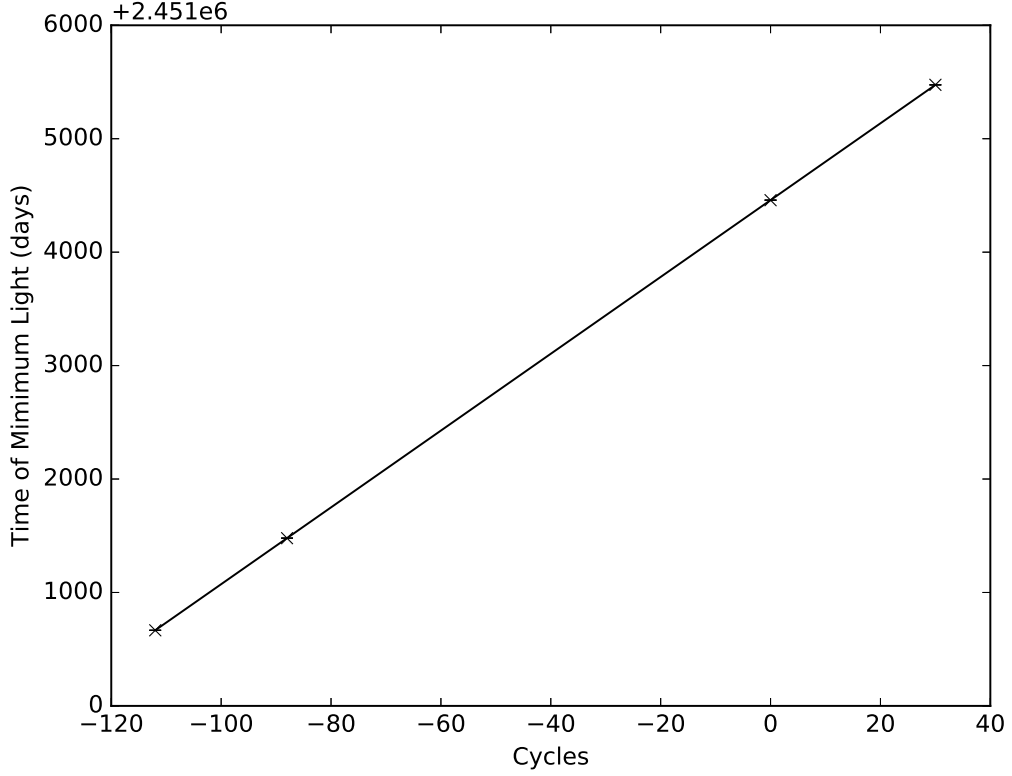


Figure 5.6: The straight line fit to the results shown in Table 5.4. The error bars are smaller than the size of the data points.

this was used to ensure there was no loss of cycle count from the epoch of the Greiner et al. (2001a) observations to the epoch of our NIFS observations. A straight line fit to the ToML versus the number of orbits, which can be seen in Figure 5.6, leads to a revised binary orbital ephemeris of:

$$T_0(\text{HJD(UTC)}) = (2455458.69 \pm 0.04) + (33.86 \pm 0.01)E$$

Given the large error bars on the O-C residuals (Figure 5.7) we performed a χ^2 test to determine if they were consistent with a (expected) parabolic fit, or a straight line. The resulting reduced χ^2 values were 0.737 and 1.54 respectively, implying that a parabola fits the data better statistically. Thus we expect the O-C residuals can

be fit by a parabola of the form:

$$O - C = aE^2 + bE + c \quad (5.2)$$

From this we can estimate the orbital period variation, \dot{P} , of GRS1915. This is found from the co-efficient of E^2 in Equation 5.2 (Sterken, 2005):

$$\frac{dP}{dt} = \dot{P} = \frac{2a}{\bar{P}} \quad (5.3)$$

where \bar{P} is the average orbital period, which we take to be that of the refined orbital period, i.e. $\bar{P} = 33.86$ days.

To constrain \dot{P} at the 68% confidence level we again performed a χ^2 test on the residuals. Given the one degree of freedom (four O-C residual data points minus the three free parameters of the parabolic fit) we require an increase in the χ^2 of

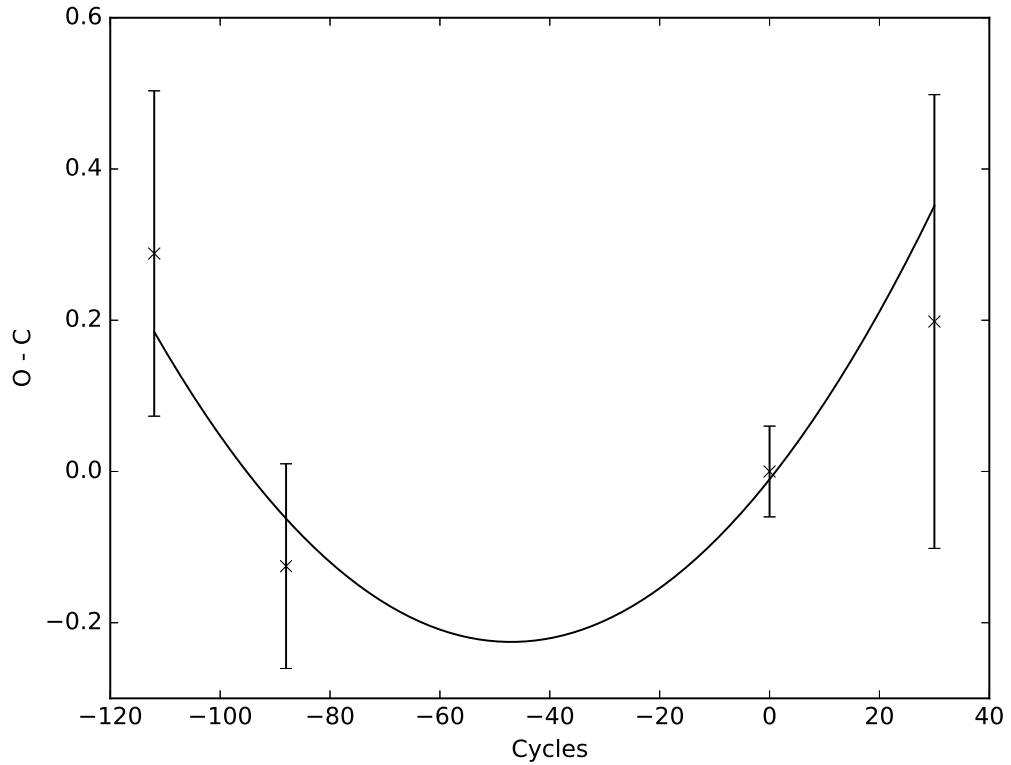


Figure 5.7: O - C residuals using our refined ephemeris.

the fit to the residuals of 1.704 (i.e the actual value of χ^2 required is $0.737 + 1.704 = 2.441$). We confined a , the co-efficient of E^2 , to lie in the range -2×10^{-4} to 2×10^{-4} and recalculated the fit in steps of 1×10^{-8} . At each step the corresponding value of χ^2 was found and the value of a at $\chi^2 = 2.441$ was put into Equation 5.3 and the orbital period variation, \dot{P} , of GRS1915 was estimated to be $\dot{P} = 5.74^{+4.86}_{-4.895} \times 10^{-6}$ days per day.

If we assume conservative mass transfer of the form (Pringle and Wade, 1985):

$$\frac{\dot{P}}{P} = -\frac{2\dot{M}_2}{M_1 + M_2} \quad (5.4)$$

this gives an estimate of the mass loss rate of the secondary star (again at the 68% confidence limit) of $\dot{M}_2 = 3.27^{+2.789}_{-2.77} \times 10^{-4} M_\odot \text{ yr}^{-1}$. This compares to an orbital period variation of $\dot{P} \sim 5 \times 10^{-9}$ days per day implied from a mass accretion rate of $\dot{M} \sim 3 \times 10^{-7} M_\odot \text{ yr}^{-1}$ from the modelling of Podsiadlowski et al. (2003). This is explained in more detail in the next section, however there are several reasons which may account for the discrepancy. Firstly we have only four data points from which to estimate \dot{P} and \dot{M}_2 . Indeed additional observations in the future will improve this ephemeris, and allow us to place more stringent limits on \dot{P} . For example, we have added two additional points to our O-C diagram, spaced five and 10 years after the last of the observations in Figure 5.7, and refitting the data shows that we would be able to constrain \dot{P} to within $\sim 5 \times 10^{-7}$ days per day. At this point we begin to place useful limits on the degree to which the mass transfer in GRS1915 is conservative or not. We also note the relatively large error on our estimate of \dot{P} . Secondly, the only system parameters available to Podsiadlowski et al. (2003) with which to compare their model were those of Greiner et al. (2001b), while they also froze the initial mass of the black hole at $10 M_\odot$, only varying the initial mass of the donor star. Given new, more accurate, estimates put the mass of the black hole

to be $\sim 10 M_{\odot}$ (i.e. the same value as their *initial* black hole mass) it seems obvious their model would need to take this into account. A model with lower initial black hole masses or varying black hole masses may provide a more robust description of the evolution of GRS1915.

In the Context of GRS1915

Podsiadlowski et al. (2003) specifically ran models aimed at reproducing the observational properties of GRS1915, i.e. models with an orbital period of 33.5 days (as determined by Greiner et al., 2001b). They find that if accretion was Eddington-limited the black hole in GRS1915 may have accreted up to $\sim 4 M_{\odot}$ since its formation. If, generally, the present mass of a black hole in a binary system is not an indicator of the initial remnant mass, then any analyses of such systems (e.g. Bailyn et al., 1998, Özel et al., 2010 and Farr et al., 2011) must take this into account. The possible $\sim 4 M_{\odot}$ of accreted material suggests the black hole has been spun up to a spin parameter of $a \sim 0.8$. This assumption is conservative as the initial spin of the black hole will depend on the final spin of the progenitor. As such the estimate here may be consistent with the estimate of $a \sim 0.97$ as stated by Narayan and McClintock (2012). Mass transfer rates of up to $\dot{M} \sim 3 \times 10^{-7} M_{\odot} \text{yr}^{-1}$ imply an X-ray luminosity $L_x \sim 2 \times 10^{39} \text{ erg s}^{-1}$, only slightly lower than the peak luminosity achieved by GRS1915 ($L_x \sim 7 \times 10^{39} \text{ erg s}^{-1}$), and so they suggest only moderate super-Eddington accretion would be required in their model to account for the observed L_x .

5.3.3 K-band Analysis

In their paper, Hurley et al. (2013) saw phase-dependent emission of the CO band heads in the K-band: emission was present in the first half of the orbit but not the second half (see their Figure 5). We searched the K-band of Steeghs et al. (2013) to see if this phase-dependence was also present in their VLT spectra and the trailed spectra can be seen in Figure 5.9. It would appear there is some weak emission blueward of the absorption line in the first half of the orbit and that this disappears in the second half of the orbit as the absorption line becomes stronger. Any emission that is present, however, is too weak to see in the individual spectra, but when averaged we see the same narrow emission feature at $\sim 23200 \text{ \AA}$ (see Figure 5.8) as in Figure 3 of Steeghs et al. (2013).

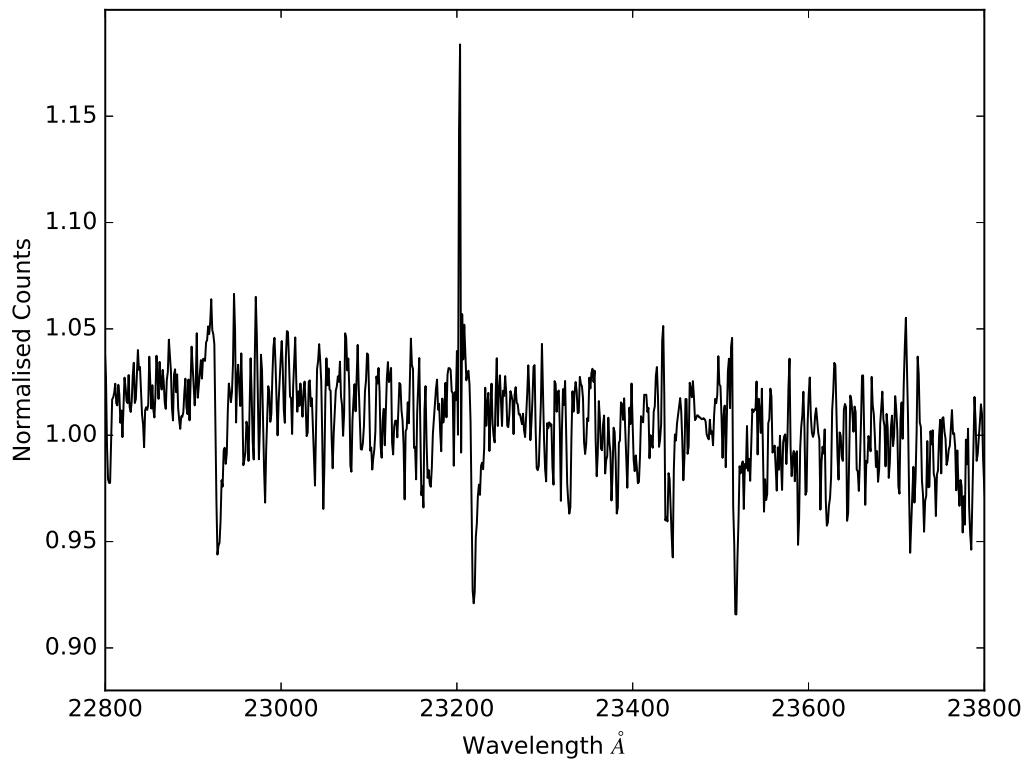


Figure 5.8: Average VLT K-band spectrum of GRS1915.

The cause of this emission is not immediately obvious. It may be due to the presence of P Cygni lines originating from a wind in the system, or, as noted by Hurley et al. (2013), CO band head emission has a dissociation energy of 11.1 eV and so the location of the emission must be in the outer part of the accretion disc. A warped, precessing accretion disc could provide the required shielding from X-rays in this region to achieve the low dissociation energy.

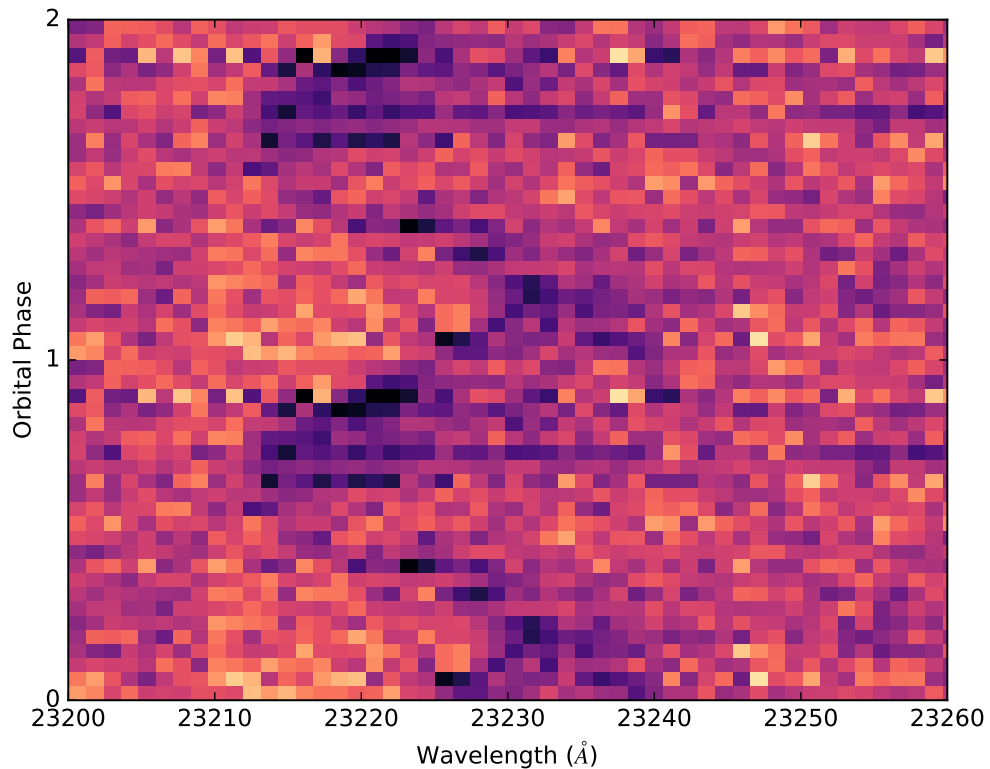


Figure 5.9: K-band trail of the VLT spectra showing emission blue-ward of the absorption line in the first half of the orbit. In the second half the absorption line becomes stronger and the emission disappears. Data have been repeated for clarity.

5.3.4 Emission Line Study

The variation of the absorption lines due to the motion of the secondary star can be seen in Figure 5.10. The lack of radial velocity variation of the emission line is to

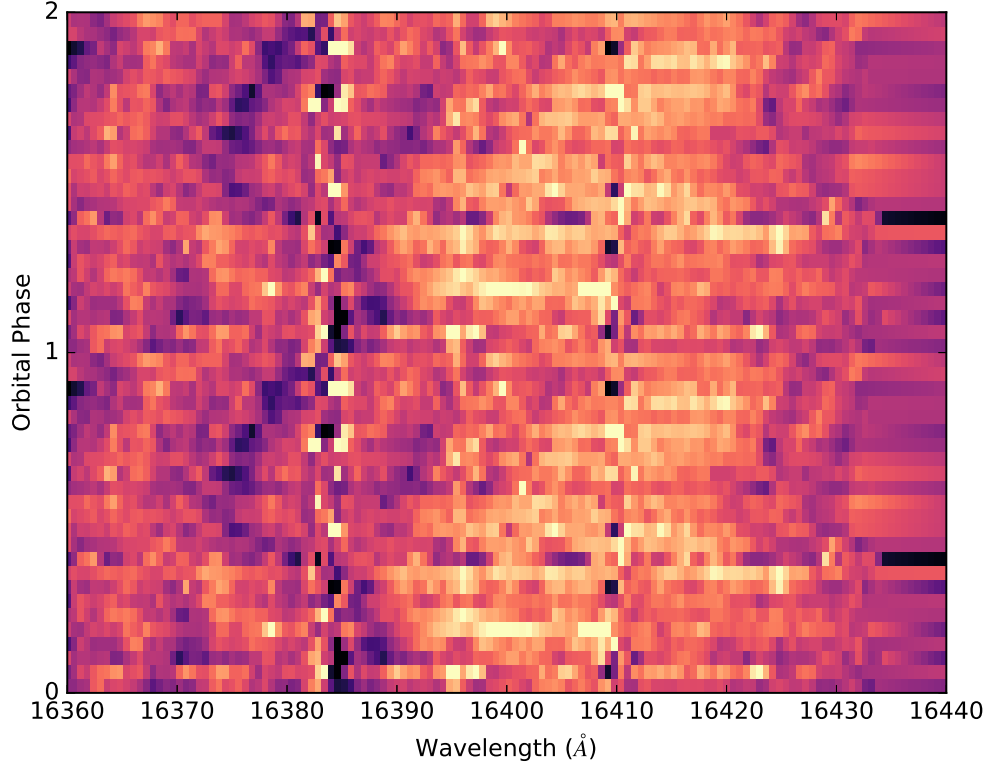


Figure 5.10: Typical H-band trail of the VLT spectra showing the S-wave pattern of the absorption lines of the secondary star as well as the emission line centred on 16411.7 Å. Data have been repeated for clarity.

be expected as the semi-amplitude and mass ratio ($K_2 \sim 126$ and $q \sim 0.042$) imply a $K_1 \sim 5 \text{ km s}^{-1}$, much less than the resolution of the data ($\sim 22 \text{ km s}^{-1} \text{ pix}^{-1}$).

Figure 5.10 does, however, suggest the emission line strength varies across the orbit. Belloni et al. (2000) defined 12 variability classes based on count rate and colour-colour diagrams from RXTE data. From this they suggest the variability observed in GRS1915 is due to transitions between three states: two soft states representing different disc temperatures and accretion rates and a hard state due to obscuration of the inner disc.

In order to determine whether there was a correlation between the EWs of the $\text{Br}\gamma$ emission lines and the X-ray variability of GRS1915 we obtained the Monitor

of All-sky X-ray Image (MAXI, see Matsuoka et al., 2008) 2-20 keV counts as close in time to the VLT observations as possible, but found no strong correlation (see Figure 5.11) and hence we conclude that the emission line strength is not strongly related to the X-ray luminosity. Ideally we would have performed this analysis on the HeI line (see Figure 5.12), which originates closer to the Black Hole than the Br γ given the larger energy required to ionise Helium, however it was too weak to see in the individual spectra, only becoming apparent in the averaged spectrum while also being heavily affected by the bad pixel correction.

Given an orbital period of $P_{orb} = 33.5$ days, Truss and Wynn (2004) estimate the radius of the accretion disc in GRS1915 to be $R_d \sim 3 \times 10^{12}$ cm. The Keplerian

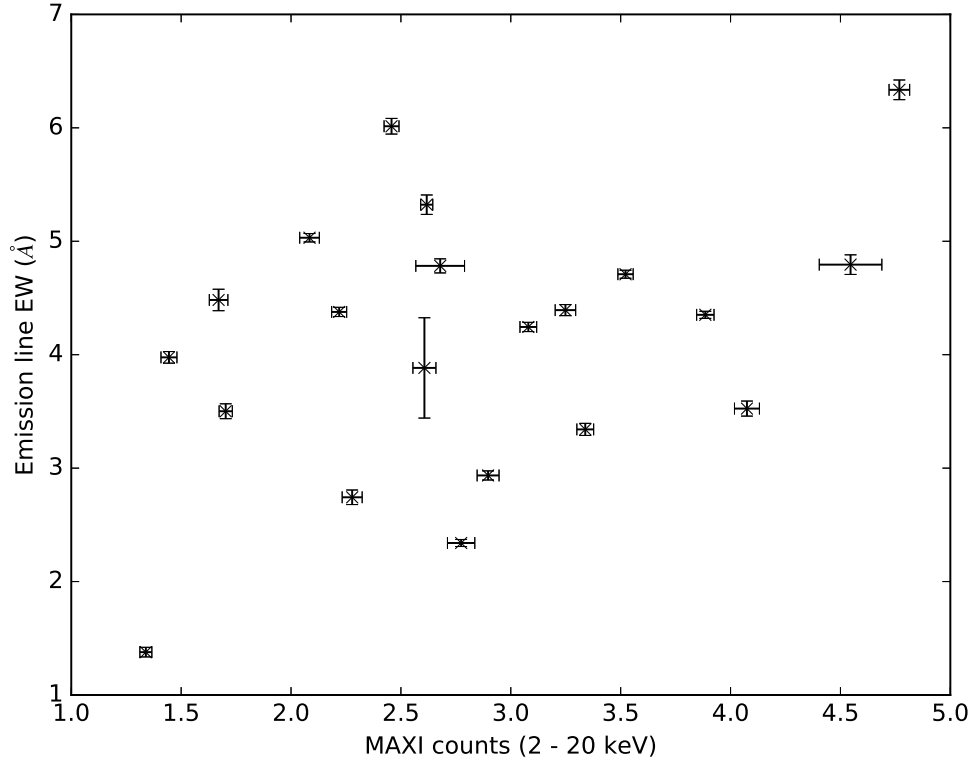


Figure 5.11: Emission line (16411.7 Å) EW versus the MAXI counts for the VLT spectra. It is clear there is no strong correlation.

velocity at the outer disc radius can be estimated from the following equation, and compared to the peak to peak separation of double peaked emission lines:

$$V_{kep} = \left(\frac{GM_{BH}}{r} \right)^{1/2} \sin i \quad (5.5)$$

where $i = 60^\circ$ and $M_{BH} = 12.4^{+2.0}_{-1.8} M_\odot$ (both from Reid et al., 2014). We measured the peak to peak line separation for all the $\text{Br}\gamma$ emission lines in our averaged NIFS spectrum (ranging from 6.45 Å to 9.45 Å) and take the average of these as an estimate of the radius of the accretion disc in GRS1915 to be $R_d \sim 5.7 \times 10^{12}$ cm. For the average VLT spectrum we were only able to use two emission lines (15884.9 Å and 16411.7 Å) as they were the only two unaffected by the bad pixel correction. We used the FWHM, rather than the peak to peak line separation, to estimate the radius of the accretion disc as the emission lines did not appear double peaked and found the radius of the disc to be in the range $R_d \sim 2.5 - 2.6 \times 10^{12}$ cm. Given the better signal to noise, and the fact there are more individual spectra averaged together, it is likely the VLT estimate is more robust, and it is in agreement with the estimate of Truss and Wynn (2004).

Both the NIFS and VLT spectra suggest the origin of the $\text{Br}\gamma$ emission is the outer part of the accretion disc. It is likely this is where the X-ray irradiation is lowest and may help to explain why we see no strong correlation between the emission line equivalent widths and the MAXI X-ray counts.

Asymmetric Emission Lines

Asymmetric emission lines in GRS1915 have been reported before, notably by Martí et al. (2000). However, they ascribe the asymmetry to the evolution of a P-Cygni profile from absorption to emission. They also report a possible P-Cygni profile in one of the spectra of Mirabel et al. (1997). In the case of both the VLT and NIFS

averaged spectra (see Figure 5.12) we see no evidence of any P-Cygni profiles but do see a change in the emission line profiles: the average VLT spectrum shows a pronounced blue emission peak in most of the Br γ lines, while the average NIFS spectrum has more pronounced red emission peaks. Initially we thought that as all but one of the NIFS spectra cover the first half of the orbit, this may give rise to the red wing of the emission lines being more pronounced. Therefore we averaged all the VLT spectra between phases $\phi = 0 - 0.5$ to see if this resulted in a similar effect, which it did not. Hence we conclude that the asymmetry seen in the emission lines is real, and not an artefact of our sampling.

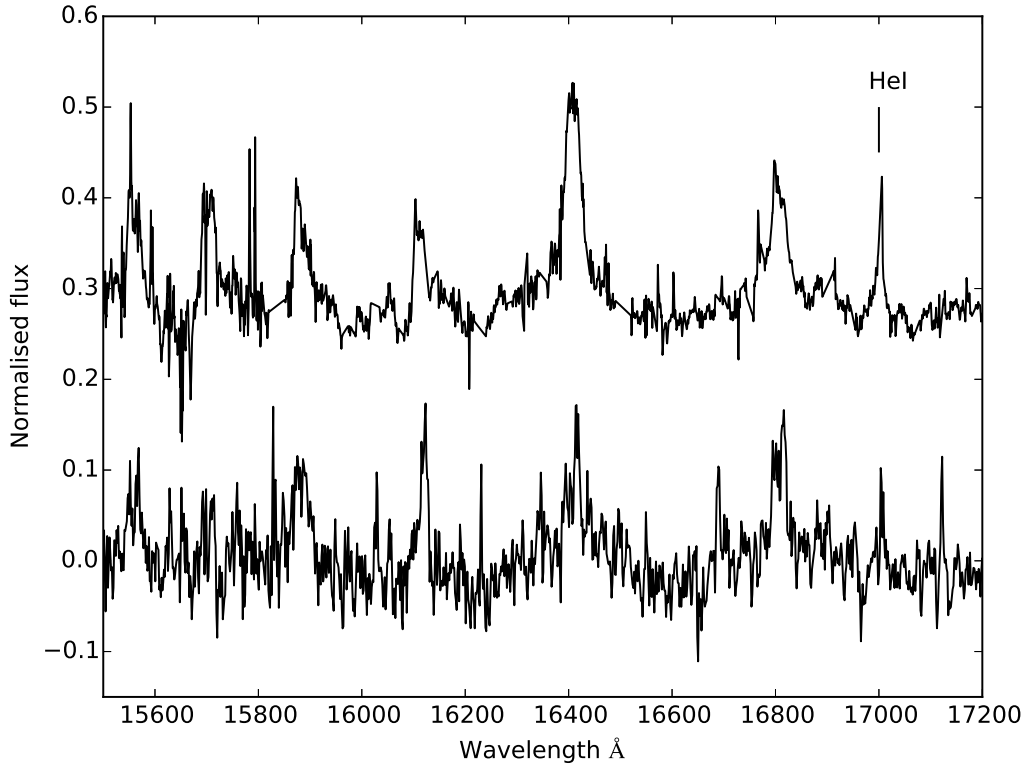


Figure 5.12: The averaged H-band spectra of GRS1915 using the VLT spectra (top) and NIFS (bottom). The spectra have not been shifted to the rest frame of the donor in order to show the emission lines.

Asymmetric emission lines may also be indicative of a warped, precessing accretion disc, evidence of which manifests as a super-orbital period. Many X-ray binaries (both low- and high-mass) have been found to exhibit such super-orbital period variations. Indeed, Rau et al. (2003) identified a 590-day long term periodicity in the hard X-ray component of GRS1915 from analysis of four years of RXTE spectra. The periodicity was also present in the hard X-rays observed with BATSE (the Burst and Transient Source Experiment on board the Compton Gamma Ray Observatory, see Horack, 1991), as well as in the radio flux from the Green Bank Interferometer and the Ryle Telescope. If radiation absorbed in the outer, tilted region of the disc is re-emitted parallel to the local disc gradient a torque is induced due to the gas pressure exerted on the disc. A possible argument against a warped, precessing disc in GRS1915 is given by Rau et al. (2003): in all other systems believed to harbour such a disc, it was the soft X-rays that displayed the super-orbital periodicity. As such it remains unclear as to whether GRS1915 harbours a warped, precessing disc, however such a disc could reasonably be expected to obscure the secondary star and so a search for a super-orbital periodicity in the IR flux of the secondary star would help to constrain the source of the 590 day period.

Further evidence of a precessing accretion disc in GRS1915 was presented by Neil et al. (2007) who found evidence of a superhump period in their analysis of seven years of K-band photometry. They split their data into two subsets, rising and falling, based on how the magnitude varied over three adjacent data points (i.e. rising denotes the local magnitude increasing over the three points). Analysis of the frequency spectrum implied a period in the range 31.2 to 31.6 days. Interestingly, they estimated the orbital period of the secondary to be $P_{orb} = 30.8 \pm 0.2$ days, which at the time was consistent with that of Greiner et al. (2001b), and implied

that as the superhump period was larger than the orbital period, the superhump precession was prograde with respect to the rotation of the accretion disc. However, given our revised orbital period of $P_{orb} = 33.86 \pm 0.01$ days, it would suggest that this is not the case.

Some caution should be taken when dealing with long term photometric analysis of GRS1915 however. As mentioned earlier, Belloni et al. (2000) defined 12 variability classes due to transitions between three states and as such a more robust treatment of photometry over long time scales may be required. It may also be that the shape of the emission lines in the IR spectra of GRS1915 are linked to the type of variability at a given time. More high S/N spectra, as well as simultaneous photometry, would be required to study this in detail.

5.4 Similar Systems

A literature search for IR spectra was undertaken of other high mass, long period LMXB systems to see if they displayed similar characteristics to GRS1915. Namely the presence of asymmetric emission lines which can not only vary dramatically in strength, but disappear entirely. However, it is due to the large black hole mass and long orbital period, and by extension large accretion disc, that makes it difficult to find objects of comparison.

The next longest period LMXB system is Cygnus X-2 (Cyg X-2) with an orbital period of ~ 9.8 days (Casares et al., 1998) containing a neutron star, rather than a black hole. Cyg X-2 is one of the brightest LMXB sources and is rare among such objects in that the secondary is easily detectable. The high optical extinction to GRS1915 necessitates the use of IR spectra, but as Cyg X-2 is so bright in the optical, unfortunately a search of the literature failed to return any IR spectra of

the object.

The next longest period microquasar is V404 Cyg with an orbital period of $P_{orb} \sim 6.5$ days (Casares and Charles, 1994). As pointed out by Steeghs et al. (2013) this means the volume of the Roche lobe of the black hole in V404 Cyg is 50 times smaller than for GRS1915 and so a much smaller accretion disc can form. After discovery in 1989 V404 Cyg achieved a peak visual magnitude of $V = 11.6$ and returned to a quiescent magnitude of $V = 18.0$ within one year (Khargharia et al., 2010 and the references within). The first IR study was carried out by Shahbaz et al. (1994) who modelled the K-band light curve as the ellipsoidal variation of the secondary star, providing an estimate of the black hole mass of $M_{BH} \sim 12 M_{\odot}$. Sanwal et al. (1996) obtained H-band photometry and found evidence of distortions to their light curve from some source other than the secondary star, namely the accretion disc. Shahbaz et al. (1994) had assumed the only source of light was the secondary star while the H-band light curve clearly showed an unknown veiling by the disc. Therefore, Sanwal et al. (1996) were only able to provide an upper limit to the mass of the black hole of $M_{BH} < 12.5 M_{\odot}$. They did, however, reanalyse the K-band data of Shahbaz et al. (1994) and were able to show it, too, was contaminated by an unknown amount of light from the accretion disc. As a result of this, Shahbaz et al. (1996) obtained, for the first time, a K-band spectrum of V404 Cyg. They showed the maximum amount of light from the accretion disc to be 14% at the 95% confidence level, which in turn revised the upper limit to the mass of the black hole to be $M_{BH} < 10 M_{\odot}$. Finally, Khargharia et al. (2010) analysed NIR broadband spectra, estimating the H- and K-band secondary star contributions to be 0.98 ± 0.05 and 0.97 ± 0.09 respectively. They then remodelled the H-band light curve of Sanwal et al. (1996), correcting for the veiling, and determined the inclination to

the system. This, ultimately, lead to an estimate of the mass of the black hole to be $M_{BH} = 9^{+0.2}_{-0.6} M_{\odot}$.

On 15 June 2015 V404 Cyg went into outburst for the first time since 1989. Multiwavelength observations showed variations right across the spectrum (Plotkin et al., 2016). Once again, however, there is a general dearth of IR observations during the outburst period.

Cyg X-2 and V404 Cyg provide the two longest orbital period LMXBs. If we extend our search to include binary systems more generally, with the caveat that an accretion disc must be present, we arrive at SS433. Originally identified as one of many objects to display strong H α emission, it was soon shown to be the source of coincident radio and X-ray emission. SS433 is, like, Cyg X-2 and V404 Cyg, bright, and it was from optical spectra that the peculiar nature of this object became clear. Broad emission lines at unexpected optical wavelengths were later shown to be Doppler shifted Balmer and HeI lines. The maximum red- and blue-shift of these lines has been measured at 50,000 km s⁻¹ and 30,000 km s⁻¹ respectively. We now know these are due to the outflow from a bipolar jet, which has a ~ 163 day periodicity. See Margon, 1984 and Fabrika, 2006 for a review. Hillwig and Gies (2008) found evidence of absorption lines from the secondary which they suggest is an A3-7I type star in an orbital period of $P_{orb} = 13$ days. Their analysis yielded mass estimated of $M_{BH} = 4.3 M_{\odot} \pm 0.8 M_{\odot}$ and $M_S = 12.3 M_{\odot} \pm 3.3 M_{\odot}$ for the black hole and secondary star respectively.

The gravitational distortion on the outermost part of the accretion disc by the secondary star changes the inclination of this part of the disc, which has been observed as a 0.2 magnitude change in the optical light curve. Fabrika (2006) state that material passes through the accretion disc in less than three days, driving the

super-Eddington accretion.

What is clear from our search of systems comparable to GRS1915 is that there is an extreme lack of infrared observations. As light from the secondary star in LMXBs begins to dominate in the infrared region of the spectrum, IR observations are ideal in identifying the spectral lines of the secondary stars, which in turn allows dynamical studies and estimates of the masses of the binary components. It is clear that more IR observations of LMXBs are needed to better our understanding of these systems.

Chapter 6

Conclusions and Future Work

In this thesis, we have presented optical and infrared observations of a number of interacting LMXB systems: one with a neutron star primary and two with black hole primaries. Radial velocity studies were undertaken to refine the binary parameters and a proof of concept to estimate the changing contribution of the accretion disc was attempted. Here we summarise the various results and discuss some opportunities for future work.

Conclusions

PSR1023+0038

The history of J1023 tells us the system undergoes transient accretion phases. In outburst we see double peaked emission lines and when in quiescence millisecond radio pulsations are detected. This suggests the system occupies an important position on the evolutionary track from LMXB to isolated millisecond radio pulsar.

We have presented archival WHT optical spectra and combined this with the V-band spectroscopy of Thorstensen and Armstrong (2005). Using ELC to simultaneously fit the light curve with our new radial velocity curve we constrain the upper

limit of the mass of the pulsar to be $\leq 2.2 M_{\odot}$ at the 2σ level, and have shown that the secondary star is underfilling its Roche lobe by 15% to 20% at the 1σ level. This suggests the idea that the method of mass transfer is via a wind on the secondary rather than the more common method of Roche lobe overflow which is usually the case in LMXBs. This may be due to the transient accreting/non-accreting history of the system.

Optimum subtraction of the template spectrum from the average spectrum of the secondary star revealed residual $H\alpha$ emission. Repetition of this subtraction on the 26 individual spectra of J1023, and measurement of the semi-amplitude of the emission, suggests it is consistent with the absorption line semi-amplitude velocity. As such we suggest that the residual $H\alpha$ emission is either due to the irradiated inner hemisphere of the secondary, or that the secondary is a chromospherically active star.

Finally, we presented new optical photometry obtained while J1023 was in outburst in 2014 taken on one night in April at the VATT and over two nights in June at the SAAO. We combined the latter with the V-band photometry of Halpern et al. (2013) also taken in June at Kitt Peak. The light curve of the April data showed fast (~ 15 s) and long (~ 100 s) flickering while by June the light curve shows a smooth, slightly asymmetric modulation with minimum at phase zero.

A0620-00

As A0620-00 has been in quiescence since 1976 it has allowed for extensive study of the system. The donor has been identified as a K-type star accreting material onto a black hole whose mass has been precisely determined as $M = 6.6 \pm 0.25 M_{\odot}$. Its distance of $d = 1.06 \pm 0.12$ kpc makes it one of the closest known black hole

systems.

However, the previous assumption of many authors that the contribution of the accretion disc to the light curve is constant is clearly wrong with significant variation on time scales of days. As such, we presented simultaneous, phase resolved V-band spectroscopy and photometry with the intent of measuring the changing veiling at each phase of our observations. This was a proof of concept idea that would enable us to correct our light curve for the disc contribution on a time scale of our exposure time of four minutes and give us the pure ellipsoidal modulation due to the secondary star. However it became clear we did not have the S/N required in our spectroscopy to achieve this. Indeed the unscaled errors were on the order of 45%. Due to the corresponding increase in S/N required it seems unlikely that any existing telescope would be capable of achieving this. More likely these observations would only be possible with the new generation of extremely large telescopes such as the E-ELT which is expected to have its first light in the mid-2020s.

GRS1915+105

Many properties of GRS1915 make it unique. It has remained in outburst since it was discovered in the 1990s when we would typically expect a return to quiescence within a year. It has the longest known orbital period of 33.85 days and is often observed as the most luminous accreting black hole in the Galaxy. The near-maximum spin of the black hole gives rise to the parsec-scale jets which have seen GRS1915 dubbed the prototype galactic microquasar.

Much work on GRS1915 has focused on the molecular lines in the K-band. We presented H-band spectra in the hope that these intrinsically narrower, atomic absorption lines would help to better constrain the mass of the black hole. Three

“pathfinder” spectra were obtained in 2010 showing many of the absorption lines identified by Greiner et al. (2001a). As a result more spectra were obtained in 2013 covering more of the orbital phase. One of the seven spectra showed absorption lines while the remaining spectra displayed broad Br γ emission lines as well as some of the absorption lines identified by Greiner et al. (2001a).

Cross correlation of the absorption lines against a high resolution template spectrum did not reveal the expected radial velocity shifts. As such, we investigated the arc solution, any variation in the skylines from their rest wavelengths and the accuracy of the telluric correction. None of these were able to account for the lack of variation we saw. We contacted Steeghs et al. (2013) who provided us with their VLT observations. After first correcting these for telluric lines and bad pixels, we were able to repeat their dynamical study in the H-band, while also confirming the varying emission line strength in the K-band. Combining the VLT and NIFS observations with those of Greiner et al. (2001a) and Hurley et al. (2013), we were able to refine the ephemeris which should prove useful to other studies conducted in the future. Using the new ephemeris we estimated an upper limit, at the 68% confidence limit, on the spin down rate to be $\dot{P} = 5.74^{+4.86}_{-4.895} \times 10^{-6}$ days per day. Assuming angular momentum and mass loss are both conserved this gives an upper limit to the mass loss rate of the secondary to be $\dot{M}_2 = 3.27^{+2.789}_{-2.77} \times 10^{-4} M_{\odot} \text{ yr}^{-1}$. Including additional points at five and ten years after the observations on Figure 5.7 and refitting the data, shows that we would be able to constrain \dot{P} to within $\sim 5 \times 10^{-7}$ days per day. At this point we begin to place useful limits on the degree to which the mass transfer in GRS1915 is conservative or not.

Future Work

PSR1023+0038

Phase resolved spectroscopy and more accurate photometry while the system is in quiescence are required to confirm the underfilling of the Roche lobe, as well as to explain the origin of the residual H α emission. As our photometry of the system in outburst was taken over several epochs and only sampled part of the orbital phase, more systematic observations are required to investigate the short and long time scale flickering that we see. Given the important position of J1023 on the evolutionary tack (i.e. between LMXB and isolated millisecond pulsars), and the few comparable systems, more observations could prove vital for enhancing our understanding of these systems.

A0620-00

It appears to be a matter of waiting for the next generation of telescopes to come online before we will be able to achieve the high S/N spectra required to sample the veiling on such short time scales. Extending this concept to other wavelengths may also be useful.

More immediately it may be possible to use this method on other, brighter systems. For example there are many CVs several magnitudes brighter than the quiescent state of A0620-00 which may provide a good test of this proof of concept.

GRS1915+105

Further IR observations of GRS1915 would be useful in many ways. Higher signal-to-noise data may enable us to confirm the presence of a precessing accretion disc

and would aid in attempting to measure the veiling on shorter timescales. Continued study would also provide longer baseline measurements to refine the limit on \dot{P} while further photometric observations of GRS1915 would also prove useful to explain the difference in the photometric and spectroscopic periods of the system. Finally, given the multitude of different variability states present in GRS1915, more observations will help in our understanding the nature of this emission behaviour.

Appendix A

An Eclipsing Light Curve Code

In order to estimate and model the system parameters in Chapter 3 we utilised the Eclipsing Light Curve (ELC) of Orosz and H.Hauschildt (2000). Here we provide a brief overview of how the code works.

The Roche lobe filling factor, mass ratio and the rate of the secondary star's rotation define the shape of the star. The effective temperature, gravity darkening and linear limb darkening co-efficient define the temperature over the whole star. The Planck function and limb darkening are then used to compute the intensities over the whole star. Finally, when the orbital phase information and the inclination angle are added the total observed flux can be calculated.

ELC models any accretion disc as an optically thick, flattened cylinder centred on the compact object. It is assumed that the temperature does not vary with azimuth angle and, if sufficiently thick, light from the rim is also accounted for. Planck's function, once again, is used to relate temperature and intensity at a point on the disc.

If the inclination is sufficiently large enough, ELC is also capable of modelling eclipses. The integration of flux elements of the body in front is done as described

previously. All points on the edge (or horizon) of this body are projected onto the plane of the sky. The integration of the flux elements of the body being eclipsed are found and also projected onto the plane of the sky. If they lie within that of the body in front they are excluded from the model.

To account for X-ray heating the X-ray luminosity and physical size of the orbit are found using the mass function and orbital period. The net result is points on the star facing the irradiating source are brighter and their temperature is increased.

ELC computes grids of models and performs χ^2 fits to the data using a wide range of parameters uniformly spaced. The sets of parameters that produce low χ^2 are chosen and used as the starting point for an optimisation routine. After several runs of different starting points the parameter set giving the lowest overall χ^2 fit to the data is chosen. It is this use of many different starting points that helps to achieve a global, rather than local, minimum χ^2 .

Errors to the parameters are internal statistical errors, not systematic, and are found from bootstrapping. Artificial data are constructed from the original and the same fitting procedure is used on this data as was used on the original. The 1σ errors returned are derived from the distribution of the fitted parameters from the many artificial data sets.

Appendix B

The O-C Method

The O-C method was employed in Chapter 3 in order to refine the orbital period of the system.

Initially, the radial velocity curve was folded on the then best known orbital period of 0.198094 days, from Thorstensen and Armstrong (2005). The resulting systemic velocity, γ , and semi-amplitude, K_2 , were fixed at 1 km s^{-1} and 286 km s^{-1} respectively. The orbital period was then varied and the corresponding radial velocity value and χ^2 was found for each of our observations. The individual χ^2 were then summed and divided by the 25 degrees of freedom (the 26 radial velocity data points minus the one free parameter, the orbital period).

This process was repeated until a minimum reduced χ^2 was found, corresponding to a revised orbital period of 0.1980966 days.

Appendix C

List of Publications

Peer Reviewed Publications

“Roche lobe underfilling of the secondary star in PSR J102347.6+003841?”, O. McConnell; P. J. Callanan; M. Kennedy; D. Hurley; P. Garnavich; J. Menzies, Monthly Notices of the Royal Astronomical Society 2015 451 (4): 3468-3472

Oral Presentations

“The Mass of the Transiently Accreting Neutron Star FISTJ102347.6+003841” Astronomical Science Group of Ireland (ASGI) Summer Meeting, 7 June 2013, Trinity College Dublin, Ireland

Poster Presentations

“The Mass of the Transiently Accreting Neutron Star FIRSTJ102347.6+003841” IAU Symposium 290, 20 - 24 August 2012, Beijing, People’s Republic of China

“Gemini H-band Spectroscopy of the Galactic Microquasar GRS1915+105” The

X-ray Universe, 16 - 19 June 2014, Trinity College Dublin, Ireland

“Gemini H-band Spectroscopy of the Galactic Microquasar GRS1915+105” Irish National Astronomy Meeting (INAM), 13 - 15 August 2014, Trinity College Dublin, Ireland

“Optical Variability of PSR J1023+0038 During its Recent Outburst” INAM, 26 - 28 August 2015, Queen’s University Belfast

Bibliography

Al-Naimiy, H. M. (1978). *ApES*, 53:181–192.

Archibald, A. M., Kaspi, V. M., Bogdanov, S., Hessels, J. W. T., Stairs, I. H., Ransom, S. M., and McLaughlin, M. A. (2010). *ApJL*, 732:88.

Archibald, A. M., Stairs, I. H., Ransom, S. M., Kaspi, V. M., Kondratiev, V. I., Lorimer, D. R., McLaughlin, M. A., Hessels, J. B. J. W. T., Lynch, R., van Leeuwen, J., Roberts, M. S. E., Jenet, F., Champion, D. J., Rosen, R., Barlow, B. N., Dunlap, B. H., and Remillard, R. A. (2009). *Science*, 324:1411.

Backer, D. C., Kulkarni, S. R., Heiles, C., Davis, M. M., and Goss, W. M. (1982). *Nature*, 315(615B).

Bailyn, C. D., Jain, R. K., Coppi, P., and Orosz, J. A. (1998). *ApJ*, 499:367–374.

Balbus, S. A. and Hawley, J. F. (1991). *ApJ*, 376:214–222.

Bassa, C. G., Patruno, A., Hessels, J. W. T., Mahoney, E. F. K. B. M. E. K., Bogdanov, S., Corbel, S., Edwards, P. G., Archibald, A. M., Janssen, G. H., Stappers, B. W., and Tendulkar, S. (2014). *MNRAS*, 441:1825–1830.

Becker, R. H., White, R. L., and Helfand, D. J. (1994). *In: ASP Conference Series. Edited by D. R. Crabtree and R. J. Hanisch and J. Barnes.*

- Belloni, T., Klein-Wolt, M., Méndez, M., van der Klis, M., and van Paradijs, J. (2000). *A&A*, 355:271–290.
- Bevinton, P. R. and Robinson, D. K. (2003). *Data Reduction and Error Analysis for the Physical Sciences, Third Edition*.
- Bingham, R. (1984). *General Optical Description of the 4.2 m Herschel Telescope, RGO/La Palma Technical Note No. 9*.
- Bochanski, J. J., Hennawi, J. F., Simcoe, R. A., Prochaska, J. X., West, A. A., Burgasser, A. J., Burles, S. M., Bernstein, R. A., Williams, C. L., and Murphy, M. T. (2009a). *PASJ*, 121:1409.
- Bochanski, J. J., Hennawi, J. F., Simcoe, R. A., Prochaska, J. X., West, A. A., Burgasser, A. J., Burles, S. M., Bernstein, R. A., Williams, C. L., and Murphy, M. T. (2009b). *PASP*, 121:1409–1418.
- Bond, H. E., White, R. L., Becker, R. H., and O’Brien, M. S. (2002). *PASP*, 114:1359.
- Bowen, I. S. and Vaughan, A. H. (1973). *Applied Optics*, 12:1430.
- Brown, G. E., Weingartner, J. C., and Wijers, R. A. M. J. (1996). *ApJ*, 463:297–304.
- Cantrell, A. G., Bailyn, C. D., McClintock, J. E., and Orosz, J. A. (2008). *ApJ*, 637:L159–L162.
- Cantrell, A. G., Bailyn, C. D., Orosz, J. A., McClintock, J. E., Remillard, R. A., Froning, C. S., Neilsen, J., Gelino, D. M., and Gou, L. (2010). *ApJ*, 710:1127.
- Carroll, B. W. and Ostlie, D. A. (2007). *An Introduction to Modern Astrophysics (2nd edition)*. Edited by A. R. S. Black.

- Carter, D., Benn, C. R., Rutten, R. G. M., Breare, J. M., Rudd, P. J., King, D. L., Clegg, R. E. S., Dhillon, V. S., Arribas, S., Rasilla, J.-L., Jenkins, C. R., and Charles, P. A. (1993). *ISIS Users' Manual*.
- Casares, J. and Charles, P. A. (1994). *MNRAS*, 271:L5.
- Casares, J., Charles, P. A., and Kuulkers, E. (1998). *ApJ*, 493:L39.
- Castro-Tirado, A. J., Brandt, S., Lund, N., Lapshov, I., Sunyaev, R. A., Shlyapnikov, A. A., Guziy, S., and Pavlenko, E. P. (1994). *ApJS*, 92:469.
- Castro-Tirado, A. J., Geballe, T. R., and Lund, N. (1996). *ApJ*, 461:L99–L101.
- Chamel, N., Haensel, P., Zdunik, L. L., and Fantina, A. F. (2013). *Int. J. Mod. Phys, E22*.
- Chapuis, C. and Corbel, S. (2004). *A&A*, 414:659.
- Chaty, S. (2011). *In: ASP Conference Series. Edited by L. Schmidtbreick and M. Schreiber and C. Tappert*, volume 447.
- Church, M. J. and M.Balucińska-Church (2004). *MNRAS*, 348:955–963.
- Collado, A., Gamen, R., Barbá, R. H., and Morrell, N. (2015). *A&A*, 581:A49.
- Cowley, A. P. (1992). *Annual Review of Astronomy and Astrophysics*, 20:287.
- d’Amico, N., Lyne, A. G., Manchester, R. N., Possenti, A., and Camilo, F. (2001). *ApJ*, 548:L171.
- de Martino, D., Casares, J., Mason, E., Buckley, D. A. H., Kotze, M. M., Bonnet-Bidaud, J. M., Mouchet, M., Coppejans, R., and Gulbis, A. A. S. (2014). *MNRAS*, 440:3004–3014.

- de Martino, D., Falanga, M., Bonnet-Bidaud, J.-M., Belloni, T., Mouchet, M., Masetti, N., Andruchow, I., Cellone, S. A., Mukat, K., and Matt, G. (2010). *A&A*, 515(A25).
- Deller, A. T., Archibald, A. M., Briskin, W. F., Chatterjee, S., Janssen, G. H., Kaspi, V. M., Lorimer, D., Lyne, A. G., McLaughlin, M. A., Ransom, S., Stairs, I. H., and Stappers, B. (2012). *ApJ*, 756:L25.
- Deller, A. T., Moldon, J., Miller-Jones, J. C. A., Patruno, A., Hessels, J. W. T., Archibald, A. M., Paragi, Z., Heald, G., and Vilchez, N. (2015). *ApJ*, 809:13.
- Dunford, A., Watson, C. A., and Smith, R. C. (2012). *MNRAS*, 422:3444.
- Eggleton, P. P. (1983). *ApJ*, 268:368.
- Elvis, M., Page, C. G., Pounds, K. A., Ricketts, M. J., and Turner, M. J. L. (1975). *Nature*, 257:656–657.
- Fabrika, S. (2006). *Astrophysics and Space Physics Reviews*, 12:1.
- Farr, W. M., Sravan, N., Cantrell, A., Kreidberg, L., Bailyn, C. D., Mandel, I., and Kalogera, V. (2011). *ApJ*, 741:103–121.
- Fender, R. P., Garrington, S. T., McKay, D. J., Muxlow, T. W. B., Pooley, G. G., Spencer, R. E., Stirling, A. M., and Waltman, E. B. (1999). *MNRAS*, 304:865–876.
- Flannery, B. P. (1975). *MNRAS*, 170(325-331).
- Frank, J., King, A. R., and Raine, D. J. (1985). *Accretion Power in Astrophysics*.
- Froning, C. S., Cantrell, A. G., Maccarone, T. J., France, K., Khargharia, J., Winter, L. M., Robinson, E. L., Hynes, R. I., Broderick, J. W., Markoff, S., Torres, M.

- A. P., Garcia, M., Bailyn, C. D., Prochaska, J. X., Werk, J., Thom, C., Béland, S., Danforth, C. W., Keeney, B., and Green, J. C. (2011). *ApJ*, 743:26–39.
- Froning, C. S. and Robinson, E. L. (2001). *ApJ*, 121:2212–2218.
- Froning, C. S., Robinson, E. L., and Bitman, M. A. (2007). *ApJ*, 663:1215–1224.
- Fryer, C. L. and Kalogera, V. (2001). *ApJ*, 554:548–560.
- Giacconi, R., Gursky, H., and Paolini, F. R. (1962). *PhRvL*, 9:439.
- Gonzalez-Hernandez, J. I. and Casares, J. (2010). *A&A*, 516:A58.
- Greiner, J., Cuby, J., M. McCaughrean, Castro-Tirado, A., and Mennickent, R. (2001a). *A&A*, 373:L37.
- Greiner, J., Cuby, J., and M. McCaughrean (2001b). *Nature*, 414:522.
- Grimm, H.-J., Gilfanov, M., and Sunyaev, R. (2002). *A&A*, 391:923–944.
- Halpern, J. P., Gaidos, E., Sheffield, A., Price-Whelan, A. M., and Bogdanov, S. (2013). *The Astronomer’s Telegram*.
- Hessells, J. W. T., Roberts, M. S. E., McLaughlin, M. A., Ray, P. S., Bangale, P., Ransom, S. M., Kerr, M., Camilo, F., and DeCesar, M. E. (2011). Radio pulsars: An astrophysical key to unlock the secrets of the universe. *AIP Conference Proceedings*, 1357:40–43.
- Hill, A. B., Szostek, A., Corbel, S., Camilo, F., Corbet, R. H. D., Dubois, R., Dubus, G., Edwards, P. G., Ferrara, E. C., Kerr, M., Koerding, E., Koziel, D., and Stawarz, L. (2011). *MNRAS*, 415:235.
- Hillwig, T. C. and Gies, D. R. (2008). *ApJ*, 676:L37–L30.

- Homer, L., Szkody, P., Chen, B., Henden, A., Schmidt, G., Anderson, S. F., Silvestri, N. M., and Brinkmann, J. (2006). *AJ*, 131:562.
- Horack, J. M. (1991). *Development of the Burst and Transient Source Experiment (BATSE)*, vol. 1268, NASA Ref. Publ.
- Hurley, D. J., Callanan, P. J., and Reynolds, M. T. (2013). *MNRAS*, 430:1832–1838.
- Hynes, R. I., Zurita, C., Haswell, C. A., Casares, J., Charles, P. A., Pavlenko, P. V., Shugarov, S. Y., and Lott, D. A. (2002). *MNRAS*, 330:1009–1021.
- Khargharia, J., Froning, C. S., and Robinson, E. L. (2010). *ApJ*, 716:1105–1117.
- Kippenhahn, R. and Weigert, A. (1994). *Stellar Structure and Evolution*. Edited by R. Kippenhahn and A. Weigert.
- Kovaleva, D., Malkov, O., Yungelson, L., and Chulkov, D. (2017). *arxiv*, arXiv:17012.
- Lattimer, J. M. and Prakash, M. (2004). *Science*, 304:536–542.
- Lattimer, J. M. and Prakash, M. (2015). *arxiv*, arXiv:1512.07820.
- Lebzelter, T., Seifahrt, A., S., R., Bagnulo, S., Hartman, H., Hussain, G., Kaeufl, H.-U., Nieva, M.-F., Przybilla, N., Seemann, U., Smette, A., Uttenthaler, S., Wahlgren, G., and Wolff, B. (2012). *A&A*, 539(A109).
- Lewin, W. H. G. (1997). *X-ray Binaries (Cambridge Astrophysics Series)*. Edited by W. H. G. Lewin and J. van Paradijs and E. P. J. van den Heuvel.
- Liu, Q. Z., van Paradijs, J., and van der Heuvel, E. P. L. (2007). *A&A*, 469:807–810.
- Lubow, S. H. and Shu, F. H. (1975). *ApJ*, 198:383–405.

- Margon, B. (1984). *Ann. Rev. Astron. Astrophys.*, 22:507–536.
- Marsh, T. R., Robinson, E. L., and Wood, J. H. (1994). *MNRAS*, 266:137–154.
- Marshall, J. L., Burles, S., Thompson, I. B., Shectman, S. A., Bigelow, B. C., Burley, G., Birk, C., Estrada, J., Jones, P., Smith, M., Kowal, V., Castillo, J., Storts, R., and Ortiz, G. (2008). *SPIE*, 7014:169.
- Martí, J., Mirabel, I. F., Chaty, S., and Rodríguez, L. F. (2000). *A&A*, 356:943–948.
- Masetti, N., l. Morelli, Palazzi, E., Galaz, G., Bassani, L., Bazzano, A., Bird, A. J., Dean, A. J., Israel, G. L., Landt, R., Malizia, A., Minitti, D., Schiavone, F., Stephen, J. B., Ubertini, P., and Walter, R. (2006). *A&A*, 459:21.
- Massey, P. (1997). *A User’s Guide to CCD Reductions with IRAF*.
- Massey, P., Valdes, F., and Barnes, J. (1992). *A User’s Guide to Reducing Slit Spectra with IRAF*.
- Matsuoka, M., Kawasaki, K., Ueno, S., H.Tomida, Kohama, M., Suzuki, M., Adachi, Y., Ishikawa, M., Mihara, T., Sugizaki, M., Isobe, N., Nakagawa, Y., Tsunemi, H., Miyata, E., Kawai, N., Kataoka, J., Morii, M., Yoshida, A., Negoro, H., Nakajima, M., Ueda, Y., Chujo, H., Yamaoka, K., Yamazaki, O., Nakahira, S., You, T., Ishiwata, R., Miyoshi, S., Egughi, S., Hiroi, K., Katayama, H., and Ebisawa, K. (2008). *PASJ*, 61:999.
- McClintock, J. E. and Remillard, R. A. (1986). *ApJ*, 308:110–122.
- McGregor, P., Hart, J., Conroy, P., Pfitzner, L., Bloxham, G., Jones, D., Downing, M., Dawson, M., Young, P., Jarnyk, M., and van Harmelen, J. (2002). *SPIE*, 4841(178).

McKee, C. F. and Ostriker, E. C. (2007). *ARA&A*, 45:565–687.

Mirabel, I. F., Bandyopadhyay, R., Charles, P. A., Shahbaz, T., and Rodríguez, L. F. (1997). *ApJ*, 477:L45–L48.

Mirabel, I. F. and Rodríguez, L. F. (1994). *Nature*, 371:46.

Murphy, M. T., Tzanavaris, P., Webb, J. K., and Lovis, C. (2007). *MNRAS*, 378:221.

Narayan, R. and McClintock, J. E. (2012). *MNRAS*, 419:L69–L73.

Neil, E. T., Bailyn, C. D., , and Cobb, B. E. (2007). *ApJ*, 657:409–414.

Neilsen, J., Steeghs, D., and Vrtillek, S. D. (2008). *MNRAS*, 384:849–862.

Oke, J. B. (1977). *ApJ*, 217:181–185.

Orosz, J. A. and H.Hauschildt, P. (2000). *A&A*, 364:265.

Özel, F., Psaltis, D., Narayan, R., and McClintock, J. E. (2010). *ApJ*, 725:1918–1927.

Papitto, A., Ferrigno, C., Bozzo, E., Rea, N., Pavan, L., Burderi, L., Burgay, M., Campana, S., Salvo, T. D., Falanga, M., Filipović, M. D., Freire, P. C. C., Hessels, J. W. T., Possenti, A., Ransom, S. M., Riggio, A., Romano, P., Sarkissian, J. M., Stairs, I. H., Stella, L., Torres, D. F., Wieringa, M. H., and Wong, G. F. (2013). *Nature*, 501:517–520.

Patruno, A., Archibald, A. M., Hessels, J. W. T., Stappers, S. B. B. W., Bassa, C. G., Janssen, G. H., Kaspi, V. M., Tendulkar, S., and Lyne, A. G. (2014). *ApJL*, 781:L3.

Patruno, A. and Watts, A. L. (2013). *arxiv*, arXiv:1206.2727.

- Plotkin, R. M., Miller-Jones, J. C. A., Gallo, E., Jonker, P. G., Homan, J., Tomsick, J. A., 7, P. K., Russell, D. M., Heinz, S., Hodges-Kluck, E. J., Markoff, S., Sivakoff, G. R., Altamirano, D., and Neilsen, J. (2016). *arxiv*, arXiv:1611.02810.
- Podsiadlowski, P., Rappaport, S., and Han, Z. (2003). *MNRAS*, 341:385–404.
- Podsiadlowski, P., Rappaport, S., and Pfahl, E. D. (2002). *ApJ*, 565:1107–1133.
- Pringle, J. E. and Wade, R. A. (1985). *Interacting Binary Stars*.
- Radhakrishnan, V. and Srinivasan, G. (1984). *Paper presented in the Second Asia-Pacific Regional Meeting in Astronomy, Bundung, poceedings. Edited by B. Hidayat and M. W. Feast. Tira Pustaka, Jakarta (1984)*.
- Rau, A., Greiner, J., and McCollough, M. L. (2003). *ApJ*, 590:L37–L40.
- Reid, M. J., McClintock, J. E., Steiner, J. F., Steeghs, D., Remillard, R. A., Dhawan, V., and Narayan, R. (2014). *Ap.J*, 796:2–10.
- Ribeiro, T., Baptista, R., Harlaftis, E. T., Dhillon, V. S., and Rutten, R. G. M. (2007). *A&A*, 474:213–220.
- Ritter, H. and Kolb, U. (2003). *A&A*, 404:301–303.
- Russell, D. M., Fender, R. P., and Jonker, P. G. (2007). *MNRAS*, 379:1108–1116.
- Salaris, M. and Cassisi, S. (2005). *Evolution of Stars and Stellar Populations*.
- Sanwal, D., Robinson, E. L., Zhang, E., Colomé, C., Harvey, P. M., Ramseyer, T. F., Hellier, C., and Wood, J. H. (1996). *ApJ*, 460:437–442.
- Sazonov, S. Y. and Revnivtsev, M. G. (2013). *A&A*, 423:469.
- Shahbaz, T., Bandyopadhyay, R., Charles, P. A., and Naylor, T. (1996). *MNRAS*, 282:977–981.

- Shahbaz, T., Bandyopadhyay, R. M., and Charles, P. A. (1999). *A&A*, 346:82–86.
- Shahbaz, T., Dhillon, V. S., Marsh, T. R., Casares, J., Zurita, C., and Charles, P. A. (2010). *MNRAS*, 403:2167–2175.
- Shahbaz, T., Linares, M., Nevado, S. P., Rodríguez-Gil, P., Casares, J., Dhillon, V. S., Marsh, T. R., Littlefair, S., Leckngam, A., and Poshyachinda, S. (2014). *MNRAS*, 453:3461–3473.
- Shahbaz, T., Ringwald, F. A., Bunn, J. C., Naylor, T., Charles, P. A., and Casares, J. (1994). *MNRAS*, 271:L10–L14.
- Shakura, N. I. and Sunyaev, R. A. (1973). *A&A*, 24:337–355.
- Shectman, S. A. and Johns, M. (2003). *SPIE*, 4837:910.
- Stappers, B. W., Archibald, A. M., Bassa, C. G., Hessels, J. W. T., Janssen, G. H., Kaspi, V. M., Lyne, A. G., Patruno, A., and Hill, A. B. (2013). The Astronomer’s Telegram.
- Steehhs, D., McClintock, J. E., Parsons, S. G., Reid, M. J., Littlefair, S., and Dhillon, V. S. (2013). *ApJ*, 786(185).
- Sterken, C. (2005). *The O-C Diagram: Basic Procedures. In: Proceedings of ASP Conference Series. Edited by C. Sterken*, volume 335.
- Tanaka, Y. and Shibazaki, N. (1996). *ARA&A*, 34:604–644.
- Tauris, T. M. and van den Heuvel, E. P. J. (2003). *In: Compact Stellar X-ray Sources. Edited by W. Lewin and M. van der Klis. Cambridge Astrophysics Series No. 39, Cambridge University Press.*
- Tegmark, M. (2004). *ApJ*, 606:702–740.

- Thorstensen, J. R. and Armstrong, E. (2005). *AJ*, 130:759.
- Tobin, J. J., Kratter, K. M., Persson, M. V., Looney, L. W., Dunham, M. M., Segura-Cox, D., Li, Z.-Y., Chandler, C. J., Sadavoy, S. I., Harris, R. J., Melis, C., and Pérez, L. M. (2016). *Nature*, 583:483–486.
- Tonry, J. and Davis, M. (1979). *AJ*, 84:1511.
- Truss, M. R. and Wynn, G. A. (2004). *MNRAS*, 353:1048–1054.
- Warner, B. (1995). *Cataclysmic Variable Stars*.
- White, N. E., Kaluzienski, L. J., and Swank, J. L. (1984). *High Energy Transients in Astrophysics. Edited by S. Woosley*.
- Wijnands, R. and van der Klis, M. (1998). *Nature*, 394(344).
- Williams, J. P. and Cieza, L. A. (2011). *ARA&A*, 49:67–117.
- Woudt, P. A., Warner, B., and Pretorius, M. L. (2004). *MNRAS*, 351(1015).
- Zacharias, N., Monet, D. G., Levine, S. E., Urban, S. E., Gaume, R., and Wycoff, G. L. (2004). The Naval Observatory Merged Astrometric Dataset (NOMAD). In *American Astronomical Society Meeting 205; Bulletin of the American Astronomical Society, Vol. 36, p.1418*.